Universität Augsburg
Mathematisch-Naturwissenschaftliche
Fakultät

On the role of soft interfaces for the understanding of blood clotting

Dissertation zur Erlangung des Doktorgrades der mathematisch-naturwissenschaftlichen Fakultät der Universität Augsburg

vorgelegt von
Christoph Westerhausen

Augsburg, 29.03.2012

Universität Augsburg
Lehrstuhl für
Experimentalphysik I

1. Gutachter: Prof. Dr. Matthias Schneider
2. Gutachter: Prof. Dr. Armin Reller
Tag der mündlichen Prüfung: 05. Juni 2012

"Rule #32: Enjoy the little things!"

Tallahassee in the movie "Zombieland", 2009

Contents

Summary - On the role of soft interfaces for the understanding of blood clotting

"How can the events in space and time which take place within the spatial boundary of a living organism be accounted for by physics and chemistry?" was the question brought up by Erwin Schrödinger 1944 in his book "What is Life?" [1]. A question that claims an interdisciplinary ansatz and cannot be solved without research between biology, chemistry, medical science and physics on an equal level. Motivated by this question, the present thesis treats biophysical aspects of primary hemostasis, mainly from a thermodynamic point of view. Especially the fundamental role of transitions of the protein von-Willebrand-Factor (VWF) and lipid membranes for their function in the context of blood clotting is studied. The protein VWF that plays a crucial role in hemostasis exhibits a conformation change under shear flow from a coiled to a stretched string like shape [2]. During this process binding sites for blood platelets are exposed, leading to the formation of a plug of VWF and platelets, that closes lesions of the vascular system. In the clinical picture of Von-Willebrand-Disease type 2A and 2B the patients tend to increased bleeding. The knowledge about the importance of the conformation for the proteins function and the shear force dependent conformation change lead to the question about the correlation of dysfunction and conformation change.

Can these bleeding dysfunctions of mutated VWF be explained with altered threshold forces for the conformation change from coiled to elongated state?

Surprisingly, the tendency for platelet aggregation of the two mutations is exact opposite: while 2A shows a decrease of function, VWF 2B exhibits a gain of function. In the frame of this thesis we adress the question, whether a mechanical explanation, that correlates a higher/lower force threshold for the conformation change of the according mutation of VWF, applies or not. To answer this question the mechanical properties of the proteins were determined with atomic force spectroscopy. By fitting the necessary stretching force of the polymers with the worm-like-chain model, quantitative statistics on the elasticity associated persistence length are compared for wild type and mutated VWF. The interpretation of the experiments is supported by systematic simulation of force distance curves of polymers. Indeed differences can be seen: while VWF 2A needs slightly lower stretching forces than WT, VWF 2B polymers need higher stretching forces. Hence, this result fits not to the simple mechanical picture that the aggregation tendency is a consequence of differences in the necessary unfolding forces according to the ability of platelet aggregation. Instead we propose the following hypothesis may be the case: clinically the reason for the increased bleeding is the lack of high weight multimers in both mutations, the reason for this lack, however, is different. VWF 2A is stretched at lower forces and thus, the probability for cleavage by the VWF cleaving protease ADAMTS13 is increased. As a consequence of the increased cleaving probability the higher multimers are absent in these patients. On the other side VWF 2B needs higher stretching forces than WT.

Although the high weight multimers do exist in patients with the mutation 2B, due to an increased binding affinity to platelets the high weight multimers are not available for primary hemostasis at sites of injury, leading to the same clinical effect.

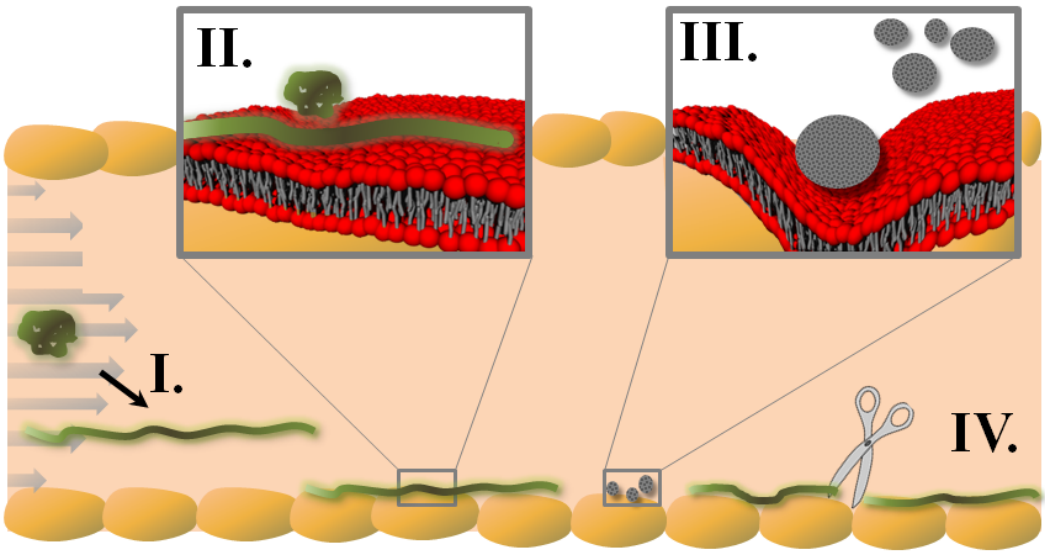

Figure 0.1.: I. Differences in shear induced unfolding of VWF in hemophilia. **II.** Conformation dependent interaction of VWF with lipid membranes. **III.** Impact of protein mimetics (e.g. nanoparticles) on the state of the membrane. **IV.** Cleavage of VWF by the enzyme ADAMTS13 at the cell membrane.

What is the role of the VWF conformation for its interaction with phospholipid membranes?

After activation (stretching) VWF is prepared to bind to the membrane of the endothelia cells. As this adhesion is a crucial step in hemostasis, the interaction of wildtype VWF and mutations of type 2A and 2B with lipid interfaces were studied in Langmuir monolayer experiments. The, at first glance, strongly altered compressibility of the system, independent of the type of mutation, was relativized by comparison with calculations of a two component system (VWF and lipids). Detailed studies show apart from an ideal superposition some less drastic effects of globular VWF with lipid monolayers. Comparing these results with the interaction of fully elongated VWF with lipid membranes indicates that the shear force induced conformation change of VWF also switches the interaction with phospholipid membranes without special binding sites on the membrane side. In the frame of these studies thermodynamic considerations show, how information about the binding affinity between VWF and lipid monolayers in the two liquid phases can be extracted.

How is the phase state affected by simple protein mimetics?
After the interaction of membranes and VWF has been studied dependent on the state of the protein, the question appears about the interaction dependent on the state of the membrane. The manipulation of the state of biological membranes by the adhesion of proteins like VWF, is studied with well characterized nanoparticles as simple protein mimetics. Besides this reason the impact of NPs on cell membranes of course is from high sociocultural relevance due to the increasing addition of NPs for example in food and cosmetica. To overcome such barriers in nature, there are different uptake pathways that are partly associated with the presence of particular proteins [3]. To illuminate such processes, from a physicists point of view, the impact of NPs on the thermodynamical properties of phospholipid bilayers with a focus on the main phase transition was studied. The consequences are rather physical explanations of the observes effects, e.g. induced curvature, than biochemical ones. In calorimetric measurements size dependent effects of silica NPs on various solid-supported phosphatidylcholine membranes were found. A detailed model combing thermodynamical and mechanical aspects explains the effects. Besides the mainly curvature induced effect, a chemical effect, namely a NP concentration dependent melting point depression was observed and explained. Furthermore in fluorescence microscopic studies of the temperature induced phase transition of giant unilamellar vesicles (GUVs) morphological changes occur. These experiments open ways to think about endocytosis supported by proteins rather from a physicists than from a biochemists point of view.
What is the role of the phase state of the membrane for the activity of the VWF cleaving protease ADAMTS13?
After activation VWF is not only more likely to bind but also more likely to interact with the cleaving protease ADAMTS13. Knowing that the conformation of VWF switches interaction strength with lipid membranes, and that protein mimetics can change the state of the lipid membrane, the question comes up, whether the state of the membrane also affects this mechanism in the blood clotting process. The optimal function of VWF in vivo depends on the cleavage of the unrolled polymers in shorter fractions by the enzyme ADAMTS13. In physiology the unrolled VWF is mainly adhered to the endothelial cells and thus, the reaction takes place in the vicinity of biological membranes. Hence, a possible mechanism affected by the membrane state is the enzyme activity. To testify the impact of the membrane state, ADAMTS13 was bound to phosphatidylcholine vesicles, the catalytic rate was measured temperature dependent and compared with the activity of unbound enzyme in lipid-free samples. In contrast to the activity of free ADAMTS13, the activity of membrane bound enzyme shows more than a simple linear temperature dependence. Astonishingly the phase transition temperature divides two temperature ranges where the temperature dependence of the rate of this, naturally not membrane associated enzyme, changes by one order of magnitude. Besides the common method for the determination of the enzyme

activity from the maximal rate of kinetic curves an alternative method is shown. Deviations between theory and measurement, concerning the rate especially at the phase transition temperature are discussed in the controversy of membrane fluidity or phase state as crucial parameter for catalysis.

In summary this work shows how the consequences of statistical physics, thermodynamics, in an interdisciplinary context can contribute to the answer of Schrödingers‘ question.

Preamble

Before we get to the core of the matter, the structure of this thesis is pointed out. As indicated in the summary, the study of biophysical aspects of processes involved in primary hemostasis is divided in the following four questions:

- Can bleeding dysfunctions of mutated VWF be explained with altered threshold forces for the coiled to elongated conformation change?
- What is the role of the VWF conformation for its interaction with phospholid membranes?
- How is the phase state affected by simple protein mimetics?
- What is the role of the phase state of the membrane for the activity of the VWF cleaving protease ADAMTS13?

To be prepared for the topic, in the next part very briefly basic information on the main matter (VWF, lipids, NP and ADAMTS13) are given. Subsequently the four main questions are answered. For this, the structure of each chapter, according to the four questions, is geared on a typical publication in the particular field: a introduction presents the state of the art and leads to the question. Before the results are presented and discussed in a critical manner, the used materials and methods of the particular experiments are shown. Finally a conclusion and, where appropriate, an outlook on ongoing research is pointed out.
In addition for each results chapter further information like protocols, calculations, additional studies on side effects are added in a separate appendix. Thus, it should be also possible to understand single result chapters in combination with the associated basic and appendix chapters.

Part I.

Basics

1. The protein von Willebrand factor as main actor in hemostasis

Beyond all question the accurate function of the blood clotting process is indispensable to life. In physiology the protection against bleeding is secured by sealing of the defect, initially done by the adhesion of platelets and the protein von Willebrand factor (VWF). This section describes in brief the leading role of VWF in hemostasis, mainly based on the publications [4, 5] and references therein. The multimeric protein VWF consists of identical subunits,

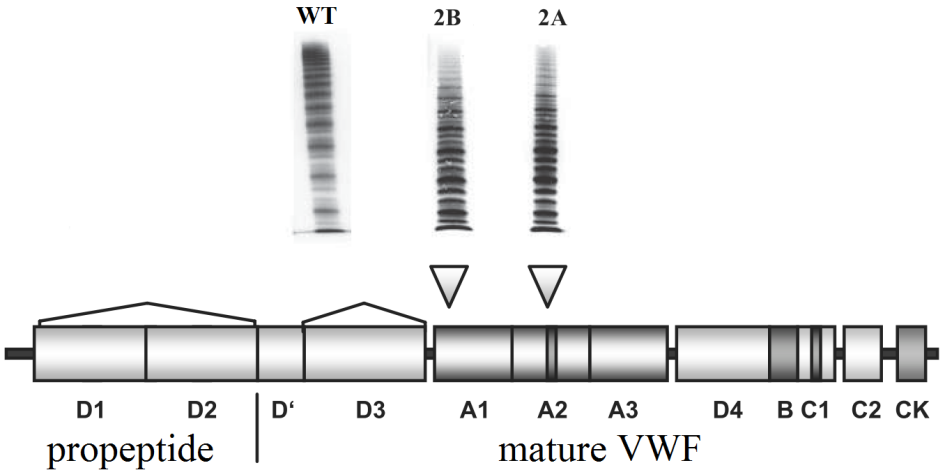

Figure 1.1.: Domain structure of VWF (adapted from [6]). Two prominent mutations 2A and 2B correlated with bleeding disorder are located in the A2 respectively A1 domain. The multimeric pattern of both mutations are similar and show a decreased fraction of high multimers compared to wild type VWF (WT).

that are linked with disulfide bonds into dimers of 512kD. The subunit of VWF consists of several functional domains as fig. 1.1 illustrates. The A1 domain for example can bind VWF to platelets via their receptor GP1$\beta\alpha$. Furthermore these domains bury hydrophobic parts in the inside of the coiled conformation. Another example for the domain specific functions is the regulation of VWF

multimerisation. The cleavage of VWF by the enzyme ADAMTS13 (see also chapter 8) happens enhanced if the A2 domain is unfolded [7]. The dimers again are linked with disulfide bonds into multimers of 20 and more dimers, resulting in a length of 2μm and longer. For understanding of the role of VWF in primary hemostasis one has to know, that the function of VWF in hemostasis is strongly dependent on the conformation of the protein. In the blood stream VWF is existent in a globular conformation, whereas at high shear forces the protein is unrolled in a stretched conformation showing the full length of the protein. This reversible conformation change was shown to happen as a certain shear rate threshold is exceeded [2].

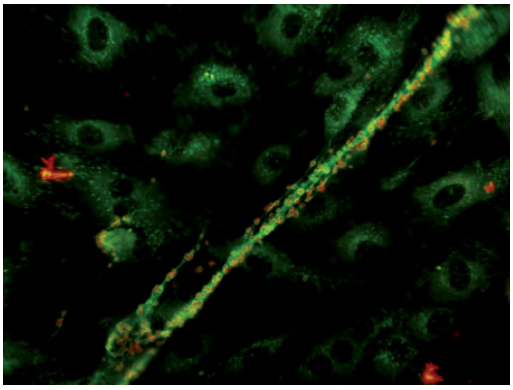

Figure 1.2.: A VWF fiber ($\approx$400μm long) is stretched under shear flow and adhered to endothelial cells (green cells in background). The red labeled thrombozytes bind to VWF (taken from [4]).

When a defect at the vessel wall is detected, the platelets adhere to this site and aggregate with help of VWF. But the platelets solely bind to VWF in its unrolled conformation via the glycoprotein I$\beta\alpha$ receptors at the platelet surface. As a consequence further receptors are expressed, leading to a acceleration of the blood coagulation [8]. At these bound platelets again unrolled VWF adheres and builds up fibres and networks of huge size, that stabilize the inital aggregation of platelets. These processes are called primary hemostasis. In fig. 1.2 an in-vitro experiment shows a VWF fiber stretched under shear flow and adhered to endothelial cells. To this VWF fiber thrombozytes bind.
Without VWF the crucial step of platelet aggregation at the side of the injury would not or only weakly happen. In contrast, secondary hemostasis denotes the events of stimulated clotting, thrombin and fibrin formation, that finally stops blood leakage. Besides the crucial role in primary hemostasis, also during the second part of hemostasis VWF protects coagulation factor VIII and stabilizes the protein structures in this wound healing process. Quantitative deficiency of VWF also leads to deficiency of factor VIII. This disease named, Von-Willebrand-Jürgens-Syndrome belongs to the most frequent hereditary disease [6].
Normally blood clotting happens outside of the vascular system at sides of vulneration. But if the aggregation of platelets occurs to some reason inside the vascular system without a vulneration this is called thrombosis. A consequence then is the partly or complete stasis, i.e. the bloodstream is stopped in a certain part of the body. If the thrombi block the vascular system of important organs, like the lung, this dramatic and often lethal incidence is called

embolism [9]. The opposite case, that hemostasis does not happen sufficiently, when a vulneration appears is called hemophilia. It can be caused by a lack of coagulation factors, like factor VIII, or quantitative and qualitative malfunctions of VWF. As well hypo function as hyper function of VWF concerning platelet aggregation is correlated with mutations in the primary molecular structure of VWF. Chapter 5 treats the question how these mutations influence the crucial conformation change, especially if the clinical malfunctions are correlated with the mechanical properties of the mutated proteins.

2. Phospholpids in biologicals systems and general surface physics

Phospholipid as the main part of cell membranes

The basic building block of living individuums is a single cell. All cells as well as all compartments inside the cells are surrounded by a lipid bilayer containing proteins and sugar molecules. These natural barriers are linked to the actin filament and control the influx and efflux of the cell. On the way explaining processes in living systems, a very reduced and simple model for those membranes are phospholipid bilayers [10], consisting of one or more components.

Chemical structure

The characteristic behavior of the lipids results from their amphiphiphilic properties. While the headgroup is hydrophilic, the carbon chains are hydrophobic, mainly due to entropy. This is the reason for the self organisation of lipids in water or on a water surface. In water the lipids try to avoid contact of the tail regions with water leading to micelles or vesicles or more dense networklike bilayer structures. The different organization forms of lipids in water, relevant for this thesis, are introduced in the following part.

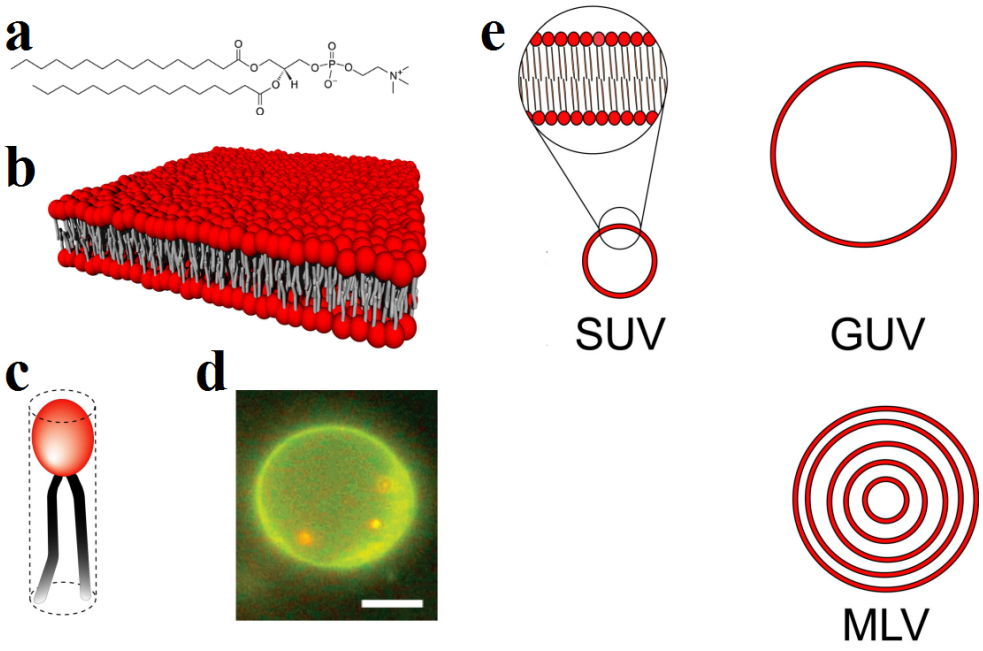

Figure 2.1.: **(a)** Chemical structure of DPPC. **(b)** The amphiphilic molecules organize in lipid bilayer structures. **(c)** The polar head group is simplified as one part of the lipid and the apolar carbon chains are the hydrophobic part of the molecule. **(d)** Microscopic picture of a GUV (scale bar 5 μm) **(e)** Different vesicular structures: small unilamellar vesicles SUV, giant unilamellar vesicles GUV, multi lamellar vesicles MLV (adapted from [11].

Forms of organisation of lipids

Besides the above mentioned micelles or networklike structures divers vesicular structures are possible and used in science depending on the intended purpose. In the framework of this thesis the following organisation forms were used.

Monolayers

A very simple but highly reproducible way to produce easy controlable lipid interfaces that posses similar properties like biological membranes are Langmuir monolayers. If the, in chloroform solved, molecules are given to a through with water, the amphiphilic molecules accumulate at the air-water interface. The headgroups are in contact with the water, whereas the carbon chains point towards the air.

Vesicles

Above a certain concentration in the pico molar range lipids form energetical favorable vesicular structures. The following three forms of lipid vesicles were used within the experiments presented in this thesis.

Multi lamellar vesicles - MLV

Multilamellar vesicles are the variant of vesicles that is produced with the least necessary intrusion from outside. A typical procedure for phosphatidylcholine MLVs is the following. The chloroform-lipid-solutions are dried under nitrogen atmosphere for some minutes and subsequently under vacuum for three hours to evaporate the chloroform completely. Afterwards the lipids are re-hydrated with the intended aqueous solution (water, buffer, nanoparticle solutions,...) in a heat bath at temperatures above the main phase transition temperature. Simple shaking of the solution accelerates the formation of this onion like structure of lipid bilayers like illustrated in fig. 2.1e. These MLV, with a tyical size of 0.5 μm to 5 μm are used in the frame of this thesis for studing the impact of membrane state on enzyme activity in chapter 8. The impact of contaminants on the main phase transition of MLV is analysed in chapter 7.

Spherical solid-supported vesicles - SSV

If e.g. silica nanoparticles are added during the preparation process of MLV, after several days spherical solid-supported vesicles are formed, by spreading of the lipid bilayers on the nanoparticles. This process can be accelerated by sonication of the sample during the preparation. More details and citations can be found in section 7.3.2.

Giant uni lamellar vesicles - GUV

Giant unilamellar vesicles with a size of 10 μm - 100 μm can be produced with the well known method of electro swelling. These GUV serve as artifical model for cell membranes that can be observed with a fluorescence microscope like shown in 7.5. Appendix C contains a typical preparation protocol adapted from [12].

Physics of surfaces

This sections deals with a selection of physics of surfaces that are usefull for the understanding of the presented experimental results, especially the lipid monolayer experiments. If not explicitely mentioned the facts are based on [13].

Surface tension

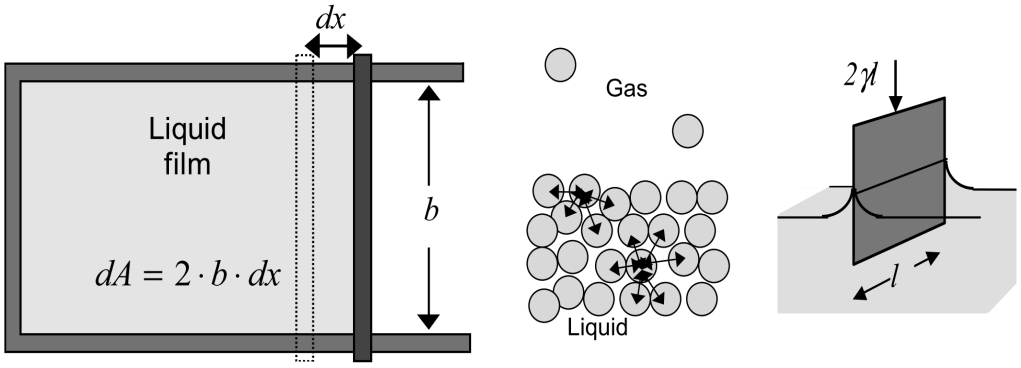

(a) A thin liquid film in a frame.

(b) Molecular explanation of surface tension.

(c) Wilhelmy-plate method.

Figure 2.2.: (a) A thin liquid film in a frame is expanded by a movable barrier. The proportionality factor between needed work and enlargement of area is the definition of surface tension. **(b)** A molecular picture explains surface tension. The molecules in the liquid experience attractive interaction forces from the other molecules. In the bulk the forces vanish while at the surface a finite force remains. **(c)** A thin plate is dipped half into the liquid. The downward pulling force is proportional to the surface tension. (pictures adapted from [13]).

A very important physical term for the physics of surfaces and interfaces it the surface tension. Figure 2.2a shows a thin liquid film in a frame. The area can be expanded by a moveable barrier. A movement of the barrier for a infinitesimal step dx leads to an increase in area of $dA = 2bdx$. The proportionality factor between enlargement of area dA and the needed work dW is called the surface tension γ.

$$dW = \gamma dA \tag{2.1}$$

Furthermore it holds

$$dW = -Fdx \tag{2.2}$$

what in combination delivers:

$$\gamma = \frac{-F}{dA/dx} \approx \frac{-F}{\frac{\partial A}{\partial x}} \tag{2.3}$$

Equation 2.3 allows to determine the surface tension with different methods. A very convenient and widely used method is the determination of surface tension with a Wilhelmy plate. A rectangular filter paper, connected to a sensitive force sensor, is dipped into a liquid. Assuming ideal wetting (contact angle 0°) the change of the wetted area of the plate dA is the product of the change in height dx and the circumference $2l$.

Interfacial excess

At the interface of a liquid phase to a gas phase (like in lipid monolayer experiments) the surface divides the system into two volumes V_{liquid} and V_{gas}, if infinitesimal thickness of the interface is assumed. Both compartmens have internal energies U_i, entropies S_i and number n_{ij} of particles of all components j. At the interface an interfacial excess of a component j is defined by the number n_j of particles of component j of the system minus the numbers of particles of this component in each phase n_{ij} divided by the area of the interface:

$$\Gamma = \frac{n_j - n_{liquid_j} - n_{gas_j}}{A} = \frac{n_j^\sigma}{A} \tag{2.4}$$

The interfacial excess and the surface tension are connected by the Gibbs adsorption isotherm:

$$0 = S^\sigma dT + \sum_j n_j^\sigma d\mu_j + A d\gamma \tag{2.5}$$

, where μ is the chemical potential. At constant temperature the first term vanishs and hence:

$$d\gamma = -\sum_j \Gamma_j d\mu_j. \tag{2.6}$$

Assuming now a simple two component system (e.g. water and solved protein) equation 2.6 changes to:

$$d\gamma = \Gamma_{solvent} d\mu_{solvent} + \Gamma_{solute} d\mu_{solute}. \tag{2.7}$$

By definition of the exact location of the surface $\Gamma_{solvent}$ can be set to zero and hence $d\gamma = \Gamma_{solute} d\mu_{solute}$. Furthermore the chemical potential of the solute

depends logarithmically on a dimensionless concentration c of the solute:

$$\mu_{solute} = \mu^0_{solute} + RTln\frac{c}{c_0} \tag{2.8}$$

Differentiating of eq.2.8 with respect to c, combined with 2.7 delivers

$$\Gamma_{solute} = -\frac{c}{RT}\frac{\partial\gamma}{\partial c}|_T. \tag{2.9}$$

Thus, for positive values of Γ_{solute}, that means if the substance is enriched at the surface, addition of the substance to the solvent leads to a decrease of surface tension. These substances are called surface active, or surfactant if γ decreases drastically (e.g amphiphiphilic phospholipds). Sodiumchlorid for example leads to a slight increase of surface tension. In most of the presented experiments 100 mM NaCl was used. Using the literature value $1.8\,\frac{mN/m}{mol}$ NaCl an increase of surface tension of 0.18 mN/m compared to pure water is expected [14]. As the salt concentration is the same in all compared experiments, a bigger influence is expected due to the surface activity of the used protein VWF, as polymers and proteins can show surface activity, but with less defined phases compared to lipid molecules [15]. Often difficulties are caused due to irreversibility of the area-pressure-isotherms. Furthermore if concentration dependent experiments are compared one should keep in mind that the addition of the protein will lead to a varying decrease of surface tension and thus a variation of the baseline.

Lateral pressure of surfactant monolayers

If a drop of amphiphilic molecules, solved in chloroform, is spread on a water volume, the molecules build a monomolecular layer on the surface. The difference in surface tension of the solution γ and the pure solvent γ_0 is defined as the lateral pressure $\pi = \gamma_0 - \gamma$. By compressing of the layer π increases like indicated in the shematic area-pressure-isotherm in fig. 2.3. A typical phosphatidylcholine monolayer system usually has four phases: a gaseous phase, a liquid expanded, a liquid condensed and a solid condensed phase [16].
In the gaseous phase the average area per molecule is much larger than the molecule size. In the liquid phase there is a significant lateral interaction between the molecules, what results in tilted carbon chain tails of the molecules under further compression. The first order phase transitions between gaseous phase and liquid expanded phase and between liquid expanded and liquid condensed phase induces plateaus at lipid specific and temperature dependent lateral pressures. Typically in measurements in this thesis the systems are driven from the gaseous phase to the liquid condensed phase.

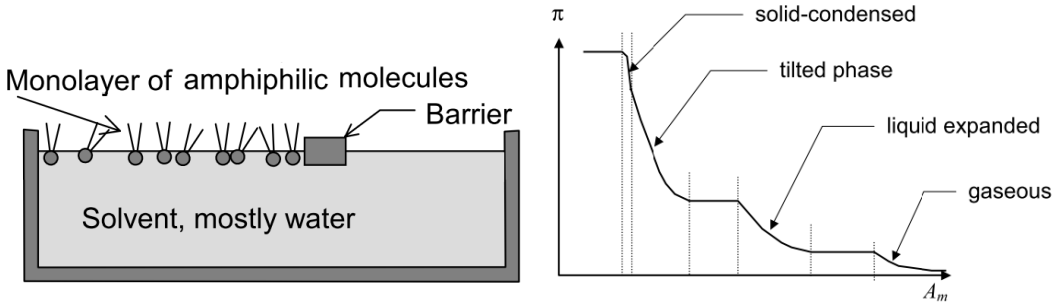

(a) Langmuir monolayer (b) Schematic Area-pressure-isotherm

Figure 2.3.: (a) A monolayer of amphiphilic molecules on the surface of a (mostly) water volume is compressed by a movable barrier. **(b)** A schematic area-pressure-isotherm shows four phases with increasing lateral pressure: gaseous, liquid expanded, tilted or liquid condensed phase, solid condensed phase. Between gaseous and liquid expanded and between liquid expanded and liquid condensed phase is a first order phase transition.

Lipid phase transitions

By controlling the lateral pressure of monolayers in isothermal experiments the phase state can be controlled easily as shown above. Another possibility to change the state of the lipid layer is the change of the temperature at constant lateral pressure. By adjustment of the area per molecule the pressure can be kept constant. In this case the area per lipid molecule as function of the temperature is an accessible indicator for the phase of state of the system. Fig. 2.4a shows how an area isobar for increasing temperature can be understood from a bunch of area isotherms of different temperatures. By increasing the temperature at a fixed lateral pressure from a temperature T for a step ΔT the area is increased according to the area istotherm for the temperature $T+\Delta$T. In this example around 30°C the area increases drasticly, theoretically shows a discontinuity. This discontinuity of the isobar indicates the phase transition from the liquid ordered to the liquid disordered phase for a constant lateral pressure.

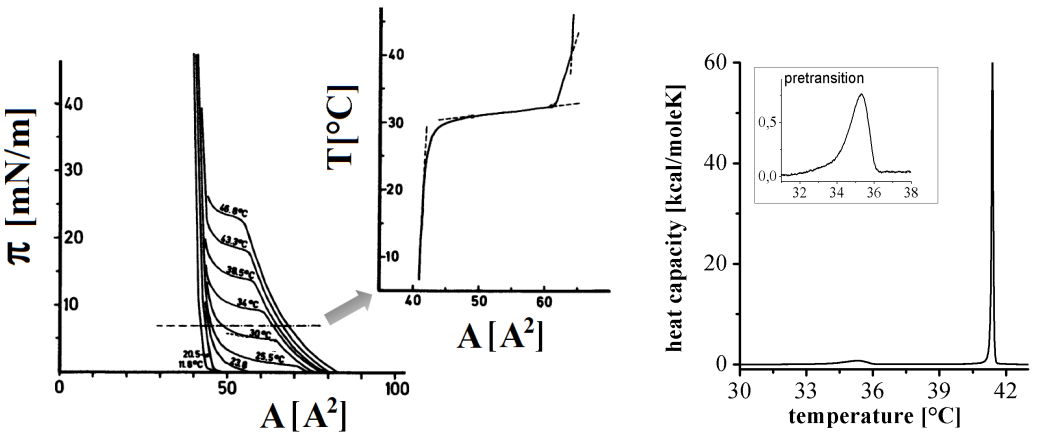

(a) From area isotherms to an area isobar (b) Heat capacity of a DPPC sample

Figure 2.4.: (a) Left: a bunch of area isotherms of DMPA shows the typical increase of phase transition pressure with increasing temperature. Right: Keeping the lateral pressure constant by regulating the area per lipid molecule, one can measure an area isobar. The intersections of the dashed dotted line at 7mN/m with the isotherms in the left graph describe the same (area, temperature)-tuples as the isobar here (adapted from [17]). **(b)** Typical heat capacity profile of a DPPC sample.

Along the same line, a temperature induced phase transition can be observed for lipid bilayer vesicles. Optical observation of the excess area is possible but not very convenient and precise. The transition from the gel-like to the fluid phase of lipid bilayers is a first order phase transition. This means the enthalpy as function of temperature exhibits a discontinuity at the transition temperature and the first derivative, with respect to temperature, a singularity. Thus, this phase transition of vesicles can be analysed very precise and reproducible by measuring the excess heat capacity of the sample with Differential Scanning Calorimetry [18]. A DSC setup measures the heat capacity by heating respectively cooling of a sample and a reference sample with the same volume. With electric heaters the temperature of sample and reference is kept equal during the process. The excess heat capacity of the sample during the phase transition can be directly taken from the difference in required electric power of the heaters (for detailed information about a common DSC device see [19]).
The isobaric heat capacity is defined as follows:

$$C_p = \frac{\partial Q}{\partial T} \mid_p \tag{2.10}$$

From the measured heat capacity the transition enthalpy ΔH can be calcu-

lated, using dH = dQ in the isobaric case:

$$\Delta H = \int_{T_1}^{T_2} \frac{\partial H}{\partial T} dT = \int_{T_1}^{T_2} \frac{\partial Q}{\partial T} dT = \int_{T_1}^{T_2} C_p dT \tag{2.11}$$

Fig. 2.4b shows C_p of a typical DPPC MLV sample. The sharp peak at 41°C indicates the highly cooperative main phase transition. Below this temperature T_M the membrane is in the gel-like phase, a state of high order. Above T_M the membrane is in the fluid phase, with significantly changed intrinsic properties. For further information concerning the phase transition of lipid membranes see the chapters 7, 8 and the references therein.

3. Nanoparticles - Social relevance and characterization of used NP

Silica Nanoparticles in humans environment

Due to the continuing progress in technology, in the last decades nanoparticles (NP) appear more and more in the human environment. The applications of NP are various. As well in food, cosmetics as in drugs divers NP of different materials and shapes are used. As additives to food e.g. titanium dioxide (E551) and silicium dioxide (E171, up to 50 mg/g) is permitted - independent from the particle size [20]. Furthermore in sun screens titanium dioxide NP are already a standard ingredient. Thus, the impact of NP on living organisms is a rapid growing and highly discussed field of research. Recently we were able to show that the biological reaction, measured in form of cytotoxicity, of identical silica NP as used in the context of this thesis, is proportional to the surface area of the NP and not the number or mass of particles [21]. More detailed information and references concerning NP are given in chapter 7. This demonstrates that one of the key advantages, can be also a possible source of risk: due to the size in the nm range the surface to volume ratio is increased enormously compared to micro particles or bulk material in general. Thus, these for the human eye invisible particles can show a high reactivity or overcome the membrane of the cell nucleus.
Besides these social relevance, mono-disperse NP are usefull in science. Because of well defined different sizes they can be used in combination with lipid bilayers as model system for the impact of proteins with cell membranes. Instead of complex biochemical explanation attempts, more general effect likes local curvature changes can be studied with NP. In this thesis there was a special focus on the impact of NP on the phase transition of lipid membranes (chapter 7).

Synthesis and characterization

In the presented studies exclusively silica NP were used that were produced with a modified Stoeber synthesis like reported in [22]. For the fluorescence microscopy experiments silica particles were labeled with the dye Perylene, whereas in the calorimetric studies and the monolayer experiments unlabeled NP were used. The radii of the mono-disperse in water soluted NP spanned a range from 9 nm to 250 nm. Thus systematic studies of membrane effects could be studied.

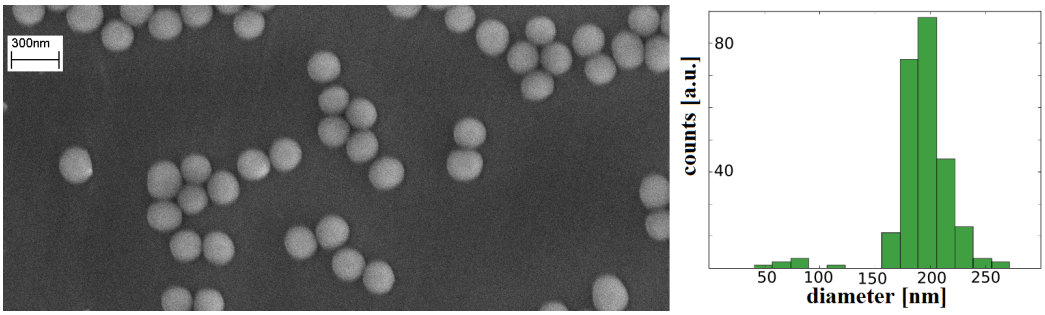

Figure 3.1.: To determine the size of the used silica NP electron microscopy pictures of dried NP solutions were evaluated. Left: Exemplarily a picture of particles with a mean diameter of 200 nm. Right: The size distribution contains the information of several pictures from different areas of the substrate.

Most of the NP were characterized like already described in [12] with scanning electron microscopy, transmission electron microscopy and dynamic light scattering. Beyond the particles mentioned in [12] further batches of NP with differing size were used (see chapter 7). The most important results of the characterization are:

- monodispersity
- chemical stability in water and phosphate buffer (besides a relative high equilibrium concentration of silicic acid in the solvent, shown in chapter 7)
- no tendency for agglomeration due to the negative surface charges (bare particles as well as lipid covered NP)

For further details concerning the synthesis of these particles or quantization of fluorescence etc. the citations [12, 22] or direct contact to Dr. R. Herrmann (University of Augsburg) are recommended.

4. The role of ADAMTS13 and basics in catalysis

Role of ADAMTS13 in hemostasis

As mentioned before, in primary hemostasis ultralarge VWF fibers (ULVWF) are stretched to the enrolled state and bind blood platelets to seal the damage in the blood vessels. The multimerisation of VWF to ULVWF is regulated by the cleavage by a certain protease, that cleaves the large multimers in the A2 domain between the residues Tyr1605 and Met1606, where an acidic group and an alkaline group with similar pK values are built. In the late 1990s a VWF cleaving protease was partially purified [23, 24] and later identified to belong to the ADAMTS family [25, 26]. Since then the name ADAMTS13 is used synonymously for VWF cleaving protease [27]. Furthermore a correlation between the existence of unusual large VWF and thrombotic thrombocytopenic purpura (TTP), the occurence of widespread thrombi in the vasculature, was discovered in 1982 [28]. As VWF is one of the major players in the blood clotting process, this clearly shows the importance of ADAMTS13 as well in healthy organisms as in the case of VWF related diseases. It is known for example, that for certain mutations large VWF fibers are cut faster respectively slower compared to the wildtype.

Enzym kinetics

To ensure comparable values for the cleavage activity of enzymes in general, and here ADAMTS13, the standard reaction scheme is used [29, 30]:

$$\mathrm{E} + \mathrm{S} \underset{k_{-1}}{\overset{k_1}{\rightleftharpoons}} \mathrm{ES} \underset{k_{-2}}{\overset{k_2}{\rightleftharpoons}} \mathrm{E} + \mathrm{P}_1 + \mathrm{P}_2 \tag{4.1}$$

where E means enzyme, S substrate, ES the complex of both and $\mathrm{P}_1, \mathrm{P}_2$ the products. Furthermore the Michaelis constant K_M that is independent from

substrate and enzyme concentration is defined as following:

$$\mathrm{K_M} := \frac{k_{-1} + k_2}{k_1} \tag{4.2}$$

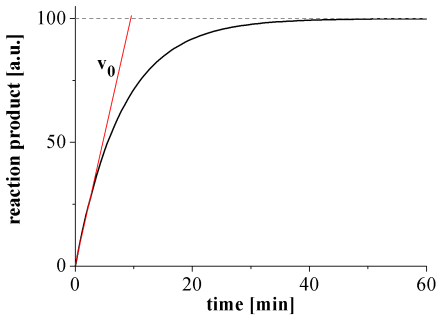

Figure 4.1.: A typical kinetic curve shows a steep increase v_0 of reaction product followed by exponential saturation behavior.

Typical enzyme kinetic curves show a steep nearly linear increase $\mathrm{v_0}$ in the beginning followed by exponential saturation behavior, as illustrated in fig. 4.1. The increase $\mathrm{v_0}$ depends on the enzyme concentration $[E]_T$ and the substrate concentration $[S]$ as follows:

$$\mathrm{v_0} := \mathrm{k_2}\,[\mathrm{E}]_T \frac{[S]}{[S] + K_M} \tag{4.3}$$

If the sample is saturated with substrate the rate v_0 reaches a maximum v_{max} and thus:

$$\mathrm{k_2} = v_{max} / [\mathrm{E}]_T \tag{4.4}$$

Using eq. 4.4 and eq. 4.3 leads to the Michaelis-Menten-Equation that expresses the reaction rate as function of the substrate concentration:

$$v_0 := v_{max} \frac{[S]}{[S] + K_M} \tag{4.5}$$

This leads to a proportionality between catalytic rate and substrate concentration for low substrate concentrations. Whereas for high substrate concentrations the fraction in 4.5 is nearly one and the measured rate is v_{max}. For identical enzyme concentrations and $[S]$ higher than the maximal value of K_M at different temperatures, the rate v_{max} is a capable parameter to compare the enzyme activity while varying other parameters like temperature.

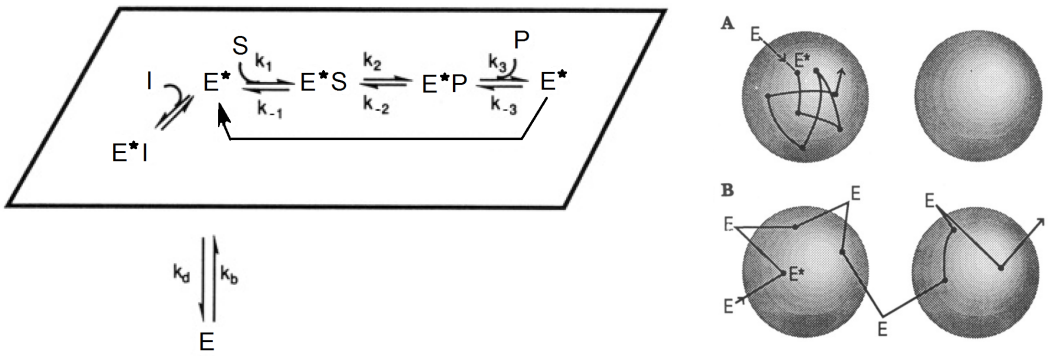

(a) Reaction scheme of interfacial catalysis

(b) Scooting vs. hopping mode

Figure 4.2.: (a) This scheme (taken from [31]) illustrates the key features of interfacial catalysis. The enzyme in the bulk E binds/unbinds with a rate k_b/k_d to the interface (then E*), where it forms a complex with the substrate S. This complex can react to an enzym product complex E*P that dissociates into P and E*. The according rates are k_i/k_{-i}. Optionally E can form a complex with an inhibitor I.**(b)** Illustration (from[31]) of the scooting (A) and the hopping mode (B). In the scooting mode the enzyme binds to the vesicle and moves within the surface, whereas in the hopping mode an enzyme switches between bulk and different vesicles.

Interfacial catalysis

For the special case where the catalytic reaction takes place at a membrane interface the general case described above has to be expanded as illustrated in fig. 4.2a. The enzyme in the bulk E binds/unbinds with a rate k_b/k_d to the interface (then E*), where it forms a complex with the substrate S. This complex can react to an enzyme product complex E*P that dissociates into P and E*. The according rates are k_i/k_{-i}. Optionally E can form a complex with an inhibitor I. Here P stands for the both products P_1, P_2. In the experiments presented in this thesis no inhibitors were used.
Another discussed aspect concerning catalysis at vesicle surfaces is the question of the reaction mode [31]. In Fig. 4.2 the vesicle scooting mode (A) and the vesicle hopping mode (B) are illustrated. If $k_b >> k_d$ the enzyme will not leave the vesicle surface and move within this interface. If desorption is more likely the vesicle hopping mode may be the case. We assume A for our experiments, although the difference is not as crucial as in the case of e.g. phospholipase, where the vesicles are substrate and reaction interface at the same time. Furthermore we show indirectly in section 8.2 that $k_b >> k_d$. Furthermore we assume $k_3 >> k_{-2}$ as shown e.g. for phospholipase A_2 in [32]. Thus, it is plausible to use the simplified equation 4.1 for the moment, keeping in mind, that additional effects due to the restriction of the interface can appear.

Part II.

Results and Discussion

5. Mutations influence mechanical stretching of von Willebrand faktor

5.1. Introduction - A mechanic approach to explain mutation specific dysfunctions in hemostasis

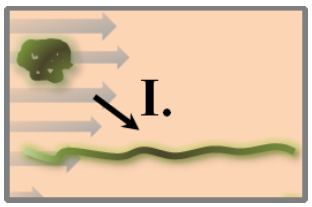

In almost 1% of the population inherited defects of VWF function can be detected. Clinically significant malfunctions affect only $\sim$ 125 per million population [33]. For instance the von-Willebrand-Jürgens-syndrome is one of the most inherited diseases [6]. Therefore, the question about the mechanism behind the causality of certain deviations in the organism compared to healthy persons and the correlated symptoms is the driving force for the presented studies on the mechanical properties of the protein VWF. The crucial role of VWF in primary hemostasis was pointed out already in chapter 1. Its name goes back to E. von Willebrand, who reported already in 1926 about the disease with heterogeneous tendencies in bleeding behavior [34, 35]. This severe bleeding disorder (also: hemophilia), called Von-Willebrand-Desease (VWD) is classified in three types, with quantitative and qualitative changes of VWF: type 1 shows a decreased amount, type 3 absence of VWF; in contrast type 2 classifies qualitative defects of VWF [36].
For a physicist the latter is the most interesting one, as the causality between lack of VWF and absence of its functions seems clear. Within the classification VWD type 2 there a two mutations 2A and 2B, showing a lack in high multimers and are in general not distinguishable in their multimeric pattern [36]. While also the symptoms of the according patients are in both cases similar (e.g. increased bleeding times), the tendency for aggregation of platelets differs drastic between the two mutations. In standardized tests VWF 2A shows a decreased platelet aggregation VWF 2B shows a gain of function, leading

to increased platelet aggregation [37]. In fig. 5.3b the results of a test of agglutination reported in [37] show this in a concrete way. While plasma from 2A patients shows no agglutination even at twice the threshold concentration of healthy patients, the plasma from 2B patients show enhanced agglutination already at a third of this concentration.
At this point a brief summary about the actual state of knowledge concerning these two mutations is given. Demonstrably there is a lack of high molecular weight multimers (HMWM) in the blood of patients with both mutations. These HMWM are necessary for adequate function in primary hemostasis. As the crucial interaction with platelets differs significantly for both mutations there have to be different reasons for the lack of HMWM. Ruggeri et al. in 1980 [38] suggests that in the case of VWF 2A no HMWM are produced, while the binding affinity to platelets is in principle normal. In contrast, in the case of VWF 2B, the ability to synthesize large multimers is unaffected, but due to higher binding affinity of VWF 2B to platelets and tissue the large multimers are removed from the blood circulation. In turn, the lack of the HMWM leads to hemostatic defects.
Combined with the knowledge about the shear force induced unfolding of VWF [2] this leads to the question, whether the reason for the differing agglutination of the two mutations is simply connected to differences in the unfolding forces. Lower/higher unfolding forces could lead to a lower/higher agglutination affinity. How atomic force spectroscopy can be used to answer this question is explained in section 5.2.1.

5.2. Materials and Methods

5.2.1. Probing protein properties with force spectroscopy

Besides the different imaging modes, the atomic force microscopy (AFM) technology is widely used for single molecule experiments. The high resolution in the pN range allows to measure the force acting on a molecule during elongation. By recording thousands of so called force distance cycles and automatized data analysis, statistics of various physical variables of the studied molecule can be achieved. In figure 5.1b the function principle of an AFM is illustrated: a cantilever with a sharp tip scans the substrate while the deflection of the cantilever is detected with a laser beam, reflected on the top of the cantilever. For detailed information basic literature on AFM in general, application to force spectroscopy (e.g.[39, 40, 41, 42, 43]) and a recently published review as starting point for force spectroscopy [44] are recommended. In fig. 5.1a the trace and retrace curve of a force distance cycle are shown and for different positions the situation (cantilever deflection, distance to the substrate, molecule state) is illustrated. During the trace the molecule is at-

tached to the cantilever in its position of rest. The chip, where the cantilever is attached, is moved via a piezoelectric crystal with constant velocity towards the substrate (baseline). From the piezo position on, where the tip (and the molecule) touches the substrate, the cantilever is deflected upwards, as the piezo still moves the chip towards the substrate (linear voltage increase) till the point of maximal upward deflection. Within this time the molecule can bind to the substrate specifically, e.g. to a layer of antibodies, or unspecific to any material. In the retrace the cantilever is still bent upwards.

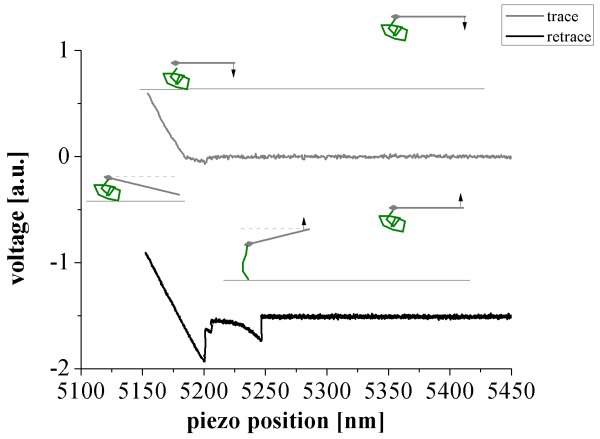

(a) Raw data of a force distance cycle

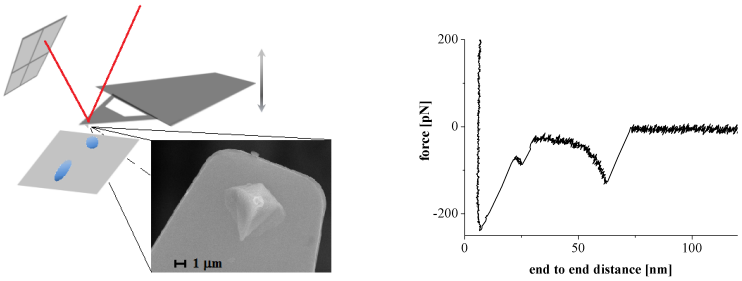

(b) Function principle of an AFM and a force distance curve

Figure 5.1.: (a) Voltage signal for trace and retrace (shifted -1.5V). Inset: schematic deflection of the cantilever at the different positions in the force distance cycle. **(b) left:** Schematic AFM setup: with a four quadrant photo diode the deflection of a cantilever is measured via a reflected laser beam. The cantilever is linked to a chip that is moved vertically with a piezoelectric crystal. **right:** Force as function of end to end distance d of the stretched molecule in the retrace.

When the chip is moved further away from the substrate at some point the molecule gets stretched between cantilever tip and substrate. Thus, the same force acts on the molecule and on the cantilever, what is visible by the negative voltage value indicating a deflection towards the substrate. After the rupture of the last binding site of the molecule, the cantilever is again at rest, while the chip is moved further upwards to the initial position.
From here, the cycle can be repeated several times.
As shown in fig. 5.1c the retrace curves can be converted in force distance curves by multiplying the voltage signal with a calibration factor and cor-

rection of the piezo position by the deflection of the cantilever (see basic literature). The distance d then describes the end to end distance of the stretched molecule. In this figure, besides the rupture at 65 nm, an unspecific rupture (left) and another small rupture (middle) appear. The first one is simply caused by unspecific interaction of cantilever and substrate and also appears in reference measurements without molecules attached to the tip. The latter one can be caused e.g. by another molecule stretched in parallel.

The AFM technology allows to record the force acting on single molecules as function of the protein elongation (force distance curve). These force distance curves for polymers can be fitted with theoretic models. The simplest model is e.g. the freely joint chain model where the monomers are approximated by stiff rods of a certain length. A number of these monomers is connected to a chain, where the angle between neighboring chain segments is free [45].

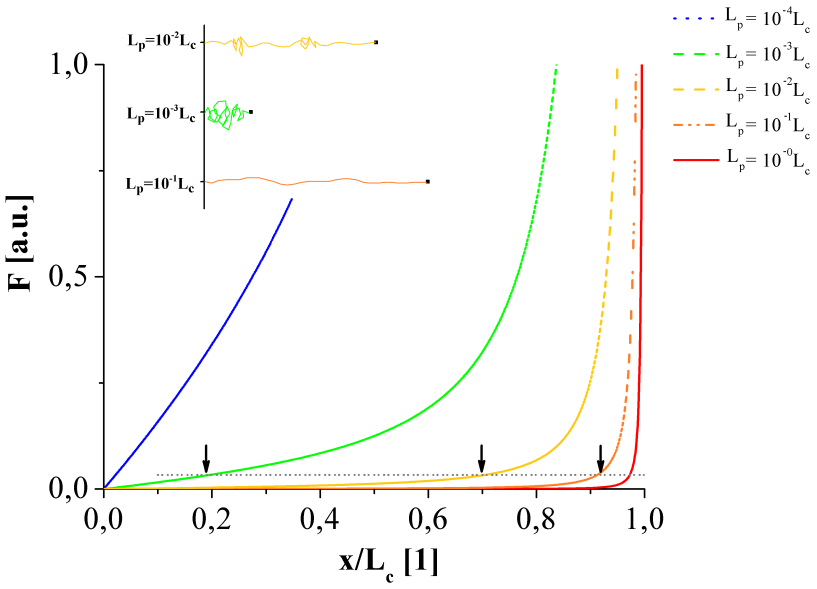

Figure 5.2.: Force F as function of relative elongation of a polymer according to the WLC model for fix L_c and different L_p. The gray dotted line marks the force that is necessary for 70% elongation of a polymer with $L_c = 100\,L_p$. At the same force a polymer with a persistence length, that is one order of magnitude higher, is only 19% elongated. In contrast a polymer with L_p one order of magnitude lower is almost completely elongated. Inset: illustration of elongation of polymers in the situation marked with arrows: at the pulling force, at which the polymer with $L_c = 100\,L_p$ leaves the linear regime, the polymer with the smallest persistence length is still coiled, whereas the one with the longest is almost completely stretched.

Expanding this model from discrete monomers to a continuity model results in the so called Worm-like-chain-model (WLC). The force F as function of the end-to-end-distance x of the polymer follows the formula:

$$F(x) = \frac{k_{\mathrm{B}}T}{4L_{\mathrm{p}}}\left(\left(1-\frac{x}{L_{\mathrm{c}}}\right)^{-2}+\frac{4x}{L_{\mathrm{c}}}-1\right) \tag{5.1}$$

where L_p is the persistence length, L_c the contour length, T the temperature and k_B the Boltzmann constant.

In figure 5.2 the pulling force F as function of relative elongation of a polymer according to the WLC model for fix contour length L_c and varied persistence length L_p is plotted. The persistence length typically is two to three orders of magnitude smaller than the contour length. Thus, the gray dotted line marks the force that is necessary for 70% elongation of a polymer with this typical ratio of L_c and L_p.
At the same force, where a typical polymer leaves the linear regime, where it behaves like an entropic spring, a polymer with a persistence length one order of magnitude lower is only 19% elongated. In contrast a polymer with L_p one order of magnitude higher is almost completely elongated.
This idea is conferred to the studied variants of VWF: In fig. 5.3a it is illustrated that VWF under shear flow switches its conformation from coiled to elongated. Only in the elongated conformation the protein binds platelets and fulfills its function in hemostasis [5]. Assuming that the force field due to the shear flow can be compared with a point force (AFM tip), one can compare the necessary forces to change the proteins conformation for wild-type VWF (WT) and two mutations (2A, 2B). Patients with these mutations tend to lower/higher platelet aggregation, like indicated in fig. 5.3b: a certain concentration of ristocetin leads to aggregation of blood. In analog experiments for the different mutations significant higher/lower concentrations are necessary. This leads to the working hypothesis, that compared to WT the mutations 2A and 2B require higher/lower forces for the change from coiled to elongated conformation like indicated in fig. 5.3c. These mechanical forces can be measured with an atomic force microscope for large number of force distance cycles.
If this mechanical picture, that links different unfolding forces with the clinical malfunctions, is correct, the statistical distribution of the persistence lengths lies at smaller L_p for mutation 2A and at higher L_p for 2B (see fig. 5.3d). Thus, large number of force distance curve under the same experimental conditions for WT, 2A and 2B have been recorded and evaluated with the analysis software described below.

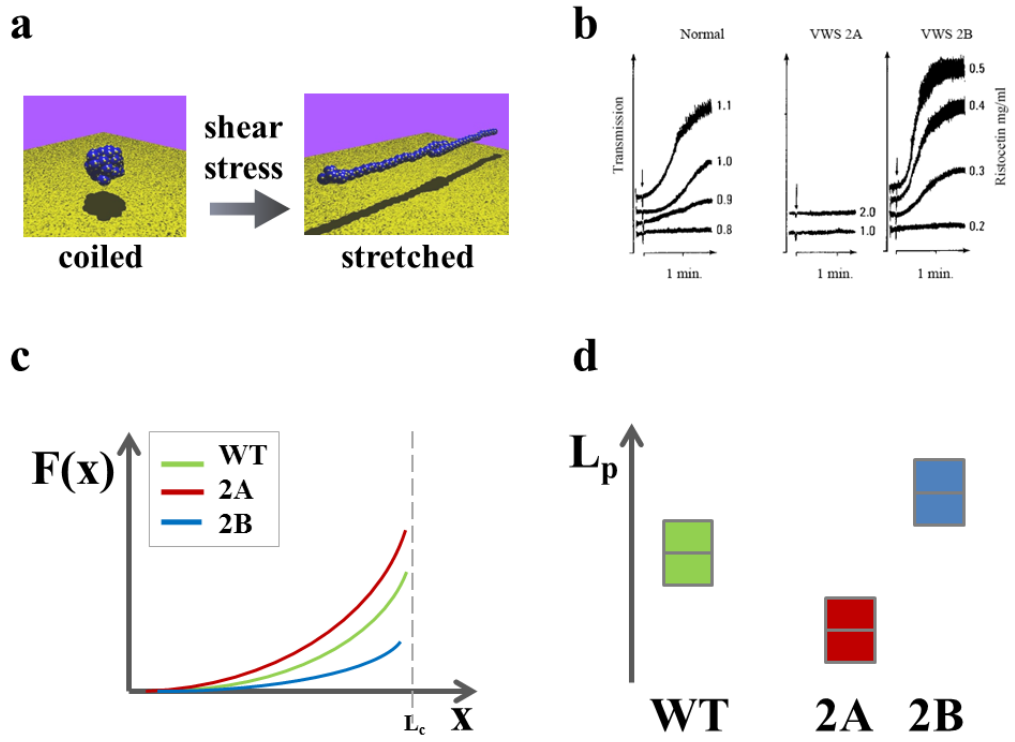

Figure 5.3.: **(a)** Under shear stress VWF switches from a coiled to a stretched conformation [2]. **(b)** The tendency for blood clotting after addition of Ristocetin is decreased for patients suffering from von-Willebrand desease (VWD) type 2A and increased for those suffering VWD type 2B [37]. **(c)** In the working hypothesis the mechanical picture explains the bleeding dysfunction: stretching of 2A/2B needs higher/lower forces than WT. These forces are measured with an AFM. **(d)** From force distance curve L_p for the different VWF types can be extracted. If the mechanical picture is correct, one expects that the distribution of L_p for 2A/2B lies at lower/higher values compared to WT.

5.2.2. Cantilever and Substrate preparation

The force cycles were measured in PBS++ (Dulbeccos PBS (1x) with Ca & Mg, PAA-Laboratories GmbH) at pH 7.4 with a setup like presented before [46]. The VWF was covalently bound to the cantilevers with linker molecules (aldehyde-PEG-NHS, friendly supplied by Dr. H. J. Gruber, Institut for Biophysics, Universtity Linz, 4040-Linz, Austria, see also [47]) according to the protocol shown in appendix A.1. As substrates freshly cleaved mica sheets (Muskovit-Mica-Sheets, Plano GmbH) were coated with the same PEG linkers. If intended, polyclonal VWF antibodies (Dako Cytomation, Denmark, reference A0082, concentration: 3,1g/l) were bound to the PEG-layer (see

also A.1). The complete surface chemistry processes are explained detailed in [46].
In the presented experiments cantilever chips of type MSCT and OTR4-10 (Veeco Instruments Inc., NY 11803, USA) were used. By default the experiments were performed with the softest cantilever of each chip (k=10-20 pN/nm). For similar experiments we recommend the MSCT type because of the better handling during coating and installation into the setup. The specifications of the cantilevers can be found in [46] or on the websites of typical suppliers for AFM accesories (e.g. Bruker AFM Probes, Camarillo, CA 93012, USA).

5.2.3. Automated analysis of force distance curves

To get significant statistics for the different VWF mutations in different experiments several hundreds to thousands of force distance curves were recorded. To analyze these huge amounts of data the implementation of an customizable automatized data analysis software was crucial. The house made software (OpenForce) is a band of scripts running with the freeware SciLab 5.2 (www.scilab.org) and was presented in detail in [46]. In the following section the main requirements to the software, its skills and the key ideas of the used algorithms are given.
OpenForce works in a semi-automatic way. That means, the operator has to adapt the default values in a configuration file, that is adjusted to some of the force curves of the complete data set. One adjusted parameter for example is the so called jump factor: it defines the threshold distance between neighboring points in a force curve indicating a discontinuity that exceeds the mean noise level significantly. With the optimized configuration file OpenForce is able to analyze thousands of force curves automatically. The main steps in the analysis of one single curve are the following.
First, from the raw data file the data columns and values from the header are read. Second, the voltage signal as function of the piezo position has to be transformed into a force signal as function of the distance between substrate and tip of the deflected cantilever. Therefor the baseline, i.e. the signal of the position of rest, has to be fitted (see fig. 5.4a). To convert the voltage signal in a force signal the sensitivity characteristic, i.e. the slope of the signal during pressing the cantilever on the substrate, has to be determined (green line in fig. 5.4a). Subsequently the signal is scanned for discontinuities, so called rupture points (circles in fig. 5.4b). Between the rupture points and the equilibrium points the algorithm fits the data according to the WLC model. Here the fitting parameters contour length L_c and persistence length L_p are varied repeatedly on a parameter grid according to the least square method. This detection and fitting step is repeated for a second time, while new rup-

ture points within the fitted ranges are determined by discontinuities in the difference of fit curve and data signal.

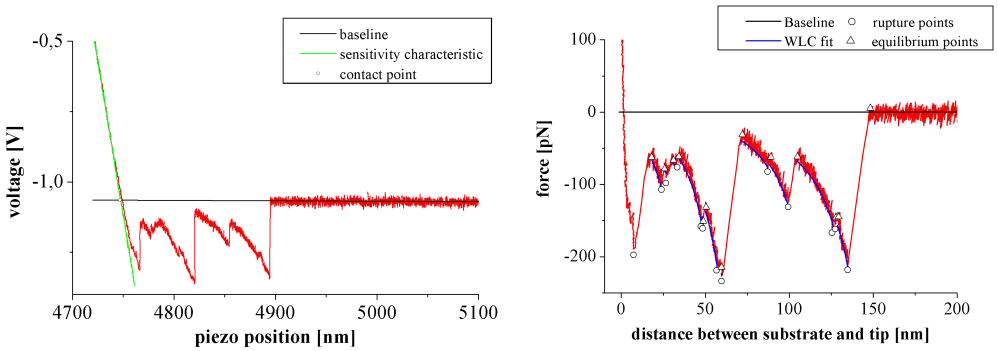

(a) Baseline and sensitivity fit

(b) Cutout of an automatically analyzed force distance curve.

Figure 5.4.: (a) Fitted baseline and sensititvity characteristic as initial steps of the analysis. **(b)** In an automatically analyzed force distance curve the circles mark the detected rupture points, the triangles the equilibrium points. Between this points the software fits WLC curves to the data points (blue line).

Then the force curve and the proper fits are plotted in the intended format. Finally the results, i.e. rupture and equilibrium points, fitting parameters L_c and L_p and other values like a quality factor of the fit are saved into a result table. Usually the contour length is defined as the length of the polymer backbone, but in pulling experiments fractions of the complete backbone can be hidden in folded domains. Furthermore it is possible and probable that the polymer is not pinned with its end to the cantilever tip. Therefore, in the following the contour length L_c is always ment as the available or measureable contour length of the protein.

After this analysis process is applied to all force curves of the data set the table of results can be sorted and evaluated with a further script in a convenient and quick way. A very detailed description of each analysis step is recommended for further information (see[46]).

5.3. Results and Discussion

The structure of the following results and discussion section is divided in five parts. First, to develop an intuition for the VWF force curves, measurements

of WT and fits to these force curves are shown. Second, the results of WT measurements are compared qualitatively with calculations and quantitatively with Monte-Carlo simulations to clarify the structure of the fit results in the L_p-L_c-space and to ensure comparability. Third, characteristics of VWF 2A measurements are shown and discussed. Subsequently the results of fits to these measurements are presented and discussed. To avoid unnecessary repetitions, the separation of results section and discussion section is omitted here. Then the same approach is used for VWF 2B.
Afterwards, in brief the obtained results of WT, 2A and 2B are compared. Finally the correlation of clinical malfunctions and mechanically measured protein elasticities are discussed and in an outlook possible continuative experiments are suggested, which can also help to unravel similar subjects.

5.3.1. Results - Force curves of wildtype VWF

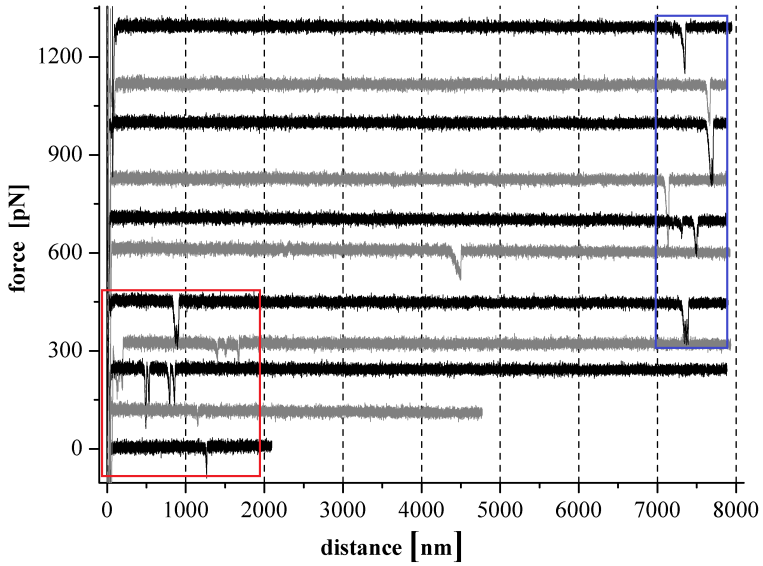

Figure 5.5.: Forces curves of VWF WT (baselines are shifted vertically).

In fig. 5.5 examples of force curves of VWF WT are plotted. Ruptures appear over the whole range up to 8 μm. Next to the rupture point most curves show typical WLC behavior. A closer look on these regions (fig. 5.6b = blue box) demonstrates that within the dips additional discontinuities (in the following called ruptures) appear. In many previous measurements the force curves look

similar to the second curve (numbering from top) in fig. 5.6a or even just like the first 1000 nm of it. Often the unspecific adhesion peak seemed to be the only interaction between tip and substrate.
Curves like the top five curves in fig. 5.5a suggest that simply the measured height range moved within the low force regime of protein stretching where eventual events cannot be seen due to the noise level of the AFM. Initial sections of such curves often cannot be distinguished from a real baseline without a connection between tip and substrate. This should be kept in mind for the discussion of the fitting results.

The analysis of several thousands of force curves are results in form of tuples in the L_p-L_c-space, like exemplarily shown in fig. 5.7. For the data set ‚A8D' no manual selection of fitted force curves was done. For ensuring satisfyingly high quality of the fits filtering criteria like minimum number of data points, or fitting quality factor as described before [46] were used. In contrast, for the data set 'A11I' force curves with ruptures at high distances were selected (examples shown in fig. 5.5).

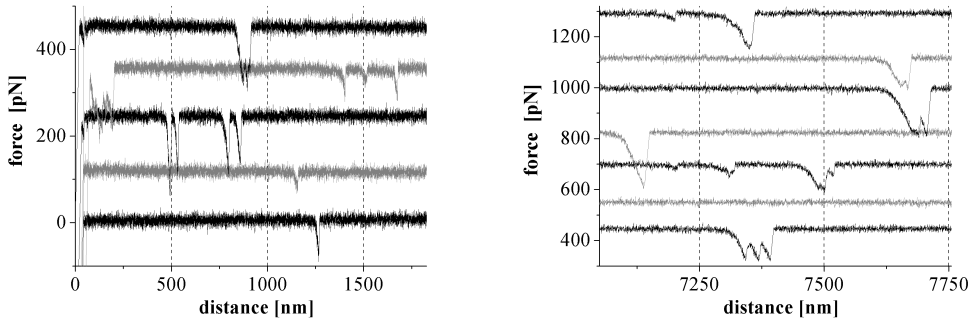

(a) Zoom (red box) (b) Zoom (blue box)

Figure 5.6.: Forces curves with VWF WT (baselines are shifted vertically). No obvious quantization in rupture distance can be seen in single force curves. **(b)** Also at high elongations single and multiple rupture events appear.

In fig. 5.7 the results of the fits to force curves of VWF WT are shown. The parameter contour length L_c is plotted as function of the persistence length L_p. The fit tuples (L_p,L_c) of a series of WT force spectra show accumulation of data points in three regions. The region in the left upper corner is mainly caused by fits to low number of data points and therefore an artifact.

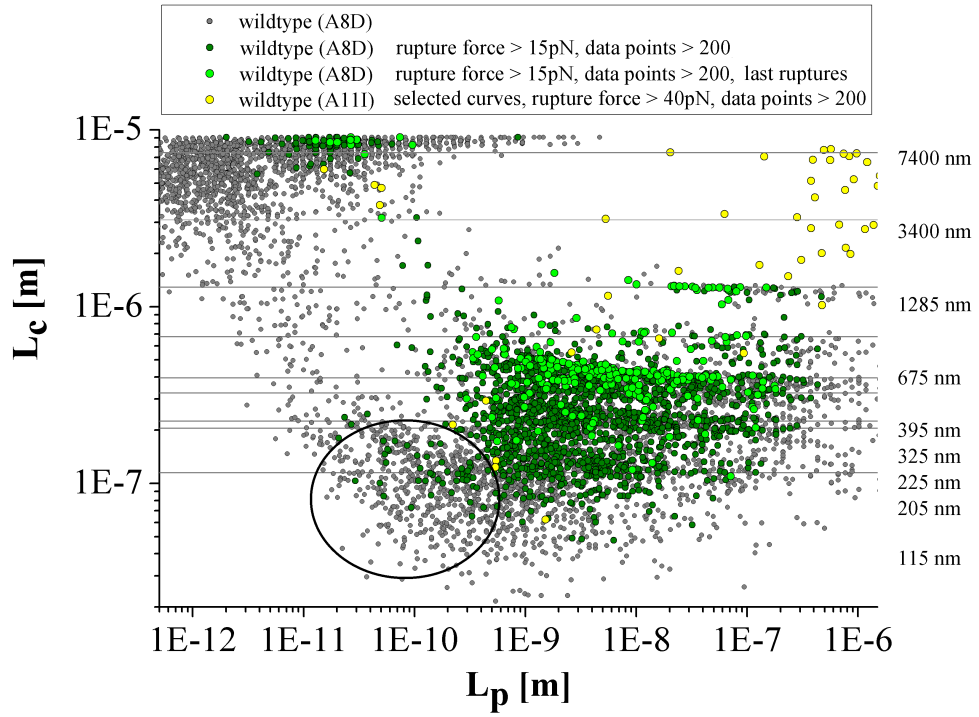

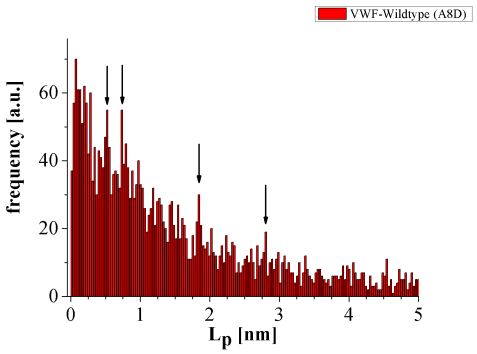

(b) Histogram of persistence lengths

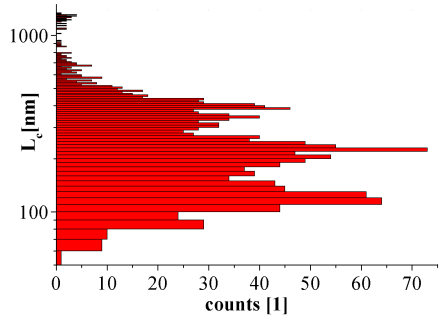

(c) Histogram of contour lengths

Figure 5.7.: (a) Fit tuples (L_p,L_p) of a series of WT force spectra show accumulation of data points in three regions. The region in the left upper corner is mainly caused by fits to low number of data points and an artifact. The region marked by the ellipse are fits to sections of high forces below 200 nm distance between tip and substrate. The remaining fits indicate a quantization of L_c and a broad distribution of L_p between 1 nm and 1000 nm. **(b)** Histogram of the fitted persistence length of WT VWF shows maxima (arrows), that can be explained with identical parallel VWF strings. **(c)** Histogram of the fitted contour lengths of WT VWF shows a quantization.

The region marked by the ellipse are fits to sections of high forces below 200 nm distance between tip and substrate. The remaining fits indicate a quantization of L_c and a broad distribution of L_p between 1 nm and 1000 nm. This region turned out to be the region with the most information about the basic polymer properties, as shown in the discussion section. The magnification of the relevant part of the L_p-L_c-space is plotted in fig. 5.7b. The histogram of the contour lengths of the data set ‚A8D' in fig. 5.7c shows maxima roughly located at multiples of the length of a VWF dimer. This quantization already can be seen in the distribution of the rupture distances of the raw data. Furthermore also the histogram of L_p shows maxima (see arrows in fig. 5.7b) that can be explained by pulling of parallel strings with the same persistence length as described in section 5.3.2 and in [46].

5.3.2. Discussion - comparison of measurements and simulations

Discussion - Qualitative comparison of measurements and simulations

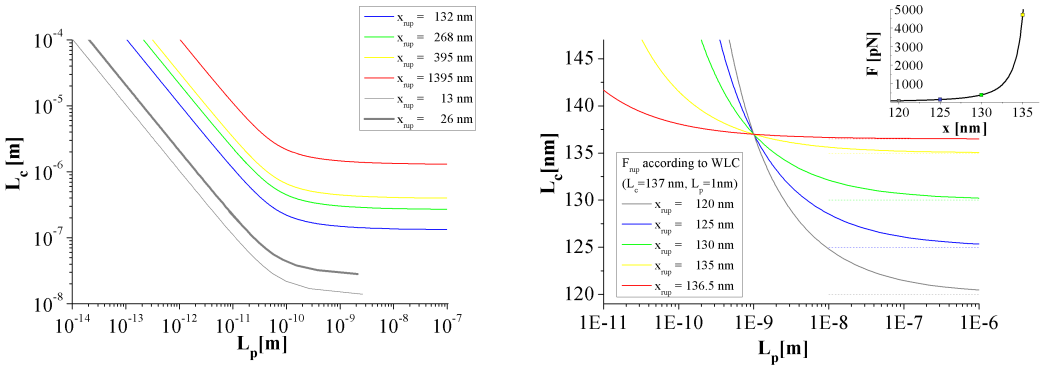

(a) Possible solutions for fixed F_{rup}

(b) Possible solutions for distinctive points of a WLC curve with fixed L_c and L_p

Figure 5.8.: **(a)** $L_c(L_p)$ for fixed F_{rup} gives a similar structure as the measurements(5.7a). The two gray lines symbolize short rupture distances (PEG-linkers) while the colored ones represent multiples of a dimer size **(b)** Possible solutions for ruptures at different relative elongations. Ruptures at different points of the same WLC force curve (see inset) produce different possible $L_c(L_p)$ solutions. With increasing relative elongation the solution curves are more flat in the vicinity of the real solution (intersection of all solution curves).

Structure of the results in the L_p-L_c-space The structure of the fit results in the L_p-L_c-space can be understood by solving eq. 5.1 for $L_c(L_p)$ for a fix

rupture point (x_{rup}, F_{rup}). In figure 5.8 L_c is plotted as function of L_p for $F_{rup} = 75$ pN and four different rupture lengths that are close to the maxima of the L_c histogram (fig. 5.7c). Furthermore the thin and thick gray lines are the possible solutions for x_{rup} near one respectively two times the length of the used linker molecules. The L_c limes for high L_p is, independent from the rupture force, obviously the rupture distance. These horizontal asymptotes can be found in the results of the fits to the measurements as well. Interestingly the high quality fits are found especially in this region.
In fits, where x_{rup} is not in the vicinity of the fitted L_c, i.e. mainly fits in the upper part of the L_p-L_c-space, leads to very small values for L_p. Recalling the elongation force according to the WLC model, this means the linear part of force curves, far away from the maximal elongation, are placed through the rupture points. This also explains why fits with short ranges and/or lower quality can be found especially in this region.
Every possible solution for one rupture point tuple (d_{rup}, F_{rup}) lies on the line corresponding to the particular tuple. A change in the rupture force varies in this double logarithmic plot only the slope of the linear part but not the limes towards high L_p. Anyway the rupture force is determined by the strength of the binding of VWF to the substrate. Thus, for the comparison with the measurements F_{rup} can indeed be assumed as nearly constant.
One basic assumption is that the studied proteins somehow possess a certain persistence length distribution. As no specific binding sites are used in the experiments, at first glance there is no reason to assume quantization of L_c. But it is thinkable that the rupture takes place at different positions within the elongation force according to the WLC model. This influence on the shape of the line of solutions is analyzed in fig. 5.8b. For fix model parameters ($L_c = 137$ nm, $L_p = 1$nm) different rupture points (x_{rup},F_{rup}) near to the vertical asymptote are used to calculate $L_c(L_p)$. They represent relative elongations between 87.6% and 99.6%. It is observable that with increasing x_{rup} the possible solution curves are more flat in vicinity of the real solution. Furthermore in consequence of the initial conditions all lines intersect at that tuple, that describes the used model parameters. This originates the higher reliability of fits that include wide spread data points: those fits simply have to fulfill more conditions. Only solutions in the vicinity of the correct tuple fulfill these conditions sufficiently.
To sum up this paragraph: the structure of the solutions in the L_p-L_c-space can be understood by quantization of rupture distances especially for the high quality fits to the data points of the last rupture. In the following section the comparison with simulations of domain unfolding will further clarify what information can be won from the measurements.

Discussion - Quantitative comparison with a polymer model using a Boltzmann ansatz for domain unfolding

The in-depth studies of the force spectra, and the fitting results suggest that the force spectra result from several parallel VWF polymers which each consists of a series of moduls that hide a certain inaccessible part of the polymer backbone. The opening of this domain like substructures in a single fiber lead to an increase of the contour length and hence to the typical saw tooth pattern in the force spectra. Based on the simpler calculations in [46] sophisticated simulations using a Boltzmann-ansatz show high agreement with the measurements. Thus, a fraction of this unpublished data [48] is used here to present the up to date status concerning force spectroscopy on VWF.
A simulated single VWF polymer consists of a series of moduls (from here: domains) described according to the WLC model and the properties (L_c, L_p). Thus, a elongation x_i of the domain i results in an acting force $F_i(x_i)$ on this domain. In a chain the force acting on each domain is the same. Furthermore, the total elongation of the chain is the sum over the elongation x_i of all domains.
Each of these domains expose a hidden part of the polymer with a probability p_i that is exponentially dependent on the force, acting during a infinitesimal time step Δt:

$$p_i(F) = k_{0,i} e^{\frac{F}{F_0}} \Delta t \tag{5.2}$$

where $k_{0,i}$ is the unfolding rate without acting force and F_0 a characteristic force. By adjustment of these parameters this probability can be used also for the unbinding from the substrate.

Simulated force curves show very good agreement with the measured curves for the following sample structure. Three identical polymers are on both sides attached to substrate/cantilever via a PEG linker ($L_c = 15$nm, $L_p = 0.5$nm) and consist of four dimers (L_p=100nm) which are build up of three domains ($L_c = 105\,\text{nm}$, $10\,\text{nm}$, $6\,\text{nm}$) each with $L_p = 100\,\text{nm}$. All domains are closed initially, simulating the globular conformation of the protein. Thus also the end to end distance is zero. Typical values for domain opening forces, opening rates, detaching forces etc. can be found in appendix A.2. In figure 5.9 a simulated force curve is shown. Noise in the typical order of magnitude is added to the simulated force distance curves in order to compare fitting results of these simulated force curves with measured ones. A detailed study of the impact of the different simulation parameters on the result of the fits to the simulated force curves will be presented in [48].
The exemplarily shown force curve in fig. 5.9a is in many respects similar to a typical measured curve. After an unspecific adhesion dip, the curve shows typical WLC shaped force increase, interrupted by around ten ruptures. For

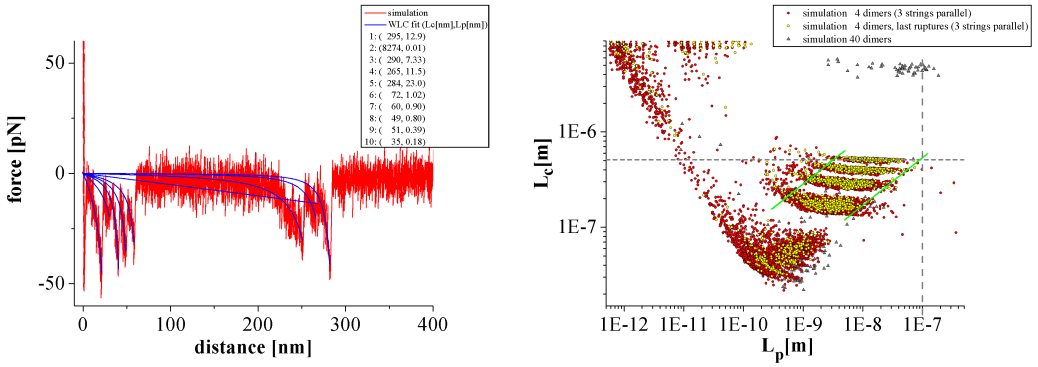

(a) Simulated force distance curve

(b) Results in the L_p-L_c-space

Figure 5.9.: (a) The simulated force distance curve look similar like the measured ones. **(b)** Results of fits to simulated force curves. Three parallel polymers with $L_p = 100$ nm are build of 4 dimers which each consist of three domains of the size 105 nm, 10 nm and 6 nm. On both sides of each polymer a linker molecule is attached ($L_c = 15$ nm, $L_p = 0.5$ nm)

the discussion of the abilities and limits of the fit algorithm we count the fits from right to left. The baseline and the contact point are determined correctly, the rupture points are identified and the fits 1, 3, 4, 6 and 10 seem perfect. In contrast fit 2 is very short ranged and produces an unrealistic tuple of fit parameters. At first glance fit 5 is also satisfying, but a close look to the fitted section shows that the deviations are not complete randomly distributed. The other fits 7, 8 and 9 are sufficient but the human eye would tend to construct a steeper curve into the data points. Thus, it is not surprising that the fitted parameter L_p names never exactly the intrinsic L_p=100 nm. Moreover the fitting results are spread over three orders of magnitude.
This broad distribution of the persistence length is problematic if only single fits are picked out. But keeping the shape of all possible solutions (fig. 5.8) in mind, a look at the resulting distribution of the fitting results in the L_p-L_c-space removes the confusion. In fig. 5.9b the red points are the results with a fitting quality of 0.7 or higher of all fits in 3000 simulated force curves, the yellow ones are the fits to data points before the last rupture. Obviously the parameter tuples reflect the typical shape of the possible solutions to a $(x, F(x))$ tuple as shown before. Astonishingly the fits to the last ruptures do not deviate strongly from the other fits. This indicates that rupture of parallel polymers at the same time (within the resolution of the sampling time) appears more often than expected and will be discussed in detail in [48]. From the theoretical considerations before, we can explain the plateaus in L_c with the quantization of the building block sizes. For example the gray dashed horizontal line is exactly the maximal length of a simulated polymer.

On the other hand, the lowest values of L_c are next to 30 nm the length of two linker molecules.
However, the most important aspect is the fact that the broadening of the persistence length on the plateaus seems to be very systematic (the green straights in this double logarithmic plot are multiples of the square route of L_p). Especially the simulation results of a string with 40 dimers show that this trend in the shift of L_p with increasing L_c saturates. The resulting values of L_p do not exceed significantly the intrinsic value of L_p=100 nm. Decreasing the noise level in the simulations leads to an expansion of the lower L_c-plateaus towards the intrinsic limit of L_p=100 nm. Furthermore in the following paragraph it will be shown, why the accumulation of measured fit tuples are limited differently for different contour lengths.

The WLC model can be simplified for $1 - \frac{x}{L_c} << 1$ to:

$$F(x) = \frac{k_\mathrm{B}T}{4L_\mathrm{p}} \left(\left(1 - \frac{x}{L_\mathrm{c}} \right)^{-2} \right) \tag{5.3}$$

The dependence of L_c on L_p and elongation x then can be derived as:

$$L_c = x \frac{1}{1 - \sqrt{\frac{k_\mathrm{B}T}{4FL_p}}} \tag{5.4}$$

Thus, for a data point (x, $F(x)$) and fix L_p obviously higher values of x lead to a higher estimation of L_c. Furthermore the limes for high L_p is again the rupture distance x. Using the simplified equation 5.3 to express L_p allows the following inequations:

$$L_\mathrm{p} = \frac{k_\mathrm{B}T}{4\left(1 - \frac{x}{L_\mathrm{c}}\right)^2} \frac{1}{F(x)} \overset{F<F_{max}}{>} \frac{k_\mathrm{B}T}{4\left(1 - \frac{x}{L_\mathrm{c}}\right)^2} \frac{1}{F_{max}} \tag{5.5}$$

and

$$L_\mathrm{p} = \frac{k_\mathrm{B}T}{4\left(1 - \frac{x}{L_\mathrm{c}}\right)^2} \frac{1}{F(x)} \overset{F>F_{min}}{<} \frac{k_\mathrm{B}T}{4\left(1 - \frac{x}{L_\mathrm{c}}\right)^2} \frac{1}{F_{min}} \tag{5.6}$$

A limitation of the force by a certain detaching force F_{max} can be safely assumed. The reason why F_{max} differs with polymer length lies in the model itself: the detaching probability is accumulated over the time steps. Hence, at constant pulling velocity high polymer lengths need a higher number of time steps and thus already a lower average force leads to the same detaching probability p in longer polymers than in shorter ones.
Along the same line, it is reasonable that long polymers are correlated with a smaller lower limit F_{min} what leads to a higher upper limit of L_p. This argumentation of accumulated probability seems satisfying, as it answers the question for both limitations at once. Furthermore, for very short polymers

the impact of the lower persistence lengths of the linker molecules on the measured total polymer lengths is higher than for longer ones.

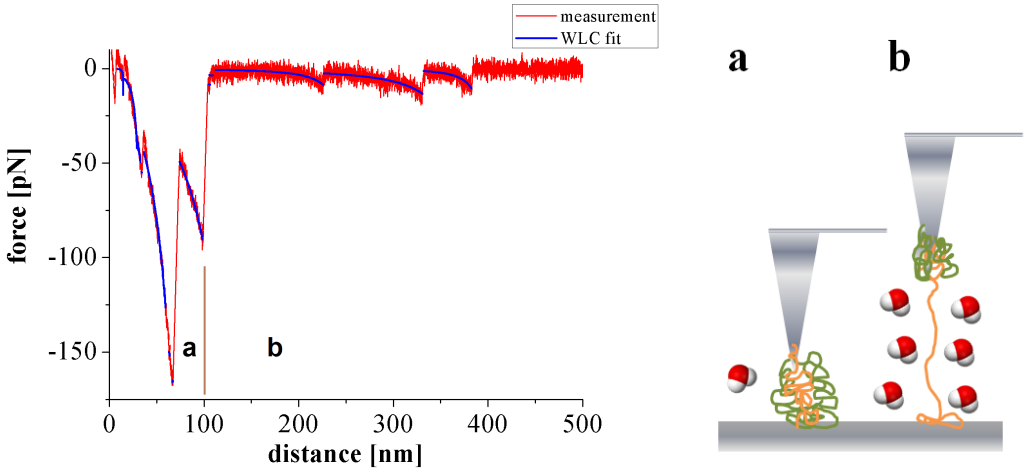

Figure 5.10.: left: Measured force curves show high force regimes below 100nm .**right:** Illustration of the regime, where intermolecular friction dominates (a) and at higher distances, where interaction with water dominates the forces (b)

Nevertheless, there are some differences between simulation and measurement that should be explicitly mentioned as it appears over all data sets and VWF types. As can be seen e.g. in fig. 5.10, in many measured force curves below an elongation of 100 nm a significant higher force regime appears than predicted by the simulations. The forces reach values around 300 pN while typical forces at higher distances are 20 pN.

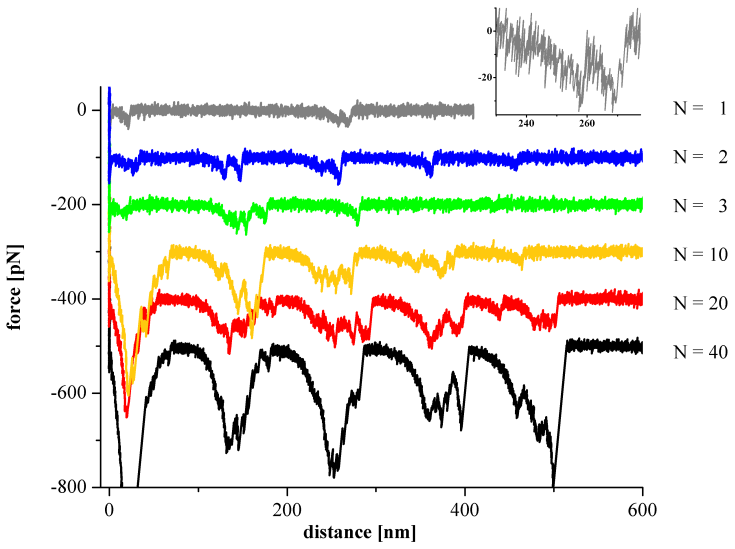

Figure 5.11.: Simulated force curves with N identical parallel polymers show a systematic increase of appearing forces.

A possible trivial reason is the number of parallel strings. In the simulations

shown before up to three polymer strings were pulled in parallel. In real measurements this number for sure can exceed three. Hence, higher total forces are applied to the cantilever. But this would not explain the sharp limitation of this high force regime, as examplarily chosen simulated force curves in fig 5.11 show. There force curves for 1 to 40 parallel but not directly interacting VWF polymers are depicted. The interaction only happens in the way that they are all connected to the same force sensor. As a consequence the appearing forces increase systematically with increasing number of polymers. But the fits still do not produce the abrupt change of the appearing forces around 100 nm and the fit tuples do not lie in the region marked in 5.7a with an ellipse.

On the other hand one could imagine, that the pulled VWF system shows two regimes, as illustrated in fig. 5.10b. At low distances between cantilever tip and substrate complete VWF globules are extended and behave somehow gel-like. Internal friction dominates the acting forces. At higher distances there is a regime where single strings are pulled out of the coiled VWF and the interaction with water dominates. This assumption is supported by the fact that at higher VWF concentrations in the coating process the gel-like regime is increased up to 2 μm. Furthermore through all measurements (different preparation, VWF mutations and batches, different substrate coatings) it turned out that two main ranges of L_p in fits with high quality appear. On the other hand there are the plateaus in the L_p-L_c-space, reaching up to roughly 100 nm, which were discussed before. These measurements are thought to describe the case of elongation of single molecules. On the other hand in fig. 5.7b a region around 0.1 nm is marked with an ellipse. These two regimes also appear in the measurements of VWF 2A and 2B.
For the quantitative answering of the question about the differences between the mutations the single molecule measurements may be better suited. But in physiology the single molecule case is unlikely, as the network formation of the VWF fibers is the basic process in primary hemostasis. Thus both regimes will be compared and discussed.
The explanation of this effect with the interaction of parallel PEG-PEG-combinations (substrate-cantilever) is excluded because of their shorter length ($\approx$ 15 nm each). In turn, a characteristic PEG-PEG-interaction should be visible in the distribution of the relaxation forces. This is not the case as shown before [46]. Furthermore the extension of the high force regime to high rupture distances with increasing VWF concentration argues against the scenario of PEG linker molecules as origin.

At this point it has to be emphasized that the appearance of only one characteristic relaxation force, combined with the good agreement of the simulation and measurements for the single or "few-molecule" case furthermore indicates,

that these effects in the measurements that agree with the simulation are not domain unfoldings in the common sense. They rather reflect the rupture of PEG-VWF bonds at the substrate. Hence, the quantization of L_c in multiples of the dimer length also indicates that these bonds are not randomly distributed over the protein.
Summing up, the considerations gotten by the comparison of measurements, simulations and the structure of possible solutions in L_p-L_c-space, have shown that the broad distribution of measured persistence length implies not categorically a real broad distribution of the persistence length of the polymer itself. In fact, it has been shown clearly that the typical measured fit tuples hint on an intrinsic persistence length in the range of 400 nm - 1000 nm. Such values of L_p are higher than typical reported ones. It simply serves as a parameter characterizing the appearing forces to stretch the polymer. Thus, to compare the results of different VWF types a mean value seems not a good choice. Instead of mean values the results in the L_p-L_c-space and especially the upper limits of accumulation of tuples for high contour lengths are a better comparable value.

5.3.3. Results & Discussion - Force curves of mutated VWF 2A

The appearance of mutation VWF 2A in patients, suffering from VWD 2A, leads to decreased agglutination, as mentioned before. Therefore, in this section force curves of VWF 2A are studied. On the one hand, one cannot distinguish single force curves of the different mutations and the majority of the force curves looks similar as the typical force curves of VWF WT presented before. On the other hand, there are indeed some characteristics that appeared in the force curves of VWF 2A, namely compared to the measurements before, very long VWF fibers with high persistence length and the appearance of quantized force plateaus with a length up to microns. At first, these characteristics will be shown and discussed. Then the results in the L_p-L_c-space are shown and compared to the according results of the WT measurements as drom the section above it follows that not the mean value but more the complete distribution of the fit tuples gives insight into the intrinsic parameter persistence length.

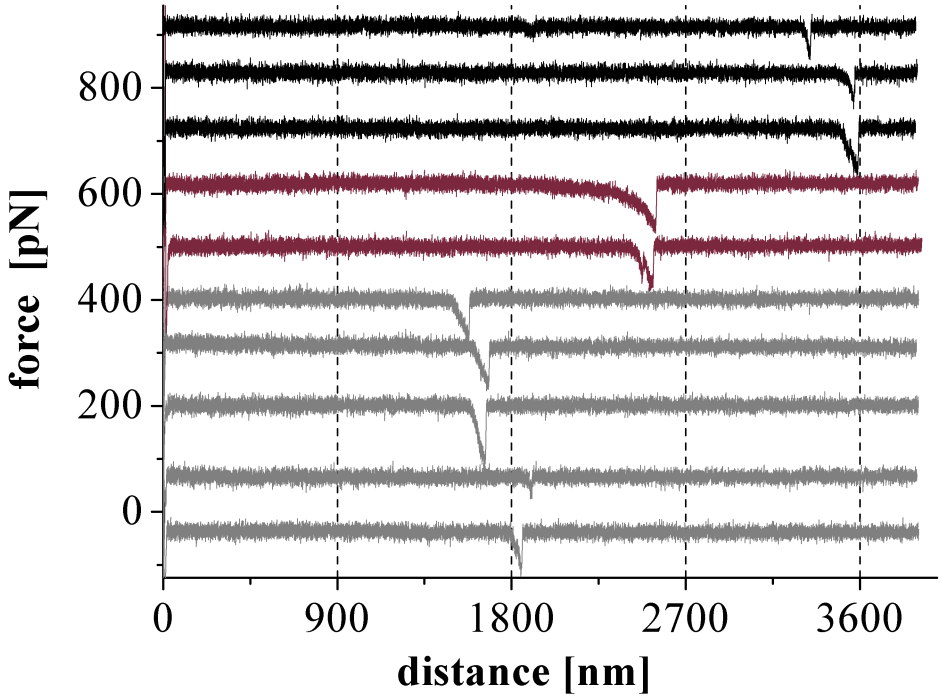

Figure 5.12.: A selection of force curves of VWF 2A. The baselines are shifted for clarity. Different colored curves show contour lengths around different multiples of 900 nm.

As mentioned before in the measurements of VWF 2A besides the typical saw tooth patterns frequently curves like shown in fig. 5.12 appeared. These curves show rupture distances up to five microns and in some cases even higher. Furthermore the persistence length reaches values between 3 nm and 400 nm. Fig. 5.13 shows the fit to the second curve in figure 5.12. Here an excellent fit to the force curve shows a persistence length of 337 nm. The inset shows a magnification next to the rupture point. In this case by eye no additional domain unfolding events can be seen. This might be the reason why here these large values for L_p can be detected by the fitting al-

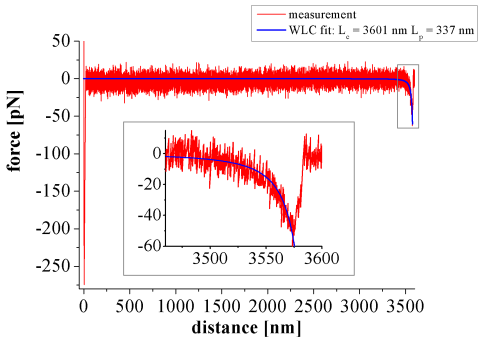

Figure 5.13.: A excellent WLC fit to curve 2 from fig. 5.12 shows a persistence length of 337 nm.

gorithm automatically. If domain unfolding events, too small to be detected clearly, would take place, the mean slope would be smaller leading to lower fitting values of L_p. But these large values of L_p differ significantly from the mean value of all measurements. The possible explanations for the measurements of such high L_p in these very long polymers are already discussed in section 5.3.2.
Another interesting phenomenon is the appearance of very long quantized force plateaus in the force curves of VWF 2A. In figure 5.14 exemplarily the different characteristic types of plateaus are presented. The force curves are numbered from top to bottom of the figure. The most curves have in common that there is a initial short unspecific adhesion peak followed by a region of low force. In this region eventual events take place within the noise level of roughly ±20 pN. The length of this region reaches from dozens of nm up to several microns. The appearing plateaus show a steep force increase up to a certain force F_p between 50 pN and 300 pN at the end of this low force region. With increasing distance this plateau force F_p is held more or less constant before the force increases with a much lower slope and then drops to zero (see curve 4) or immediately drops to zero (see curves 1-3).

The following plateau types appear. Clean plateaus (see curve 1,3), plateaus with a force increase at the plateau end (see curve 4 and 6-8) and plateaus with a fringy region within (see arrows at curve 6 and 7) or before (see arrow at curve 8) the force increase of the plateau. Furthermore curves with more than one plateau region can be observed (see curve 4). For the understanding of the plateaus the region of force increase and the constant force region are from special interest. A closer look to this regions is given exemplarily in the insets a and b in fig. 5.14. The position within the force curve are indicated by the ellipses.

In inset *a* it can be seen that within the force increase several unfolding events take place. While the complete force increase region often cannot be fitted with the WLC model, the sections between the rupture events can. Thus, the force increase can be understood as a sequence of unfolding events, each with a small extension of the contour length. This assumptions is supported by curves like curve 6-8, where the additional contour lengths are bigger and hence, the saw tooth pattern, typical for unfolding events, is more pronounced.

The force plateaus themselves simplified can be understood as sections affected by friction force, as if the partly elongated protein would be slipping over the substrate as soon as a certain force F_p is reached. A closer look shows that the according regions are not just plateaus superposed with a random noise signal. In the magnification (inset b) it can be seen that the plateau is a sequence of dozens of short sections with WLC like force increase interrupted by rupture events around F_p. These observations suggest two scenarios that have to

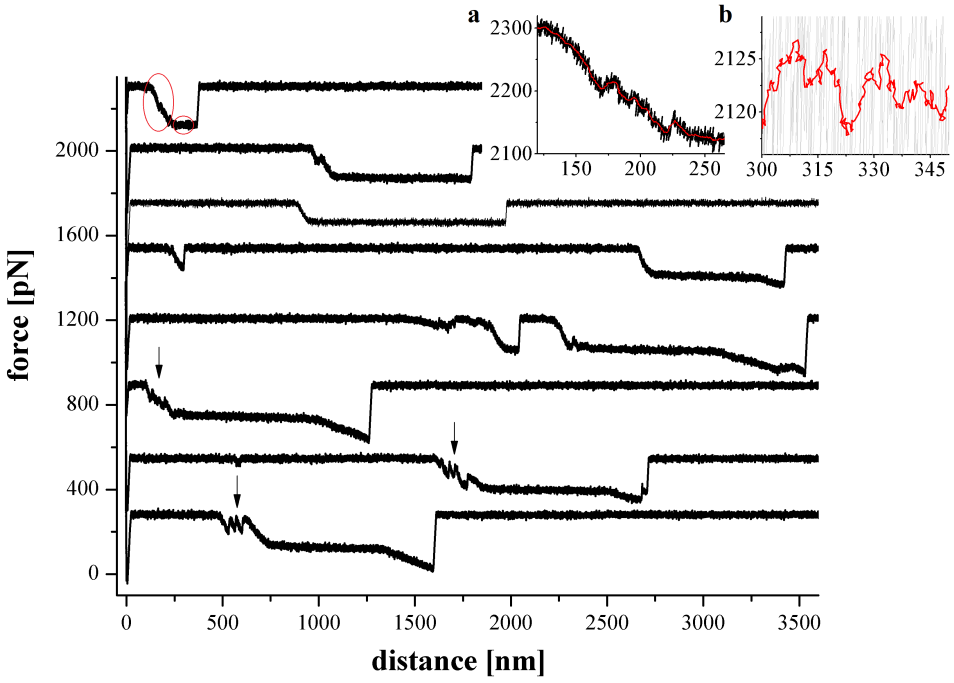

Figure 5.14.: A selection of force curves of VWF 2A shows the different types of force plateaus. The baselines are shifted for clarity. The insets show a magnification of the marked parts of the top curve: (a) the force increase consists of a series of rupture events. (b) also in the force plateau unfolding events can be detected. The force increase at the beginning of the plateau in some curves also shows a more pronounced saw tooth pattern (arrows).

be tested: a slipping of the protein over the substrate versus a sequential mechanical breaking of the binding sites between VWF and the polyclonal VWF antibodies on the substrate surface, like indicated in fig. 5.15.
At first glance the scenario of a slipping protein on the substrate surface seems to be obvious. The tip moves away from the substrate till the part of the protein, which is not adhered to the substrate, gets stressed. The adhesion force keeps the protein attached to the surface while the cantilever tip pulls at the other end. The force increases until unfolding events, comparable to the experiments shown before, appear. At a certain threshold force the adhesion force is exceeded and the protein slips over the substrate.
As the pulling direction is mainly orthogonal to the substrate plane with increasing height h (see fig. 5.15b) the length of the protein slipping over the substrate should decrease. As the friction is proportional to the length of the polymer a decrease in force would be the consequence. Along the same line the arbitrary fractions of adhered VWF would lead to a broad distribution of F_p.

Both effects are not the case. Thus, this scenario cannot explain the appearing plateaus in a satisfactory manner.

A slight deviation from the scenario is a slipping protein, where at the plateau force a series of small domains are unfolded. When all domains are unfolded the force further increases until the friction is transfered and the protein detaches from the surface. Also here a contradiction to the quantization of F_p (shown later in fig. 5.17 appears. Furthermore the question raises, why these extreme long series of small domain unfolding events does not appear in that way in other force curves at this force level. Even if complex situations could answer this question, we prefer a scenario with less assumptions.

Finally, the scenario of a series of breaking the bonds between VWF and the VWF antibody covering on the substrate is discussed. Fig. 5.15a illustrates the situation: the protein is bound at several locations on the substrate. Every bond can stand a certain force F_p. Analog to the first scenario there is a low force region in the force curve until the unbound part of the protein is stretched. The pulling force now acts on the first bond and increases. During the increase several more or less random sized unfolding events take place. This can explain the partly fringy force increase at the beginning of the plateau. As soon as the plateau force is reached the first bond breaks and the contour length is increased for the length of the protein fraction between the first and the second bond. As a consequence a little decrease in force is detected. Due to the further elongation of the protein also the second bond breaks. This process is repeated till all bonds between antibody covering and VWF are broken and the force drops to zero. The angle α will increase with increasing number of broken bonds.

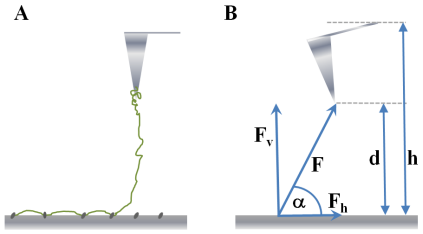

Figure 5.15.: **(a)** Serial unbinding of bonds between VWF and VWF antibodies on the substrate. **(b)** Decomposition of the pulling force in a vertical and a horizontal component. The end to end distance of the protein d and the height h of the chip above the substrate are defined.

As a consequence, to keep the horizontal component of the force constant the total force will increase. This can explain slight increases of the force within a plateau. If the distance between two binding sites is unusually large compared to the mean distance a drop to zero followed by another plateau at the same force would be the consequence. Indeed such effects are observed (compare curve 5 in fig. 5.14). A possibility to testify this hypothesis would be a comparison between measurements with different antibody concentrations for the substrate covering. The mean distance between the binding sites should

increase with decreasing antibody concentrations. As a consequence the saw tooth pattern within the plateau should increase with decreasing concentration until the plateaus disappear below a certain concentration. This effect should not appear, if the plateau is caused by a long series of domain unfolding events as named in the second scenario.

However, we consider the last scenario as the most likely. For completeness the mentioned quantization of the plateau forces will be studied in the following paragraph. The force curve shown in fig. 5.16 is an example for the appearance of multiple plateaus. Besides the plateau at 150 pN a second plateau around 285 pN can be seen.

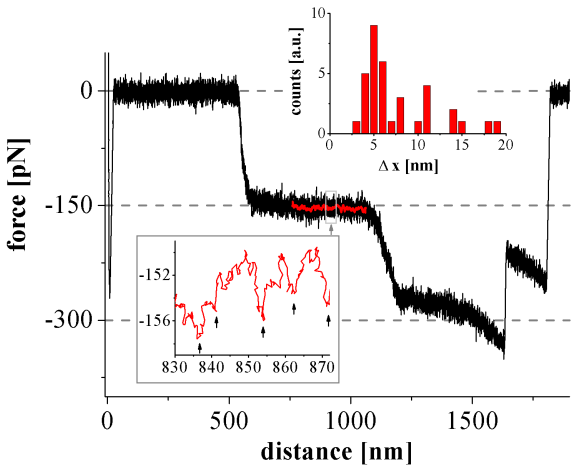

Figure 5.16.: Exemplarily a force curve of VWF 2A showing plateaus at different forces. The second plateau force is roughly twice the force of the first one. **lower inset:** Magnification of the first plateau. Averaging allows to determine the rupture events within the plateau. **upper inset:** Distribution of the differences in rupture distance of the ruptures within the first plateau (red line).

In many curves it also happened, that the force increase at the end of the plateau reaches roughly double the plateau value before the force drops to zero. This can be understood if two proteins parallel are stretched and ripped off from the substrate. To show that the quantization of F_p is objective measurable, the 1720 force curves of a series of measurements were evaluated manually. The histogram of the 234 evaluable plateaus is plotted in fig. 5.17. The arrows indicate maxima near multiples of 50 pN. For higher precision the software Openforce could be adapted to evaluate besides F_p also the plateau lengths. But already these preliminary measurements allow to predict a characteristic unbinding force between VWF and antibodies of 50 pN at a loading rate of $20nNs^{-1}$. Furthermore in fig. 5.16 the distances Δx between the rupture events (see arrows in the lower inset) in the red marked part of the left plateau are evaluated. The histogram (upper inset) shows maxima at 5 nm and 11 nm.

An automated analysis of several hundred plateaus could in such way give insight into the distance between binding sites, either on the substrate, or if the substrate is saturated on the protein VWF. It has to be mentioned that these plateaus also appeared in measurements of WT and 2B, but not as frequent as in the measurements of VWF 2A. For the quantitative determination of differences between the mutations higher statistics would be necessary. As we believe that the plateaus are most likely caused by the VWF ripping off from the substrate and no additional direct information about the protein elasticity can be won we did not follow up these kind of measurements.

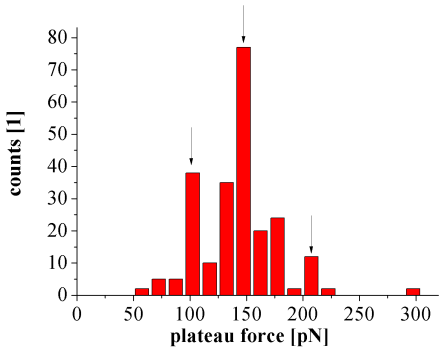

Figure 5.17.: The distribution of the plateau force F_p shows maxima at 100 pN, 160 pN and 200 pN.

As the most pronounced differences between WT and 2A measurements are shown and explained, we focus again on studying the initial hypothesis of correlation of mutations and differences in unfolding force. The fitting results of force curves of VWF 2A are shown in fig. 5.18.

The presented results were obtained from three different data sets (‘A9‘, ‘A11‘, ‘A13‘). In total, the structure of the results shows the typical shape as discussed in section 5.3.2. But systematic differences in the preparation (VWF concentration) and measurement (height range) correlate with the positions of the obtained results in the L_p-L_c-space. The resulting tuples from set ‘A9‘(triangles, presented before in [46]) most frequently are located in the L_c range of 30 nm to 300 nm with persistence lengths around 0.1 nm. The centroid of the data set ‘A13‘ is located in the same range of L_p but reaches contour lengths up to several microns. Rarely persistence lengths up to 100 nm appear. In contrast, the results of manually selected curves of the data set ‘A11‘(examples shown in fig. 5.14) give L_p in the range of 5 nm to 600 nm. At first glance these results seem contradicting, but the following paragraph will unravel this disorder. In a first step the differences between the data sets are named. Subsequently these information will be connected with the model assumptions illustrated before in 5.10.
The data sets ‘A9‘and ‘A11‘were prepared with similar VWF concentrations but differ in the recorded range of the height of the cantilever tip above the substrate. In turn, this range is the same for ‘A11‘and ‘A13‘, but the VWF concentration is increased significantly in the measurements of ‘A13‘, by linking the VWF to the substrate and not to the tip.

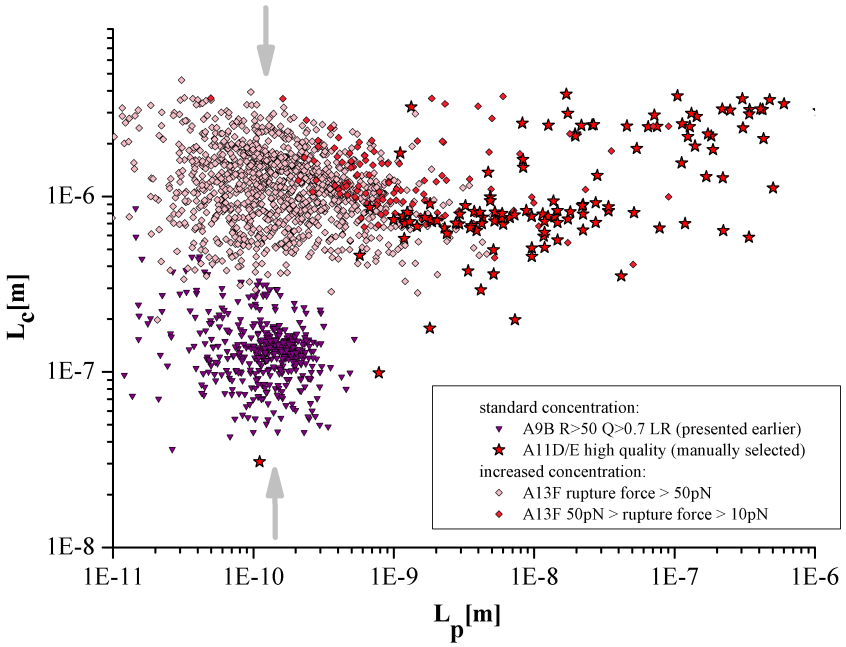

Figure 5.18.: Results of fits to force curves with VWF 2A. The gray arrows mark the typical persistence lengths of fits to the force regime above 50 pN. This regime dominates at low selected heights (purple triangles) or at high VWF concentrations even at high heights (rhombs). Manually selected fits with high quality to force curves in the low force regime, like shown in fig. 5.12, deliver L_p values up to 600 nm (red stars).

Thus, in the long range measurements with low VWF concentration (compare fig. 5.14) it is shown convincingly, that the persistence length of VWF 2A is roughly 300 nm. In agreement with the simulations, by the pulling of parallel strings also lower values are obtained in these measurements. In turn, evaluating the initial parts of these curves with rupture forces above 50 pN delivers L_p values around 0.1 nm.

Furthermore for VWF WT we showed already in fig. 5.5 that a real baseline and low force pulling of a protein can be hard to distinguish. Thus, the simple reason of choosing a too narrow height range could explain the values of L_p around 0.1 nm. Because of the low maximal height in the data set ‘A9‘ in most curves the internal friction was dominating the stretching process and the second regime is never reached. In fig. 5.19 one of the few exceptions is shown. Persistence lengths of 18 nm and higher are achieved. Along the same line, due to the higher VWF concentration the height range of the internal friction regime is extended in the measurements of the set ‘A13‘.

Only in the minority of the force curves, ruptures in the low force range below 50 pN are obtained (red rhombi in fig. 5.18). If these curves in the low force range appear, the fit delivers L_p also in the range of 100 nm. With fits to sections of force curves with ruptures above 50 pN similar values of L_p below 1 nm are measured (light red rhombi in fig. 5.18).

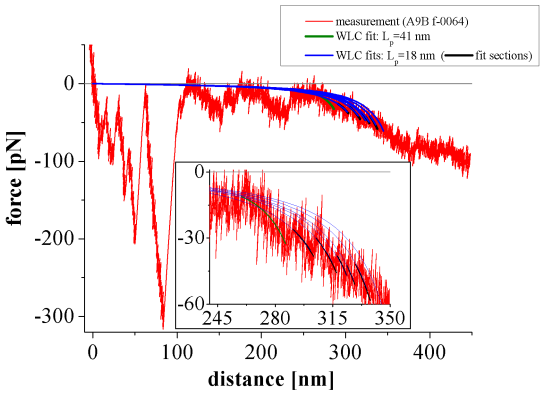

Figure 5.19.: Only four force distance curves, out of 2500, of the data set 'A9B'show rupture events beyond 200 nm. Because of an artifact these curves could not be evaluated automatically. Manually WLC fits with L_p of roughly 20nm can be fitted to the data.

In conclusion the origin of the seeming broad distribution of L_p for VWF 2A goes back to two different regimes, where VWF-VWF interaction, or VWF-water interaction respectively, dominates the energy landscape. By variation of VWF concentration the borderline between these regimes changes. For comparison between VWF WT and the mutations the values of the low force regime (here data of 'A11', red stars in fig. 5.18) are better suitable due to the lower complexity of the system. On the other hand, in vivo the other regime may be more appropriate.

5.3.4. Results & Discussion - Force curves of mutated VWF 2B

In fig. 5.20 exemplarily force distance curves of VWF 2B are shown. The gray lines below the x-axis show measurements with a cantilever, prepared with the 10-fold VWF concentration compared to the preparation for the black curves plotted above the x-axis. Obviously the same effect as in the WT and 2A measurements appears: while at low concentration already between 100 nm and 150 nm WLC-shaped force curves indicate single molecule pulling, this is not the case at high concentration. The appearing rupture forces are increased systematically. This is also reflected in the results of the high quality fits to these measurements shown in 5.21.

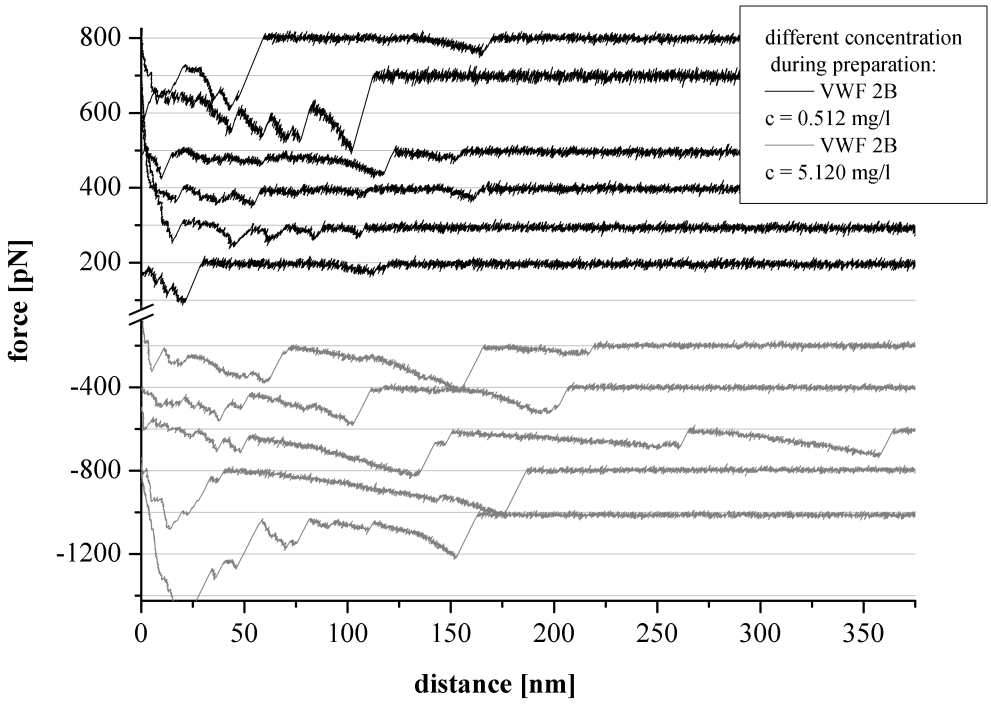

Figure 5.20.: A selection of force curves of VWF 2B. Curves below the x-axis are results of a preparation with 10-fold increased VWF concentration. The scales differs above and below the x-axis and baselines are shifted for clarity. The low concentration curves show significant lower forces and single molecule character.

The L_p values for the high concentration mainly lie in the range of 0.1 nm to 1 nm. In contrast, the values of the low concentration measurements are one order of magnitude higher. Surprisingly in these measurements no rupture events at higher ranges were detected. The lack of force curves of higher multimers is supposed to go back to degradation of the protein before or during preparation. Recalling the results of the simulations in section 5.3.2 the low persistence lengths could also be an artifact due to the lack of force curves of long polymers. Comparing the results of the simulations with the results of VWF 2B measurements no obvious correlation is visible. Nevertheless the significance of the 2A and WT data is for sure higher. Further measurements with VWF 2B samples, after determination of multimerisation with gel electrophoresis would consolidate the data.

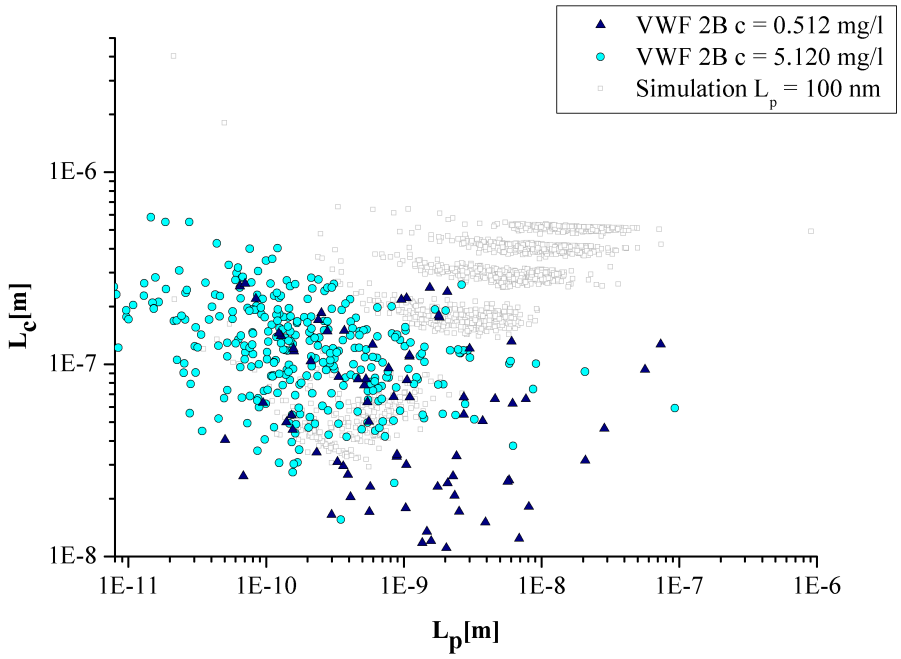

Figure 5.21.: Results of fits to force curves of VWF 2B. For clarity only high quality fits are shown. The triangles/circles are the results of the low/high concentration measurements, shown in fig. 5.20. Similar as shown for VWF 2A, the low concentration measurements show significantly higher persistence lengths. For comparison the simulation results from above are plotted in gray.

Summing up the measurements of VWF 2B, the measurements show typical WLC shaped force curves, with persistence lengths mainly between 0.1 nm and 10 nm. Contour lengths higher than 500 nm were not detected. Nevertheless, the two different regimes in the force curves, as explained more in detail for VWF WT and 2A, appeared. The significance of the 2B data is lower compared to the WT and 2A measurements.

5.3.5. Discussion - Comparison of WT and mutation specific differences and similarities

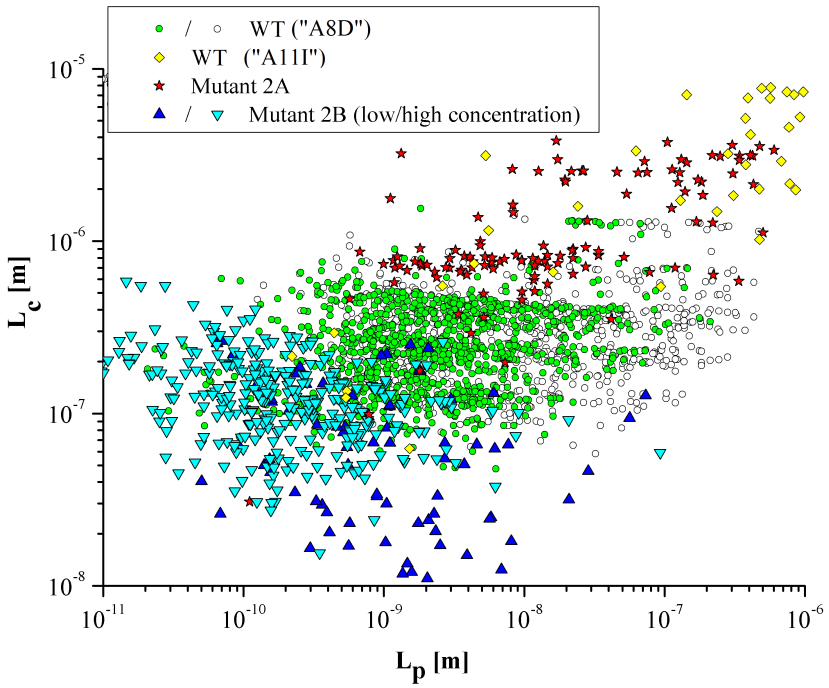

Figure 5.22.: The fit results of WT, 2A and 2B are wide spread in the L_p-L_c-space. The persistence lengths of WT and 2A reaches almost up to 1 μm. Whereas L_p of 2B reaches values below 100 nm. The threshold for the rupture forces are chosen to ensure significance due to sufficient deviation from the noise level.

As shown before, there are effects indicating two different force regimes. Through all measurements the persistence lengths of the "intermolecular friction" or "gel-like" regime is very similar for the WT and both mutations. With increasing VWF concentration this regime appears even up to L_c values of two microns.
Which regime, the latter or the "intermolecular friction" regime, applies to physiology stays unclear. But as in the "intermolecular friction" regime no differences between the mutations and wild type appear, the explicit comparison between the different VWF types is only shown for the force curves in the low force or "intra-molecular friction" regime in fig. 5.22. As the regimes in the data of VWF 2B cannot be separated as clearly as for the other types, here all good fits are taken into fig. 5.22 (blue triangles). The WT measurements shown in the according section above are plotted as open circles. To ensure significance, the higher quality fits with rupture forces of 20 pN and higher are colored green. Additionally the results of selected WT curves with

ruptures at very high distances are depicted as yellow rhombi. Secondly, the high quality fit results (A11D/E) of mutant 2A are taken from fig. 5.18.
The figure shows a wide spread of the contour lengths of the stretched protein fractions in the different measurements between 20 nm and 8 μm. For WT and 2A a broad range is covered, whereas for VWF 2B only ruptures up to the lengths of four dimers were detected. In principle this should not be problematic, as the persistence lengths is independent from the contour lengths. But as the comparison with the simulation showed convincingly, the correct determination of the persistence lengths of such a polymer is challenging. As described before, due to several reasons the results in the L_p-L_c-space spread over a broad range in L_p even if only the best fits are taken into account. A mean value of L_p is not significant as it depends on the number of parallel stretched fibers and the concentration of VWF. In contrast, the highest appearing values of L_p, where accumulations appear, are a better estimation for the intrinsic parameter L_p of the basic building blocks of the polymer. This is problematic if the intrinsic property L_p has to be determined. Furthermore with increasing length of the stretched section of the polymer the upper limit of detectable L_p increases.
These upper limits are roughly 400 nm for VWF 2A, 700 nm for WT and 60 nm for VWF 2B. Critically treated these numbers are only estimations, as the measuring system and the interpretation of the data is quite complex as shown in this chapter. The persistence lengths of the WT and 2A measurements partly overlap for $L_c \approx 3.5 \mu m$. There the differences are not significant. Furthermore single force curves of different VWF types cannot be distinguished reliably. Thus, the result of this comparison is the fact, that there are differences between the mutation 2B and the other both studied VWF types. In several attempts no fit tuples of 2B in this range were obtained, but differences in the according VWF samples per se cannot be excluded as mentioned above. Further attempts to determine differences in the persistence lengths of different polymers should consider the following conditions: 1.the contour lengths of the used polymers have to be determined and adapted/selected prior to force spectroscopy (e.g. by gel electrophoresis), 2. the concentrations have to be minimized to ensure measurements of the "intramolecular friction"regime.

5.4. Conclusion - Correlation between elasticity and clinical dysfunction

To sum up, the detailed study of mechanical stretching of VWF showed similarities and differences between WT and mutations 2A and 2B. In the "intermolecular friction"or gel-like regime the forces are similar for the different

VWF types. In the other regime, as far as the results can be compared due to their differences in measured contour lengths, 2A and WT show maximal persistence lengths between 100 nm and 1μm, whereas the maximal measured persistence lengths for 2B are below 100 nm.
The initial hypothesis assumed that the differences in agglutination is caused by the fact, that mutation 2A needs higher stretching forces than WT and the other way round for 2B. Based on the measured persistence lengths this does not hold. Anyway, precise conclusions to the biological function of the different VWF types would be hard to defend.
But as in the majority of the measurements there were hints that the intrinsic persistence lengths of 2A are higher than the one of WT and vice versa for 2B at this point some predictions are given.
If in future the forces of the conformation change of the different mutations can be determined more precisely and will be confirmed to show the order as named above, the results are in agreement with an adapted version of Ruggeris hypothesis concerning the agglutination behavior and its consequences for hemostasis [38], as illustrated in figure 5.23. As mentioned in the introduction it was believed that the lack of HMWM goes back to the inability to form large multimers in VWD type 2A, respectively to the removal of HMWM in VWD type 2B due to higher binding affinity to platelets and tissue.

In 1987 it was shown that the largest multimers of VWF 2A are degraded easier [49]. Our measurements indicate, that the persistence length of VWF 2A could be higher than the one of the WT. As a consequence the unfolding forces are lower. In turn, the probability that the polymer is in the unrolled conformation during normal blood flow is increased compared to the WT. Furthermore it was demonstrated in 2009 with optical tweezers that the cleavage of VWF is increased significantly, if the A2 domain is unfolded. Combined with the lower unfolding/stretching forces of VWF 2A this can explain the lack of HMWM: due to the lower unfolding forces the probability for cleavage is higher, leading to a lower equilibrium size of multimerisation.
On the other hand there is the correlation of VWF 2B and thrombocytopenia (TTP), a decrease of platelets in blood [50, 51]. In 1989 it was shown, that high multimers of VWF 2B possess a higher binding affinity to platelets leading to the hypothesis of removal of the HMWM from the blood circulation [52]. Furthermore Hultin et al. related in 1990 TTP with VWF 2B [53] by the postulation, that stress induced VWF 2B release can lead to spontaneous platelet aggregation because of the presence of HMWM. In turn, our findings, that the necessary forces to unfold VWF 2B are higher compared to WT, support this postulation. Along the same line, as for VWF 2A, the equilibrium size of multimerisation is increased due to the higher unfolding force of VWF 2B. A release of large amounts of HMWM in patients suffering from VWD 2B then is more problematic as in healthy patients, as the degradation prob-

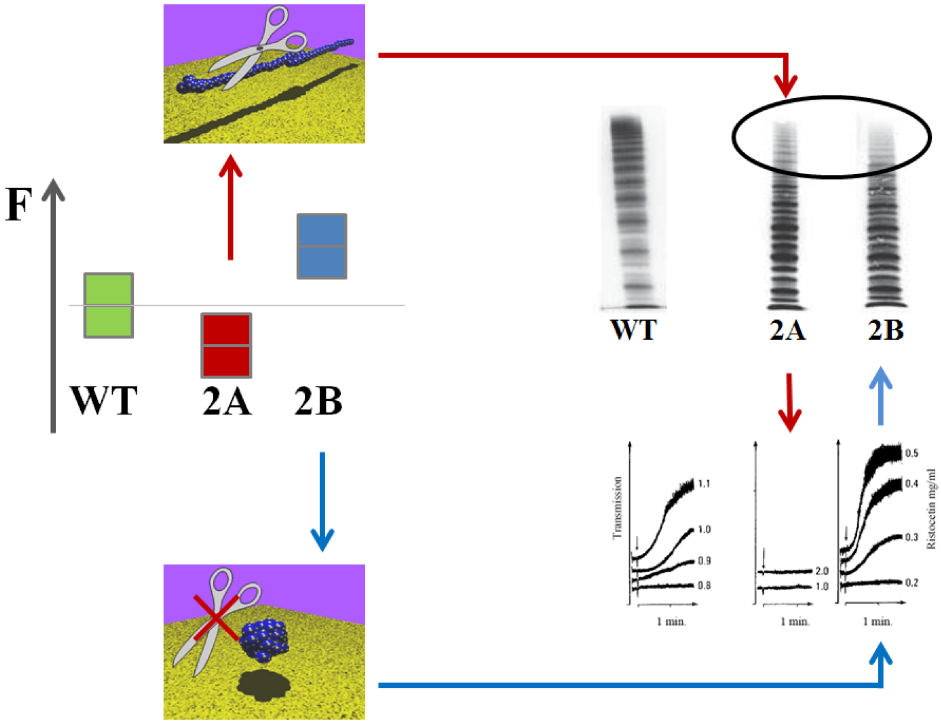

Figure 5.23.: The measurements support the hypothesis concerning the paradox of VWD type 2, where the mutations 2A and 2B lead to the same bleeding dysfunction, while the mutations show opposite effects in agglutination. The arrows indicate for both mutations the cause and effect chain within the hypothesis.

ability may be decreased.
In summary, the measured differences in unfolding forces of WT and the mutation 2A and 2B disprove the original hypothesis but are not in contradiction to the above explained hypothesis concerning the paradox of VWD type 2 [54], where the mutations 2A and 2B lead to the same bleeding dysfunction, while the mutations show opposite effects in agglutination.

5.5. Outlook - Force and height clamp measurements give insight in conformation changes

The discussions above show that eventually the persistence length of VWF is not the best suited measure to predict the conformation change behavior precisely. Maybe changes in degree of multimerisation or hardly controlable

effects during the preparation process could lead to a enhanced appearance of the gel-like regime compared to WT. Thus, mostly small persistence lengths would be obtained. The simulations using a Boltzmann-ansatz offer another possible approach to detect differences in the conformation change from native to elongated state.

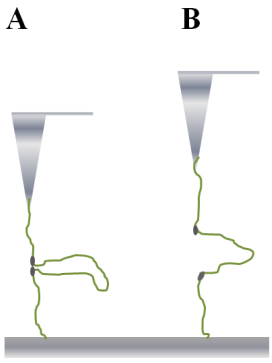

Figure 5.24.: Domain unfolding

The elongation of a folded protein can be described with the transition rates of folded to unfolded state for each building block (domain). Fig. 5.24 illustrates the transition of one building block from the folded state A to the unfolded state B by breaking of non covalent bonds within the (partly) coiled polymer. Even if protein folding is assumed to be based on global interactions like hydrophobicity [55] it is reasonable that some bonds are more sensitive to small local mutations than the global property persistence length. In the following paragraph the basic ideas of experiments are given, which can help to answer the all-embracing question about the correlation of clinical symptoms and unfolding processes. The preparations for these experiments could follow the same protocol, which can be found in the appendix. The argumentation concerning the probabilities of the native and the unrolled state and the consequences on the regulation of multimer size could be directly transfered to the interpretation of such experiments.

The potential H of a polymer stretched with an force sensor obviously has at least two contributions like indicated in fig. 5.25: on the one hand the force sensor itself has a potential proportional to the square of the displacement from its rest position x_0 (blue dashed line). On the other hand the elongation of a polymer is typically diverging when the elongation reaches the contour length (WLC potential, gray dotted line). The combination (red solid line) of both contributions lead to an equilibrium position M. But the knowledge about at least two different stable conformations of VWF [2] depending on the applied force already leads to the conclusion that this simple description is not sufficient, because of the lack of a second potential minimum. Here Kramers theory about Brownian motion over potential barriers [56, 57] and its application to protein folding [58] is helpful.

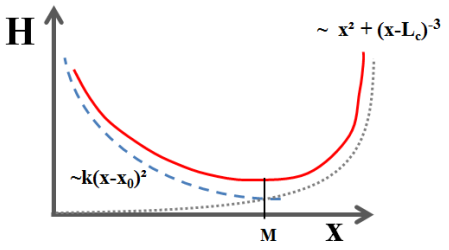

Figure 5.25.: Potential H as function of elongation x of a protein under stress as result of the two contributions force sensor (dashed) and protein (WLC potential, dotted).

If two potential minima are separated by a potential barrier the barrier height $\Delta G := \Delta G_1 - \Delta G_2$ and the transitions rates are correlated following equation 5.7.

$$k_i = k_0 e^{\frac{-\Delta G_i}{k_B T}} \tag{5.7}$$

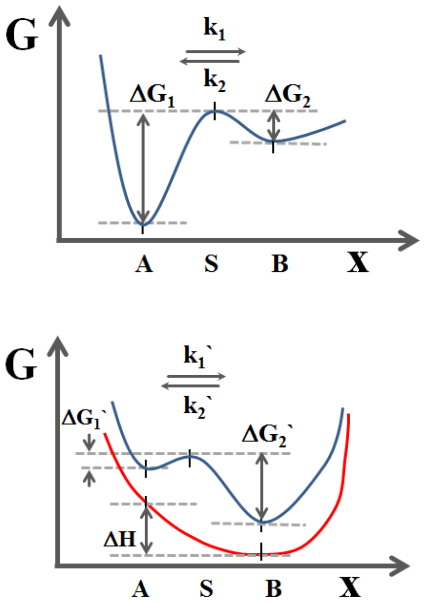

Figure 5.26.: top: Kramers theory: two states A and B are separated by a potential barrier with the instable transition state S. The x-axis reflects the reaction coordinate. The rates k_i follow eq.5.7. **bottom:** Resulting potential if the potential barrier is added to the energy landscape of a polymer stretched with a force sensor. The barrier heights are altered and influence the ratio of the transition rates like shown in eq.5.7.

In fig. 5.26 two potential minima A and B are separated by a barrier that represents an energetically unfavorable transition state S along the reaction path. The x-axis reflects the reaction coordinate, i.e. the position along this reaction path in the according phase space.Thus, if we imagine the case of a single domain in a free protein, the ratio of unfolding to folding $r := \frac{k_1}{k_2} = e^{-\frac{\Delta G_1 - \Delta G_2}{k_B T}}$. For a simplified picture one can identify the reaction coordinate with the elongation of the protein and the barrier height with the necessary energy to break the bonds like indicated in fig. 5.24.

If now a force is applied to the protein containing one closed domain or loop the according potential barrier has to be added to the potential H illustrated in fig. 5.25. Here we consider the length as thermodynamic variable. For a single chemical bond the barrier width is much more narrow compared to the length of a protein; in literature estimations for the critical distances to break such bonds are reported to be below 1 nm [55].The resulting energy landscape G is plotted in fig. 5.26.
The ratio $r`$ of the transition rates then is:

$$r` = \frac{k_1`}{k_2`} = e^{-\frac{\Delta G_1` - \Delta G_2`}{k_B T}} = e^{-\frac{\Delta G_1 - \Delta G_2 + \Delta H}{k_B T}} = r e^{-\frac{\Delta H}{k_B T}} \tag{5.8}$$

where $\Delta H = H(A) - H(B)$. Because of the flat increase of the entropic contribution (compare WLC model) in this part of the potential, the main contribution to ΔH is caused by the potential of the force sensor, e.g. the cantilever. This means $r`$ gets arbitrarily big with increasing ΔH, respectively with higher applied forces. This is for example observable in force clamp measurements, where only at very low forces domain unfolding and folding

appears. In contrast, at higher applied forces only domain unfolding appears. In the appendix A.3 for VWF WT examplarily measurements are shown and possible continuative experiments are suggested. Such force clamp measurements allow to vary ΔH and theoretically to determine the intrinsic barrier height ∂G by the evaluation of the ratio r [48]. The weak point of force clamp measurements, besides the well known baseline drift problem, is the fact, that by regulation of the applied force, energy is given to / taken from the system and it is challenging to distinguish the real effects from technical artifacts.
Simpler and well controlable measurements are height clamp measurements. A certain distance between the cantilever chip and the substrate, called the height, is clamped and the fluctuations of the length of the protein are observed as function of time and force. These fluctuations cause a deflection of the cantilever tip and in turn the change in applied force effects the fluctuations again. As the exact length and applied force for every data point is known, one can determine very precisely the ratio r for different forces by clamping of different heights without further intervention. During the experiments the system is observed under equilibrium conditions, while it fluctuates between the possible states. These experiments are less established as the well know force spectroscopy, but seem to be a promising way to study the crucial conformation change of VWF, also in the light of molecular mutations correlated with bleeding malfunctions.

6. Conformation of VWF switches interaction with phospholipid membranes

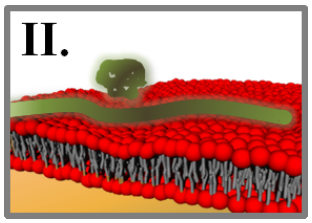

In the initial step in primary hemostasis the essential protein in the blood clotting process, von Willebrand Factor (VWF), adheres at the vessel walls. Furthermore after stimulation of the endothelial cells, significant amounts of VWF are released. Stretching of this globular VWF multimers is the essential step in hemostasis before platelets can bind. This leads to the question about the interaction between VWF and the cell membrane depending on the phase state of protein and membrane. As the elasticity parameters of a lipid bilayer (bending modulus) and monolayer (isothermal lateral compressibility) are connected, we use Langmuir film balance experiments to study the influence of globular VWF on phosphatidylcholin monolayers as a simple model system for biological membranes. The isothermal lateral compressibility of DPPC monolayers is studied as a function of VWF concentration and temperature for wild type VWF and mutations of the type 2A and 2B. Comparing the measurements with calculations of an ideal superposition of the lipid monolayer and a VWF layer at the surface, we distinguish additional effects from those, explained with an interaction free model of the compression of both substances. Furthermore the results are compared with the interaction of VWF and lipid vesicles after stretching the protein with surface acoustic waves. After physical activation of VWF, the membrane heat capacity profile as well as the secondary structure of VWF is altered significantly. We conclude that significant stronger interaction between protein and membrane appears when VWF is in the activated state compared to the globular conformation. Transferring these results into physiology one can suppose that processes in nature take advantage of this dependence of interaction of VWF and membranes, as high interaction is solely requested at locations with injuries of the blood system and not during normal circulation in the blood.

6.1. Introduction

The major player in primary hemostasis is von Willebrand factor (VWF). One of its main functions is to bind blood platelets to injuries in the vascular system to start wound healing [59]. This mechanism is defective at patients suffering on von Willebrand desease type 2, where a mutation in the structure of the protein is correlated with changes in the blood clotting behavior [60]. Furthermore VWF is released after various kinds of stimulation of human cells [61, 2, 21]. As the thermodynamic properties of membranes are sensitive to molecules, changes in ionic strength or pH [10], there is obviously the question about the interaction of VWF and the cell membrane. Langmuir monolayer experiments are a well-established way to control the state of a lipid system with a low preparation effort and high reproducibility. It has been shown that the isothermal compressibility κ_T^A and the bending modulus of a lipid bilayer κ_B are connected [62, 63]:

$$\kappa_B = \kappa_T^A 16/d^2 \tag{6.1}$$

where d is the thickness of the bilayer. This allows us to study the interaction of VWF and the relative simple and controllable lipid monolayer as a model system for the in vivo interaction of VWF and cell membranes. Therefore we analyse the thermodynamic properties of phoshpatidylcholin monolayers in the presence of VWF in the bulk water. Besides concentration and temperature, also the difference between wild type VWF and mutations of the type 2 were studied and compared with the simulation of a model that assumes no interaction.
It has already been explained how shear stress triggers adhesion of VWF fibres to endothelial cells via a conformation change from a coiled globular to an elongated conformation [2]. In turn, this leads to the question about the role of the protein conformation for the interaction with pure lipid membranes without e.g. special receptor mechanisms. To account for such dynamic measurements the changes in secondary structure of the protein after application of overcritical shear force in presence of lipid vesicles and the protein conformation dependent impact on the phase transition behaviour of lipid vesicles were studied [64]. Bringing those measurements together we reason the role of protein conformation for the interaction of VWF with artificial and natural lipid membranes.

6.2. Materials and Methods

6.2.1. Isothermal area compression/expansion measurements

All used lipids were purchased from Avanti Polar lipids solved in chloroform. If not explicitly mentioned 1,2-dipalmitoyl-sn-glycero-3-phosphocholine (DPPC) monolayers are studied at a bulk temperature of $20°C$ on phosphate buffer (pH 7, 130 mM NaCl). After spreading the lipids on a Langmuir through with a volume of 50 ml and a surface area of 100 cm^2, the systeme was equilibrated 15 minutes, mainly to wait for the evaporation of the chloroform. In all experiments first the pure DPPC monolayer was compressed and expanded at a speed of 16.6 cm^2/min to calibrate the isotherms afterwards. The pressure of the gas analogous phase was set to zero and the area per lipid molecule was set to $0.48nm^2$ at a lateral pressure of 30 mN/m. In the following step the pressure was monitored as a function of time during addition of VWF to the system in the liquid expanded phase from the top and it was waited, depending on the VWF concentration, until a saturation pressure was reached. Afterwards the monolayer was compressed and expanded again. For analysis only the first compression respective expansion was used, except in the experiments were temperature was varied at constant VWF concentration. Here for every concentration the isotherms at each temperature were measured with the same monolayer. To determine the compressibility with a macro in Origin8 the isotherms were extrapolated to the same number of data points, smoothed and the area per lipid molecule A was differentiated with respect to lateral pressure Π. In reference measurements we used a mixture of 98% DPPC and 2% 1,2-dioleoyl-sn-glycero-3-[(N-(5-amino-1-carboxypentyl)iminodiacetic acid)succinyl] (nickel salt) (18:1DGS-NTA(Ni)) to bind VWF with an His-tag to the monolayer. The used VWF was purchased from the Department of Paediatric Haematology and Oncology, University Hospital Hamburg, Germany. Four different types of VWF were used: the wild type VWF with and without a His-tag (WT, WTHis) and two mutations VWF R1308C (2B) and VWF G1629E (2A). The concentration of VWF for all samples was adjusted to 67 μg/ml before addition to the monolayer.

6.2.2. Calculated Isotherms

The simulated isotherms were calculated with the software SciLab, using the equations shown in the theory section. Besides three input variables (starting pressure Π_0 , lipid area $A_L(\Pi_0)$ and VWF area $A_{VWF}(\Pi_0)$) the compressibility $\kappa_{L/VWF}(\Pi)$ of both components were given. For simplification $\kappa_L(\Pi)$ was reduced to 71 data points (0.5 mN/m step width) and $\kappa_{VWF}(\Pi)$ to 25 data

points (0 mN/m - 23.5 mN/m, 23.5 mN/m). To get reasonable values for the compressibility of VWF, it was necessary to measure the compressibility in different pressure ranges by variation of VWF concentration. Especially for the expansion isotherms deviations between those compressibilities occur due to a rapid pressure decrease after start of area expansion which is only weak pressure dependent. Hence, in the overlapped pressure ranges values close to the compressibility of the isotherms of the higher pressure range were chosen for the simulations (see figure 6.4), as the measured DPPC-VWF-isotherms also range up to 35 mN/m.

6.3. Results and Discussion

6.3.1. Measured isotherms and compressibilities

Immediately after addition of VWF to the monolayer the pressure increases rapidly and reaches a saturation value within one to three minutes. This value is proportional to the amount of added VWF for small amounts of added VWF. Exemplarily in fig. 6.1a some isotherm compression and expansion cycles in presence of VWF are shown. Obviously there is a significant difference between compression and expansion curves: this hysteresis increases with increasing VWF amount and remains even if the barrier speed is reduced by a factor of ten.

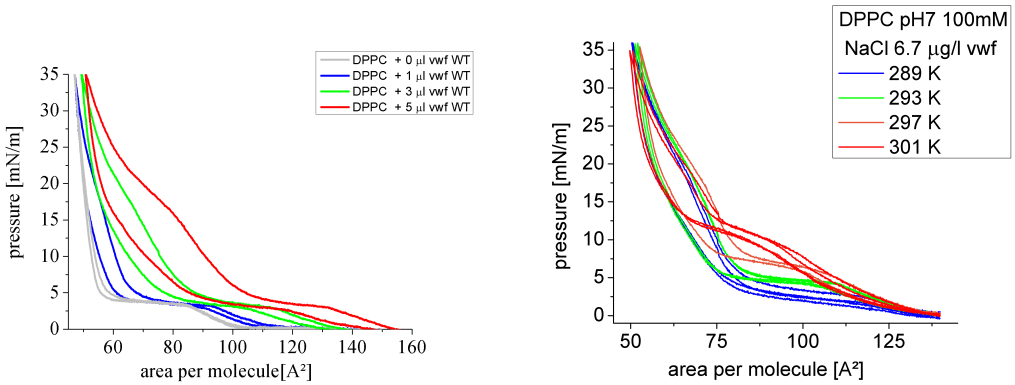

(a) DPPC Isotherms in presence of VWF

(b) Temperature dependent DPPC isotherms

Figure 6.1.: (a) DPPC isotherms at 20°C in presence of VWF shift to higher areas and show an increasing hysteresis with increasing VWF concentration.**(b)** DPPC isotherms for a fix VWF concentration at different temperatures. While the phase transition shifts to higher pressures with increasing temperature, the VWF associated effects do not shift.

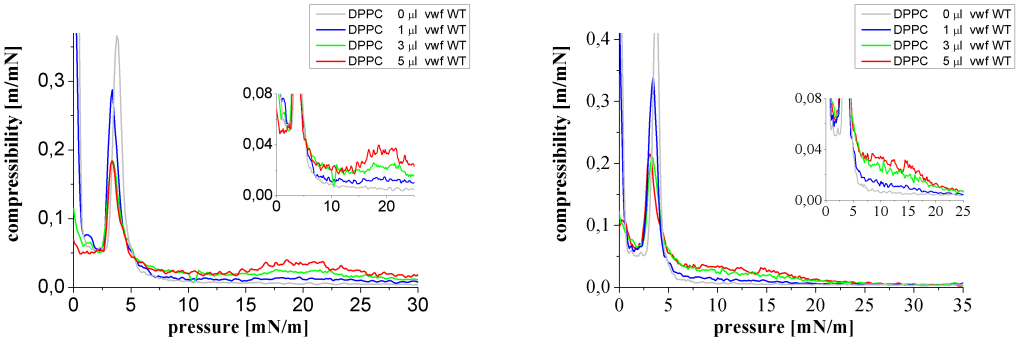

(a) Compression compressibility

(b) Expansion compressibility

Figure 6.2.: Compressibility as function of VWF concentration **(a)** compression **(b)** expansion. The maximal compressibility at the phase transition is decreased. An additional broad peak between 15 mN/m and 25 mN/m occurs for the compression curves. In the compressibility extracted from the expansion curves a shoulder occurs between 5 mN/m and 20 mN/m.

Besides the hysteresis the isotherms are shifted to higher areas but show the typical plateau around 5 mN/m like pure DPPC monolayers. Furthermore the width of the plateau is increased weakly compared to pure DPPC and in the liquid condensed phase an additional change in the slope appears that is untypical for DPPC. This effect is more pronounced in the compression curves. To study the changes more detailed in the discussion section the compressibilities of both, compression and expansion curves, are compared concentration dependent. The VWF induced increase of compressibility between 10 mN/m and 20 mN/m is nearly temperature independent as shown in fig. 6.1b. This figure shows isotherm cycles of the same monolayer for different temperatures and fixed VWF concentration. While the well-known phase transition plateau shifts towards higher pressures with increasing temperature, the VWF induced shoulder remains unchanged.

Because of the hysteresis in fig. 6.2 the compressibilities of the isotherms in fig. 6.1a are shown separately for compression and expansion. As well in compression isotherms, as in the expansion isotherms, the expected peak around 5 mN/m, originated from the phase transition of the lipid monolayer, is existent for all concentrations. The maximal compressibility is reduced. Furthermore, in the liquid condensed phase an additional broad peak (compression) respectively a shoulder (expansion) becomes more pronounced with increasing concentration. The different types of VWF show the same characteristics and differ solely in dependence of the effect on VWF concentration (compare fig. B.6). The strong change in $\kappa(\Pi)$ suggests the question in how far the binding of VWF to the lipid monolayer influences the phase transition from

liquid expanded to liquid condensed phase. In the following section some thermodynamic considerations try to answer this question.

6.3.2. Thermodynamic considerations concerning the impact of VWF binding on the phase transition behavior

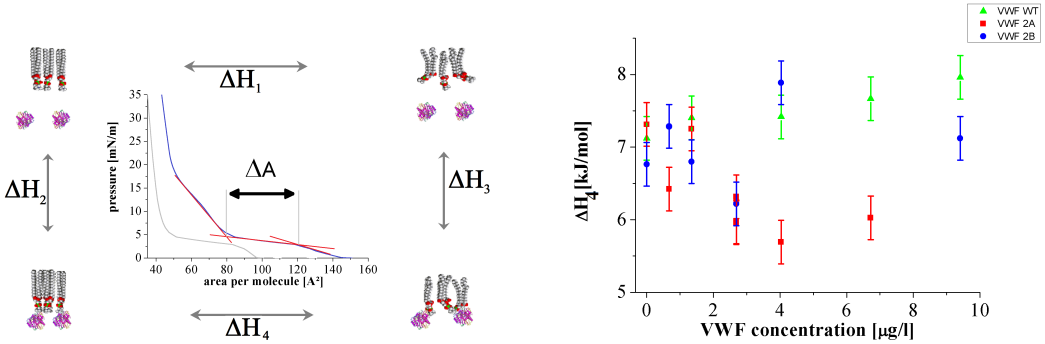

(a) Enthalpy as function of state

(b) Transition enthalpy ΔH_4

Figure 6.3.: (a) Enthalpy as function of state. In the two states in the upper part of the scheme the protein and the lipid monolayer are independent, whereas in the lower part they are bound to each other. In the two states on the left side the monolayer is in the liquid condensed phase, whereas in the two states on the right side the monolayer is in the liquid expanded phase. Bringing the system from one state to another does not depend on the way. **(b)** Resulting transition enthalpy ΔH_4 for different VWF types shows a weak concentration dependence.

In this section it is considered what information about the binding of proteins, here VWF, to lipid monolayers can be taken from the measured isotherms, especially from the plateau width ΔA. As the Helmholtz enthalpy H is a function of state it holds

$$\Delta H_1 + \Delta H_3 = \Delta H_2 + \Delta H_4 \tag{6.2}$$

where ΔH_i are the differences in H between the different states as depicted in figure 6.3a. The four states are defined by the criteria membrane state (liquid ordered, liquid expanded) and protein binding (protein bound to membrane, protein and membrane independent). Hence the enthalpy difference $\Delta H_3 - \Delta H_2$ equals the difference of the phase transition enthalpies $\Delta H_4 - \Delta H_1$. This difference can be extracted from the isotherms in presence and absence of the protein using equations 6.3 and 6.4:

$$\Delta H = T\Delta S + V\Delta P \overset{\Delta P=0}{=} T\Delta S \tag{6.3}$$

As shown before [65] in the vicinity of a critical point it holds:

$$\frac{\partial \pi}{\partial T} = constant \tag{6.4}$$

and hence for the phase transition pressure Π_{PT} and the excess area ΔA:

$$\Delta S = \Delta A \frac{\partial \Pi_{PT}}{\partial T} \tag{6.5}$$

The difference between the binding energy of VWF to the monolayer in the liquid disordered state and the binding energy in the liquid ordered state of the monolayer ΔE_B can be calculated from the measured parameters T, $\frac{\partial \Pi_{PT}}{\partial T}$ and ΔA:

$$\Delta E_B = \Delta H_3 - \Delta H_2 = \Delta H_4 - \Delta H_1 = T \frac{\partial \Pi_{PT}}{\partial T} (\Delta A_4 - \Delta A_1) \tag{6.6}$$

The plateau width of the transitions ΔA_i are measured by drawing tangents to the expansion isotherms as indicated with the red lines in the inset in fig. 6.3. Whereas the shift of the phase transition pressure with increasing temperature $\frac{\partial \Pi_{PT}}{\partial T}$ is taken from a linear fit over DPPC isotherms between $16°C$ and $28°C$ with VWF concentrations in the used range. For the calculation of ΔH_4 the resulting value $\frac{\partial \Pi_{PT}}{\partial T} = (0.8\ \mathrm{mN/m})/\mathrm{K}$ was used.
The results for ΔH_4 are plotted in 6.3b as function of the used VWF concentration. Thus ΔE_B can be calculated by subtraction of the enthalpy of the VWF free sample. Because of the weak concentration dependence compared to the error bars, the measurements are compared to an ideal superposition model (two-component-system) that assumes no interaction of protein and lipid in the following part. Furthermore, it would be very interesting, to compare this values with the difference of binding energies of VWF and phosphatydilcholine vesicles in different phases by isothermal titration calorimetry.

6.3.3. Ideal superposition does explain the main effects qualitatively

As mentioned above the following part compares measurements with an interaction free model. As a first step we show how to get isotherms out of the compressibility as function of pressure. Afterwards the calculation of the ideal superposition is explained and finally compared with the measurements, concentration dependent, for wildtype VWF and two mutations that are correlated with malfunctions in hemostasis. The isothermal lateral compressibility κ_T^A is defined as the derivative of the relative area per lipid molecule with respect to Π.

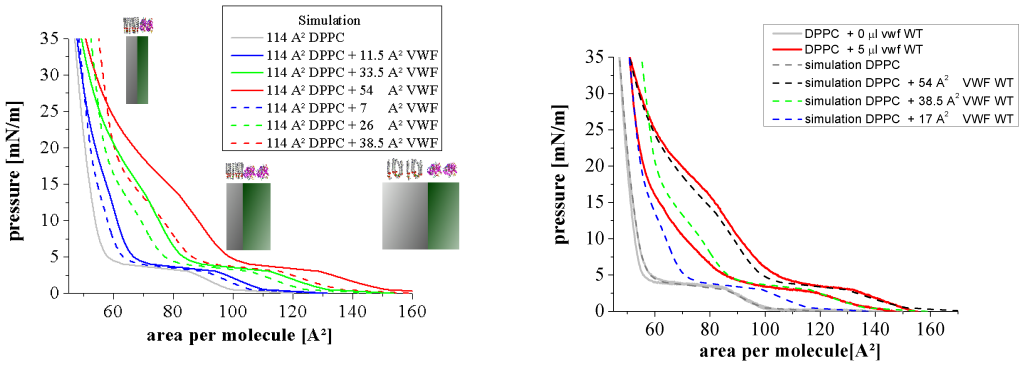

(a) Calculated Isotherms

(b) Comparison between Measurement and Calculation

Figure 6.4.: Calculation **(a)** Calculated compression/expansion isotherms. Inset: Model scheme of ideal superposition of lipid and protein layer. Independent elastic behavior of both components and equal lateral pressure in both layers is assumed. The gray area symbolizes a lipid monolayer, the green area a layer of VWF. **(b)** Comparison between calculated (dashed lines) and measured (solid lines) isotherms. The calculated compression isotherms fit well, whereas the expansion isotherms show deviations especially in the middle pressure range. This indicates a change of VWF partition coefficient between surface and bulk (see text).

$$\kappa := \kappa_T^A = -1/A \frac{\partial A}{\partial \Pi} \mid_T \tag{6.7}$$

$$\partial \Pi = -1/A \kappa \partial A \tag{6.8}$$

We now approximate the total differential with equation 6.8 and integrate $\partial\Pi$ from an initial pressure Π_i to a final pressure Π_f where κ is assumed constant:

$$\Pi\left(A_f\right) = \int_{\pi_i}^{\pi_f} d\pi + \Pi_i = \int_{\pi_i}^{\pi_f} -\frac{1}{A\kappa} dA + \Pi_i = -\frac{1}{\kappa} ln \frac{A}{A_i} + \Pi_i \tag{6.9}$$

where $A_{f/i}$ is the area per lipid molecule corresponding to the final/initial pressure $\Pi_{f/i}$. Thus, for pressure ranges where κ is constant the area per molecule can be expressed as a function of Π:

$$A_f\left(\Pi\right) = A_i e^{(-\kappa \Pi)} \tag{6.10}$$

Thus, from knowing $\kappa\left(\Pi\right)$ and the starting values (A_i , Π_i) we can calculate A(Π) using a continuity condition whenever κ changes. As the used VWF also shows surface activity, area compression and expansion isotherms can be recorded. In figure B.4 the compressibility of such a pure VWF layer is

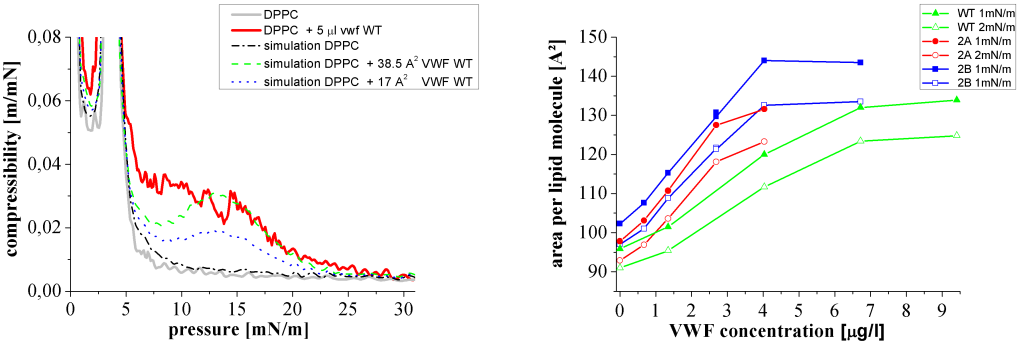

(a) Comparison Expansion compressibilities

(b) Saturation of area per molecule

Figure 6.5.: Differences between model and measurement **(a)** Compressibility of measured compression/expansion isotherms of DPPC before/after (gray/red line) addition of VWF are compared with the compressibility of simulated isotherms. The simulations (green dashed line) show a lower compressibility between 6 mN/m and 11 mN/m. A further decrease of VWF area in the model leads to a shape similar to the measured compressibility, but to too low values in the whole range between 6 mN/m and 30 mN/m. A pressure dependent VWF amount in the layer explains the measured effects. **(b)** Isobaric and isothermal area per lipid molecule as function of added amount of different types of VWF (WT, mutations 2A and 2B) taken from expansion isotherms. After a linear increase with concentration the area shows a saturation that occurs at different concentrations. This saturation limits the scope of the model.

plotted. Those isotherms feature a hysteresis comparable to the one seen in DPPC isotherms in presence of VWF. Assuming now two independent, i.e. non interacting, surface layers and equal lateral pressure in both layers we calculate the change in area for increasing the pressure for a finite step using those compressibilities and eq.6.10 (see fig. 6.4a: gray area lipid, green area VWF). So from a starting triple (lipid area, VWF area, initial pressure) by increasing the pressure in small steps (here $\Delta\Pi = 1\mu$N/m) a complete area compression isotherm is calculated using the measured compressibilities of the pure components. A short explanation for the observed isotherms, as illustrated in the inset in fig. 6.4 is the following: around 5 mN/m the lipid area is compressed much stronger than the VWF area due to the higher compressibility. Vice versa the VWF area is compressed stronger around 18 mN/m. These pressure ranges, where the materials show a transition, or, more general, are maximal compressible, cause the characteristic plateaus/shoulders in the area isotherms.

Calculated compression/expansion isotherms with systematic increased size of VWF fraction of the layer are shown in figure 6.4a. The isotherms look quite alike the measured isotherms (compare fig. 6.1a). Using the same software

macro as for the measured isotherms, the compressibility of each simulated isotherm is calculated (see figure B.5). The characteristic decrease of maximal compressibility around 5 mN/m is reproduced, as well as the broad peak between 10 mN/m and 20 mN/m, which becomes more pronounced with increasing VWF concentration.
An addition of the compressibility profiles of both components scaled according to the ratio of the initial areas delivers a similar result (not shown). So, one can already presume an mostly independent compression of both layers, indicating a weak, or more precise, with this technique hardly measureable, interaction of phosphatydylcholine and VWF in its globular conformation. At this point it has to be mentioned that the interpretation of the results may turned out totally different without the simulation of the ideal superposition. Future studies to monolayer elasticity should take care of similar possibilities of misinterpretation. In the following section the differences between calculation and measurements are discussed in detail.

6.3.4. Differences between measurements and ideal superposition

The limits of the congruence of measurements and calculations are the following. While the calculated and measured compression isotherms look quite similar on the first view, the expansion isotherms in the calculations are obviously different from the measured ones. The calculation of the expansion isotherms overlay in the pressure range between 0mN/m and 6mN/m quite well with the according compression isotherms, if in the expansions a smaller amount of VWF is assumed (compare figure 6.4b). At high pressures (18 mN/m - 35 mN/m) the measured isotherms are reproduced by the simulation much better with an even smaller VWF area. As can be seen in the compressibility of measurements and calculation in figure 6.5a the simulation that fits the isotherm in the low pressure range, reproduces $\kappa(\Pi)$ quite well, besides in the range between 6 mN/m and 11 mN/m. Whereas $\kappa(\Pi)$ in the simulation, that fits the upper pressure range, reproduces the shape but not the absolute values. Thus one can conclude that the pressure dependent partition coefficient between interface and bulk is changed in the above mentioned pressure range. Hence, during expansion more VWF from the bulk attaches to the interface in the presence of lipids. This fits to the observed effect, that the broad compressibility peak in the liquid compressed phase of the system is shifted to higher pressures in the measurements compared to the calculation. This can be explained by an increased partition coefficient of VWF at the surface and VWF in the bulk, in the presence of a lipid monolayer at the water-air interface. Hence the pressure, where VWF is "pressed" into the bulk, is higher.
Possible sources of error for these considerations are the hysteresis and the in-

creased uncertainty in the determination of the compressibility of pure VWF layers compared to lipid monolayers. As the hysteresis could not be avoided by reducing the barrier speed by a factor of ten, the aforementioned barrier speed was chosen to avoid aging effects of the lipid monolayer.
Another difference between calculation and measurement is the prediction of a linear increase with concentration of the VWF induced effects. For high VWF concentrations the measurements show a saturation of the effects. For the increased area per lipid molecule this is depicted in figure 6.5b for WT, 2A and 2B for the liquid expanded phase. Exemplarily at addition of WT to the monolayer, the isobaric area per lipid molecule as function of VWF concentration increases linearly below 6.7 μg/l VWF. For higher concentrations a saturation value is reached. The critical WT concentration 6.7 μg/l corresponds to a ratio of 20 000 lipids per VWF dimer subunit. Quantification of the maximal hysteresis between compression and expansion shows also saturation behavior after a linear increase (shown in the appendix in fig. B.2). For 2A and 2B the saturation occurs already at lower concentrations but at a similar maximal area per lipid molecule. A quantitative comparison of this saturation effect between wildtype and mutations is not done, as no information concerning the degree of multimerisation of the different types of VWF is available. A further saturation effect not predicted is that the local maximum in lateral compressibility of $\kappa_{max} \approx 0.04$ between 10 mN/m and 20 mN/m is not exceeded at higher VWF concentrations than shown in figure 6.2.
Besides the saturation effects, a closer look to the compressibility for different types of VWF, indicates a small shift of the phase transition pressure dependent on VWF type. Careful control measurements confirmed that these shifts are artefacts due to pressure calibration or rather a decrease in surface tension due to the surface activity of the VWF molecules. However the decreased κ_{max} is in accordance with the simulation. Also the tendency that every addition of VWF leads to a decrease of κ_{max} and in the limits of low and high VWF concentrations the predicted order is received in almost all measurements. For the concentrations in-between the effect of contamination or oxidation of the lipids competes against the intrinsic properties of the lipid-protein-system. Thus, a firm statement on these effects especially on cooperativity in the phase transition needs further studies.
In summary, the main difference between non interacting superposition and the measurements is the change in partition coefficient of VWF between surface and bulk. Furthermore the saturation behavior of the VWF related effects is not predicted by calculation but is of course correlated with the change in partition coefficient. This effect has to be compared with the interaction of lipid interfaces and VWF in its elongated conformation.

6.3.5. Elongated VWF interacts stronger with phospholipid membranes

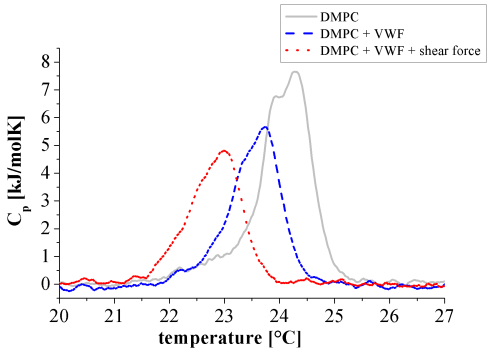

Figure 6.6.: Heat Capacity of DMPC SUVs in absence (gray solid line), presence of multimeric VWF (blue dashed line) and in presence of multimeric VWF after application of overcritical shear stress (red dotted line). VWF shifts the melting temperature of the lipids significantly and dependent on VWF conformation: $0.6°C$ globular conformation / $1.5°C$ elongated conformation.

As shown earlier [2] VWF changes from a globular to a stretched string like conformation (activated state) reversibly, if a critical shear rate is applied. To measure the interaction between activated VWF and lipids, dynamic measurements are necessary. As this is not possible with lipid monolayers, the interaction of VWF with phospholipid vesicles is studied. Differential Scanning Calorimetry (DSC) was used to measure the influence of VWF on the lipids, as the heat capacity profile of lipids is very sensitive to minute changes in lipid structure due to pH changes, solvents et cetera. To have a look on the impact of the presence of the lipid membranes on the protein, changes in the secondary structure of VWF can be measured with Circular Dichroism Spectroscopy (CD). In figure 6.6 (data from [64]) the heat capacity profile of DMPC vesicles is shown before and after addition of multimeric VWF, as well as after application of overcritical shear stress with surface acoustic waves (SAW). While the simple addition of VWF causes a shift in phase transition temperature of $0.6°C$ the phase transition temperature is shifted more than $1.5°C$ if the VWF is stretched in presence of the vesicles, suggesting that VWF in the elongated conformation binds significantly stronger to the lipid bilayers than in the coiled conformation. In control experiments protein free samples showed no changes in heat capacity upon treatment with shear force (data not shown).
Furthermore in [64] the author also studied the interaction of VWF and lipid membranes optically with bilayers prepared on a solid glass support. After addition of VWF molecules at blood concentration and after several hours equilibration time, overcritical shear stress was applied. After removing un-

bound VWF network-like structures, strongly connected to the membrane, could be shown. In clear contrast, network formation of VWF molecules was not observed without the application of shear flow.

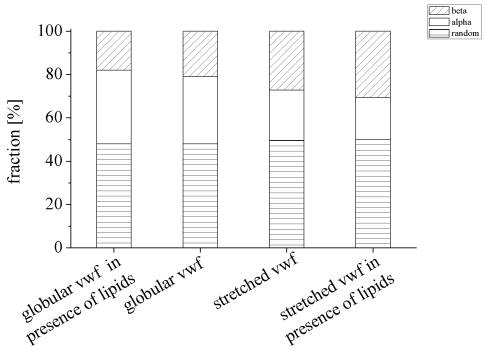

Figure 6.7.: Secondary Structure of dimeric VWF in absence and presence of DMPC vesicles and before and after application of overcritical shear stress. Shear stress leads to an increase of the fraction of beta sheets on cost of alpha helices. In presence of lipid vesicles this effect is increased.

To test the impact of the lipids on the secondary structure of VWF, lipid vesicles in presence of VWF in each conformation were studied with Circular Dichroism Spectroscopy (CD). Here also the interaction of lipids and VWF is stronger, if VWF is in the elongated conformation. In figure 6.7 the results of CD spectra of globular and stretched VWF in absence and presence of DMPC small unilamellar vesicles (SUV) taken from [64] are shown. After elongation of the protein by application of shear force the fraction of β-sheets is increased at the cost of α-helices, while the random coiled parts of the protein remained fairly unaffected. Interestingly this process is even increased in the presence of lipid vesicles while the bare presence of SUV without application of shear force shows the opposite effect. Steppich suggests a model where the α-helices are embedded in the membrane and thus, the shear flow is able to cause enhanced transformation of α-helices into more stable β-sheets [64]. One could imagine that these opposite behavior in vicinity of lipid membranes in nature stabilizes the elongated respectively the coiled conformation, depending if shear forces appear or not.

6.4. Conclusion and Outlook

In summary, the comparison between the interaction of globular VWF with phospholipid monolayers and the results from [64] suggests that the physical state of the protein plays the leading role in interaction between VWF and

membrane. In the presence of high amounts of globular VWF the elastic properties of lipid monolayers remain largely unchanged, as the comparison between measurements and calculations indicates. Furthermore the calorimetric data show a a much more pronounced change of the thermodynamic properties of a lipid bilayer in presence of elongated compared to globular VWF. Besides the membrane properties also the secondary structure of VWF is altered in presence of lipid interfaces. In turn, the stretched conformation is influenced stronger by lipid bilayers than the globular one.
Organisms in nature can eventually benefit from the switch between weak and strong interaction of VWF and lipid membranes depending on the protein conformation: under normal physical circumstances the globular protein in blood flow should not, or just weakly, interact with the endothelial cell membranes, whereas at locations of vascular damage, where high shear rates appear, the protein unfolds [2] and interacts with its environment in general, and the lipid membranes in particular.
One way to alter the state of VWF without applying high shear rates is the systematic change of pH to induce denaturation. Experiments could for example study the change in isotherms of DPPC in presence of a fixed VWF concentration, for decreasing pH. If VWF unfolds due to protonation, one would expect that this also happens at the surface and hence, interaction could be analyzed analog as presented here. Furthermore, it would be interesting to test the influence of elongated and globular VWF on the elasticity of vesicles in micropipette experiments similar to the experiments reported by Rawicz and Evans [66]. Elongating VWF by shear force in presence of GUVs, we predict from our calorimetric and monolayer data that the membrane elasticity is reduced in presence of elongated VWF stronger than in presence of globular VWF. For such experiments similar considerations like presented in our ideal superposition model have to be taken into account.
The present study shows that on the other side also the state of the membrane is important for the attachment of VWF to the lipid interface. Together with the state of the lipid monolayer, also the partition coefficient of VWF between surface and bulk changes. Thus, to account for changes of the membrane state, due to the presence of contaminants in general, or globular proteins in particular, the following chapter treats the impact of nanoparticles on the state of lipid membranes. In conclusion this work represents a first successful step towards an integrative thermodynamic understanding of VWF-membrane interaction.

7. Chemical and mechanical impact of silica nanoparticles on the phase transition behavior of phospholipid membranes in theory and experiment

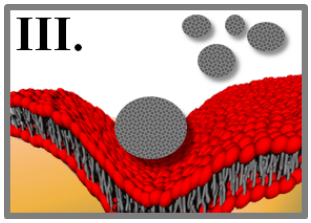

For the understanding of the interaction of nanoparticles (NPs) and living cells the interaction of NPs with lipid membranes is an integral step. During particle uptake, the membrane has to bend. The fact that the modulus of compression of these membranes can vary by more than one order of magnitude, due to the nature of their phase diagram, requires that both thermodynamic and mechanical aspects of the membrane are considered simultaneously. We demonstrate that silica NPs have at least two independent effects on the phase transition of phospholipid membranes: a chemical effect resulting from the finite stability of the NPs in water and secondly a mechanical effect which originates from a bending of the lipid membrane around the NPs. This chapter is based on our report on the experiments which allow to clearly distinguish both effects [67]. A thermodynamic model including the elastic energy of the membranes is predicted, which correctly predicts our findings both quantitatively and qualitatively. Furthermore the NPs can be taken as simple and well characterized mimetics for proteins regarding physical effects like induced curvature.

7.1. Introduction - State of the art

The increasing amount and variety of artificially produced nanometer scale particles calls for a thorough understanding of the influence of such nanopar-

ticles on biological material. Especially the uptake in human cells and its consequences are in the focus of many research teams [68, 69]. Silica nanoparticles (NPs) not only occur in exhaust emissions, but are also additives to food, textiles and construction materials to improve their properties [70]. Moreover, they are even considered for drug delivery [71]. In particular the uptake of NPs by living cells has recently become subject of risk assessments, as it correlates with cytotoxicity [21]. In this context, it has been shown before that clathrin-dependent endocytosis is the most important pathway for the cellular uptake of silica-nanoparticles [22]. For the detailed understanding of endocytotic mechanisms it is helpful to study first the mechanical properties of pure lipid membranes, which have been shown to be suitable model systems for cell membranes [72]. Here, one has to bear in mind that the elastic properties of the lipid membrane depend on its thermodynamic state and can vary substantially. Especially during the transition from the gel to the fluid phase, the bending modulus changes by at least one order of magnitude [62, 73]. Indeed, it has been demonstrated that this phase transition can trigger a variety of morphological transitions even in the absence of membrane proteins. Tube formation, fission, budding as well as the expulsion of entire vesicles have been reported [74, 75, 76, 77]. The thermodynamic state of the membrane must therefore definitely be considered as an important factor for the understanding of transport mechanisms in cells. The lipid phase transition can be conveniently monitored by Differential Scanning Calorimetry (DSC) which allows to detect even minor changes in the membrane properties [78]. In 1992, Naumann et al. were able to demonstrate that 1,2-dipalmitoyl-sn-glycero-3-phosphocholine (DPPC) bilayers on a spherical particle support ($R \approx 300\,\mathrm{nm}$) melt cooperatively, but exhibit a suppressed pre-transition [79]. Using particles of two different sizes ($R \approx 30\,\mathrm{nm}$, $R \approx 300\,\mathrm{nm}$), it has further been shown that the transition temperature of supported membranes is related to their curvature, i.e. the radius of the particles [80]. Finally, for vesicles with diameters below 100 nm, the same concept has been applied to analyze the influence of differences in the curvatures of the inner and outer leaflet on the transition temperature T_M [81].

Here, we employ DSC to characterize the impact of the same NPs that have been shown to be cytotoxic for human endothelial cells [21] on different phospholipid membranes. We investigate spherical supported vesicles (SSV) in terms of their transition temperature and find significantly different dependencies on the membrane curvature for different lipid-chain-lengths. A thermomechanical model is developed being able to explain our experimental findings by including the bending energy of the bilayer into the thermodynamic potential. In addition, a chemically induced depression of T_M is reported, which is triggered by the release of small amounts of silicic acid (SA) from the NPs.

7.2. Materials and Methods

Silica particles with the following diameters were used: d =(16±2)nm, (18±2) nm, (85±4)nm, (212±25)nm, (305±35)nm and (348±40)nm. All NPs used were synthesized and analyzed as described earlier in detail by Blechinger et al. [22]. 1,2-Ditridecanoyl-sn-glycero-3-phosphocholine (13:0PC), 1,2-dimyristoyl-sn-glycero-3-phosphocholine (DMPC or 14:0PC), 1,2-dipentadecanoyl-sn-glycero-3- phosphocholine (15:0PC), 1,2-dipalmitoyl-sn-glycero-3-phosphocholine (DPPC or 16:0PC) and 1,2-diarachidoyl-sn-glycero-3-phosphocholine (20:0PC), dissolved in chloroform, were obtained from Avanti polar lipids (USA) and used without further purification. Suspensions of vesicles and NPs were prepared by re-hydrating a dried lipid film with a dispersion of NPs in ultrapure water (pure Aqua, Germany;18.2MΩcm). The final lipid concentration was 1 mg/ml. For the multi lamellar vesicle (MLV) preparation, the sample was heated above the main phase transition temperature T_M for 60 minutes and vortexed several times. Afterwards, the solution was either sonicated above T_M for 30 min or directly loaded into the calorimeter. The pure NP dispersions as well as the spherical solid-supported vesicles (SSV) containing sonicated samples were analyzed regarding their colloidal stability. Dynamical light scattering analysis shows that the hydrodynamic radius of such samples does not change significantly over typical experimental timescales, i.e. several hours (see fig. 7.1). Also the observation of different dried samples by SEM/TEM shows no signs of big agglomerates or groups of particles that are covered with one continuous bilayer, what would decrease the effective curvature of the membrane.

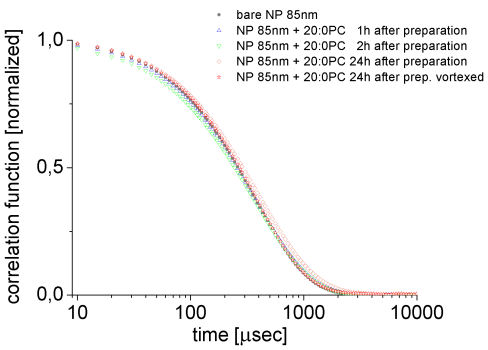

(a) DLS data of different SSV samples.

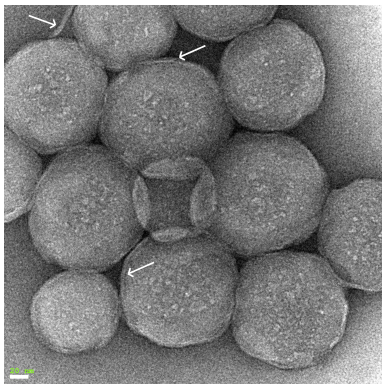

(b) TEM picture of SSV sample

Figure 7.1.: (a) Correlation functions of different SSV samples show no significant hints for agglomeration of coated particles. **(b)** TEM picture of a SSV sample from [12]. Arrows indicate stained lipid layer (scale bar 20 nm).

The measurements were carried out with a Microcal VPDSC Differential Scanning Calorimeter [19] at a scan rate of 17 K/h. The reference sample was ultrapure water. The supernatant of centrifuged NP dispersions was analyzed with electrospray ionization mass spectrometry (ESI-MS, Thermo Finnigan LTQ FT, resolution 100.000 at m/z=400, up to 2000 u, 4 kV, heating capillary temperature 250°C) to quantify the most frequent oligomers of silicic acid released from the NPs.

7.3. Results and Discussion

7.3.1. Chemical impact of silica NPs on T_M

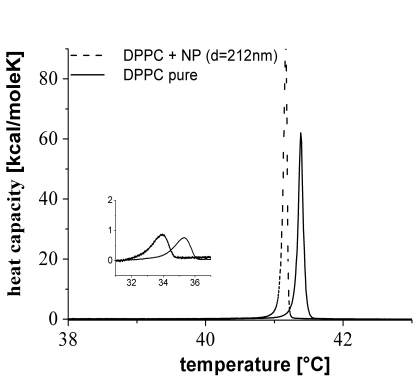

(a) Heat capacity profile of a MLV sample.

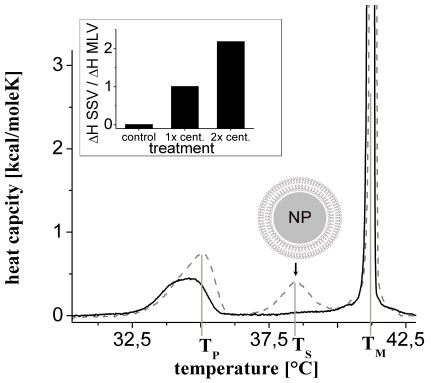

(b) Heat capacity profile of a SSV containing sample.

Figure 7.2.: (a) The heat capacity profile of a DPPC MLV sample is shifted to lower temperatures depending on NP concentration. **(b)** After a week of storage at 4°C of a MLV sample, in $C_p\,(T)$ an additional peak appears. Inset: The enthalpy ratio r of the peaks at T_S and T_M is increased after one respectively two centrifugation steps with discarding of the supernatant. The increase of r shows hat this peak origins from a supported lipid population.

When adding NPs to a suspension of MLV, both the main transition and the pre-transition peaks shift towards lower temperatures (see fig. 7.2a). To quantify this effect, the peak position of the main transition T_M was analyzed as a function of particle concentration and size (fig. 7.3a). The mass concentration c_m was chosen such to keep the total NP surface area per sample in the same range for all NP sizes. Thus, c_m covers a wider range for the larger NPs (fig. 7.3a).
Our experiments revealed the following trend: independent of particle size, the temperature shift of the main transition exhibits a linear dependence on the

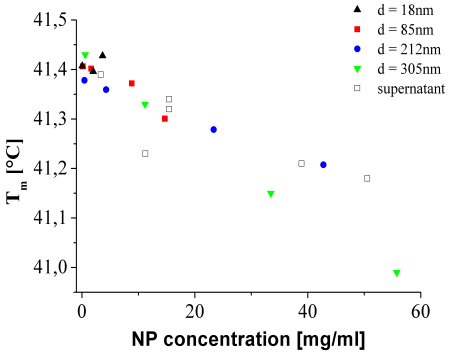

(a) T_M of DPPC NP samples as function of NP concentration.

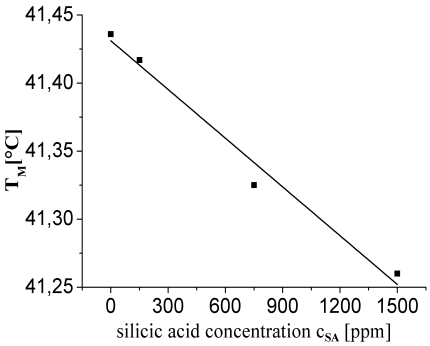

(b) T_M of a DPPC sample as function of SA concentration

Figure 7.3.: (a) T_m of DPPC MLV shows a linear shift with increasing NP mass concentration independent of NP size. NP free samples containing an equivalent amount of supernatant of centrifuged NPs show almost the same behavior (open squares). **(b)** Samples with oversaturated silicic acid show a linear shift in T_M in the same order of magnitude as the NP containing samples.

total amount of added NP mass which indicates an effect that is not related to the total particle surface. The measurements were then repeated substituting the particles by the supernatant of the centrifuged NP dispersions of adequate particle concentration (10000 g, 3 min-300 min, depending on NP size). Fig. 7.3a shows that the temperature shift of such NP free samples is equal to the corresponding NP containing samples. Therefore, the shift in T_M with increasing concentration does not arise from the physical presence of the NPs, but can rather be caused by substances dissolved from the NPs. This is confirmed by the fact that an increase in incubation time of washed NPs, leads to an increasing shift in T_M as well. Alexander et. al. [82] already reported that silica always partially dissolves in aqueous solutions, forming silicic acid oligomers (SA). According to equation 42 of [83], 95% of the equilibrium concentration of silica in water should be reached within nine hours in the case of the used NPs. The equilibrium concentration of SA is in the range of 150 ppm [82, 84]. ESI mass spectra showed that tetramers (m/z = 274.8809) and pentamers (m/z = 370.8693) are the most frequent oligomers in our NP dispersions (data not shown).

To confirm that SA is indeed the origin of the decrease in T_M, freshly prepared and oversaturated SA solution was added to MLV samples. A linear decrease in T_M as presented in fig. 7.3b was found. Regarding the hydrophilic character of SA [85] we expect head group effects to cause the observed melting point depression. One possible explanation could be an altered solvation

of both lipid phases in a SA solution compared to water. Disregarding the specific nature of the SA-lipid interaction, we assume that the solute SA influences the chemical potentials of gel phase μ_{gel} and fluid phase μ_{fluid}:

$$\mu_i(T) = \mu_i^w(T) + \Delta\mu_i^{tr}(T) \tag{7.1}$$

μ_i^w denotes the standard chemical potential of the corresponding lipid phase in water and μ_i^{tr} the free energy associated with a transfer of the phase from water to the solution. Along these lines Chapman et al. [10] has derived that for the shift of the transition temperature ΔT_M:

$$\Delta T_M = \left[-\left(R{T_M}^2\right) / \left(\Delta H\left(T_M\right)\right)\right] \alpha c_{SA} \tag{7.2}$$

where R is the gas constant, T_M the melting temperature of the lipid in pure water, $\Delta H(T_M)$ the change of the systems enthalpy at T_M and c_{SA} the concentration of the solute SA. For low concentrations c_{SA} and small temperature changes α is a constant that depends on the strength of the interaction of the solute with both phases, i.e. the values of $\mu_{gel}^{tr}(T_M)$ and $\mu_{fluid}^{tr}(T_M)$.

It is noteworthy that equation 7.2 should be true for a direct interaction between lipid phases and solute as well as for indirect influences as for example solvation effects. Our measurements with oversaturated SA suggest a proportionality constant of A= 0,119 mK/ppm. Here we want to emphasize that silica nanoparticles release small amounts of SA which can significantly influence the thermodynamic properties of lipid membranes. The concentration of dissolved SA seems to be approximately proportional to the mass concentration of nano particles in the dispersion, and does not dependent on their size (fig. 7.3a). Future studies should take that effect into account, regardless of the curvature-induced effect explained in the following section.

7.3.2. Preparation of spherical solid-supported phospholipid bilayers

Storing the samples for one week after preparation led to the occurrence of an additional peak in the DSC profile at a temperature T_S (see fig. 7.2a). After sonication, this additional peak becomes more pronounced than the original one at T_M, indicating an increasing portion of the lipids undergoing the transition at T_S following this step. Some samples were centrifuged after sonication at 10000 g for 15 to 60 minutes. Before repeating the centrifugation step, the supernatant was replaced with ultrapure water. In the inset of fig. 7.2a, the ratio of the transition enthalpies of the additional (ΔH_S) and the main transition (ΔH_M) is shown before and after centrifugation. While this ratio is only about 0.01 for the untreated sample, it increased to 1 after the first and to 2.2 after the second centrifugation step. This clearly indicates that the

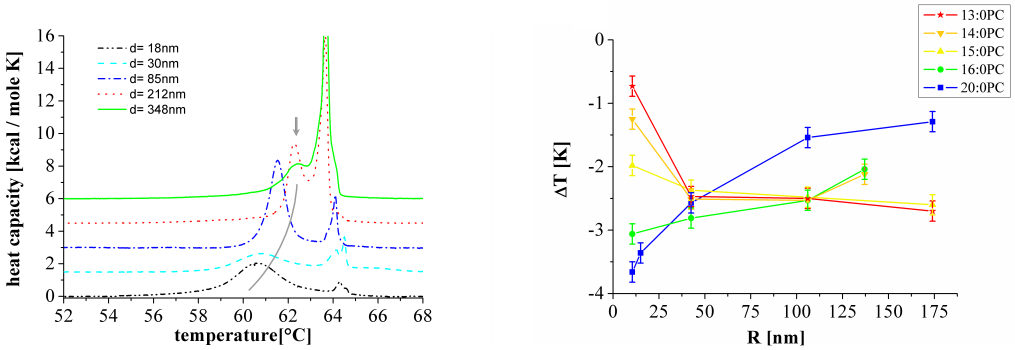

(a) Heatcapacity as function of temperature for 20:0PC

(b) ΔT for different lipid chain lengths

Figure 7.4.: (a) Heat capacity of 20:0PC samples with different sized NPs and comparable amount of total NP surface. Baselines are shifted for clarity. The arrow and the gray line indicate the shift of the SSV peak with increasing NP size. **(b)** The difference ΔT := T_S - T_M as function of NP radius for various lipid chain length show systematic differences for increased NP curvature.

additional peak at T_S has its origin in lipids which are attached to the NPs. This observation and conclusion is consistent with the findings of Naumann et al. and Bayerl et al. [79, 86] who coated NPs with lipid membranes and reported comparable shifts in T_M. Furthermore, in 1996, Brumm et al. [80] showed some differences in the curvature dependence between 14:0PC and 18:0PC, but these reports left the question about a systematical study of the influence of the NP size open.

Hence, the heat capacity profile of the supported membrane population was analyzed both for NPs of different diameters (18 nm - 348 nm) and lipids with different chain lengths between 13 and 20 carbon atoms but identical head group. To account for the above mentioned chemical melting point depression, we analyzed the difference $\Delta T := T_S - T_M$ between the transition temperatures of free and supported lipids (see fig. 7.2b). Assuming that the above chemical effect is of the same order for as well MLVs as SSV it should cancel out.

All measurements show the same tendency, namely a shift of T_M towards lower temperatures for the solid-supported case. Exemplarily, the heat capacity profiles for 20:0PC are shown in fig. 7.4a for different NP sizes. The expected broadening [79] of the SSV due to decreasing cooperativity with increasing membrane curvature was observed but not analyzed further.

Fig. 7.4b shows ΔT for different lipids and NP diameters. While ΔT decreases with decreasing NP diameter for 13:0PC, 14:0PC and 15:0PC, it increases for 16:0PC and 20:0PC. For all lipids, except for 20:0PC, the limit for a flat support of zero curvature is roughly $\Delta T = -2,5K$.

To summarize, our results consist of three main observations: i) for all lipids and NP sizes, T_S shifts towards lower temperatures, with a ΔT ranging between -0.5 K and -4 K, ii) the curvature dependence changes its sign for increasing chain length and iii) for all lipids, ΔT shows a saturation behavior with decreasing curvature.

7.3.3. Theory. Bending contribution to ΔT

In the case of SSV, the vesicles spread on and cover the NPs or parts of them, hence experiencing a curved substrate. In the following paragraph, an analytical expression for the expected change in phase transition temperature T_M based on the mechanical and calorimetric properties of the system will be derived. We therefore integrate the bending energy of the membrane in a Landau-type potential. No new or additional model assumptions are introduced. Instead, we combine existing theories to provide a coherent explanation of our results.

Contributions to the Landau potential

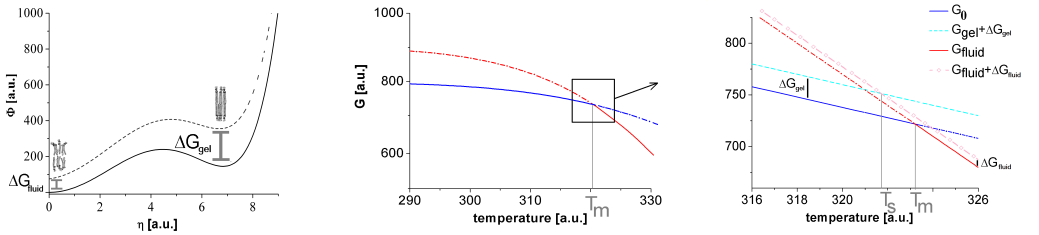

(a) Landaupotential (b) Identification of minima with G (c) Linear approximation around T_M

Figure 7.5.: (a) A Landau potential as function of a order parameter η shows two minima. At low order the membrane is fluid, while the high ordered state is identified with the symmetrical gel phase. The NP changes the complete potential, especially the minima. **(b)** The minima of the potential are identified with the Gibbs enthalpy G and plotted as function of temperature. At low temperatures the fluid phase is energetically disadvantageous, whereas this changes at the intersection of the two curves. **(c)** Linear approximation around T_M. As well G_{gel} as G_{fluid} are shifted by $\Delta G_{gel/fluid}$. Thus, the new cross section is at the melting temperature T_S.

In the Landau theory, a first order phase transition is represented by the relative evolution of the double well potential of the form shown in figure 7.5 [87, 88]:

$$G = G_0 + A\eta^2 + B\eta^4 + C\eta^6 \tag{7.3}$$

Here, η is the order parameter and $A(T, p, \Pi), B(p, \Pi), C(p, \Pi)$ are functions of the thermodynamic variables temperature T, bulk pressure p and lateral pressure Π.

It is convenient and common to consider only the evolution of the potential minima in η with temperature. These are commonly identified with the Gibbs Free Energy potentials for the gel phase and the fluid phase [89, 90] as indicated in figure 7.5.
In the absence of any solid support, the two potentials intersect at the phase transition temperature T_M. The additional energies ΔG_{gel} and ΔG_{fluid} in the presence of the support shifts the intersection towards lower temperatures T_S (see fig. 7.5c). For the transition temperature T_S now holds:

$$G_{gel}\left(T_s\right) + \Delta G_{gel} = G_{fluid}\left(T_s\right) + \Delta G_{fluid} \tag{7.4}$$

Assuming the pressure p to be constant and $\frac{\partial^2 \Pi}{\partial^2 T} \approx 0$ as shown in [65], $G_{gel}\left(T\right)$ and $G_{fluid}\left(T\right)$ can be approximated by a first order Taylor series near the transition point T_M:

$$\begin{aligned} G_{gel}\left(T_m\right) + \left.\frac{\partial G_{gel}}{\partial T}\right|_{T_m} \left(T_s - T_m\right) + \Delta G_{gel} = \\ = G_{fluid}\left(T_m\right) + \left.\frac{\partial G_{fluid}}{\partial T}\right|_{T_m} \left(T_s - T_m\right) + \Delta G_{fluid} \end{aligned} \tag{7.5}$$

and consequently:

$$\Delta T := \left(T_s - T_m\right) = -\frac{\Delta G}{\left.\frac{\partial G_{gel}}{\partial T}\right|_{T_m} - \left.\frac{\partial G_{fluid}}{\partial T}\right|_{T_m}} =: -\frac{\Delta G}{\Delta\left(\frac{\partial G}{\partial T}\right)} \tag{7.6}$$

This general analytical expression relates the contribution of the solid support to the free energy $\Delta G_{gel/fluid}$ with the shift of the transition temperature ΔT.

$\Delta\left(\frac{\partial G}{\partial T}\right)$ from the heat capacity profile

$\Delta\left(\frac{\partial G}{\partial T}\right)$ can be extracted from the experimental DSC data, recalling the relation between the thermodynamic potential G and the heat capacity c_p as its susceptibility:

$$-T\left.\frac{\partial^2 G}{\partial T^2}\right|_p = T\left.\frac{\partial S}{\partial T}\right|_p = c_p \tag{7.7}$$

In agreement with the linear approximation that was described above, we have to integrate over $\frac{\partial^2 G}{\partial^2 T}$ (respectively c_P) in the transition region to get

$\Delta\left(\frac{\partial G}{\partial T}\right)$:

$$\Delta\left(\frac{\partial G}{\partial T}\right) = \int_{T_1}^{T_2} \frac{\partial^2 G}{\partial T^2}\,\mathrm{d}T = -\int_{T_1}^{T_2} \frac{c_p}{T}\,\mathrm{d}T \approx -\frac{\Delta H}{T_m} \tag{7.8}$$

The last approximation introduces the transition enthalpy ΔH and holds for sharp transitions for which a constant temperature T_M can safely be assumed.

Mechanical contributions to ΔG

In the case of SSV, we consider two main contributions to ΔG: i) a curvature dependent one caused by the bending of the membrane and ii) a curvature independent one due to the bare presence of the substrate (planar limit). The latter, constant contribution to ΔG can be caused by various interactions between lipids and support, for example by electrostatic forces. To describe the mechanical contribution due to curvature, we use the well-known expression for the bending energy E_{bend} of a membrane [91]. For the curvature independent contribution we add an additional constant contribution ΔG_S:

$$\Delta G = E_{bend} + \Delta G_s = \frac{1}{2}\left(\frac{2}{R} - c_0\right)^2 \kappa A_m + \frac{1}{R^2}\kappa_G A_m + \Delta G_s \tag{7.9}$$

Here, A_m is the area per lipid molecule, $c_0 := 1/R_0$ is the spontaneous curvature, κ the bending modulus and κ_G the modulus of Gaussian curvature. In the case of a chemically symmetric bilayer, the spontaneous curvature is caused by the asymmetry of the environment due to the NP and a thin layer of water inside and the bulk water outside the vesicle. The bending radius R is simply determined by the radius R of the particle.

Due to the higher flexibility of lipid membranes in the fluid phase, we assume a stronger contribution of the mechanical bending energy to Φ for the low symmetric gel phase (fig. 7.5). Therefore we neglect the bending energy contribution to ΔG_{fluid}. The final expression for the temperature shift ΔT can then be found by combining eq. 7.6, eq. 7.8 and eq. 7.9:

$$\Delta T := -T_m \frac{\frac{1}{2}\left(\frac{2}{R} - c_0\right)^2 \kappa_{gel} A_m + \frac{1}{R^2}\kappa_{G_{gel}} A_m + \Delta G_{gel} - \Delta G_{fluid}}{\Delta H} \tag{7.10}$$

where κ and κ_G are the mechanical parameters for the gel phase and $\Delta G := \Delta G_{gel} - \Delta G_{fluid}$. This expression explicitly relates the shift ΔT of the main phase transition temperature with the mechanical and the calorimetric properties of the membrane and predicts trends which can be compared with the experiments.

7.3.4. Discussion - Bending energy explains the curvature dependence of ΔT

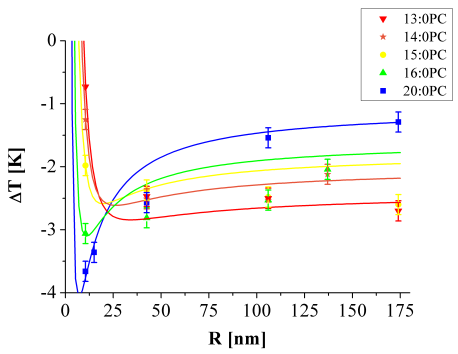

(a) Fit of ΔT

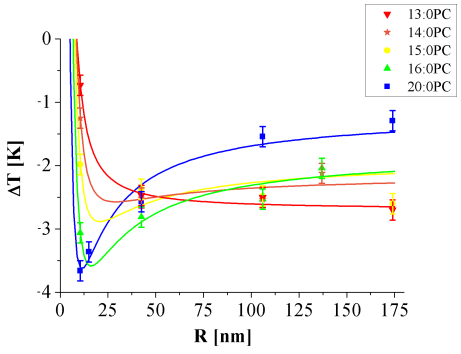

(b) Two parameter Fit of ΔT (ΔG 150J/mol

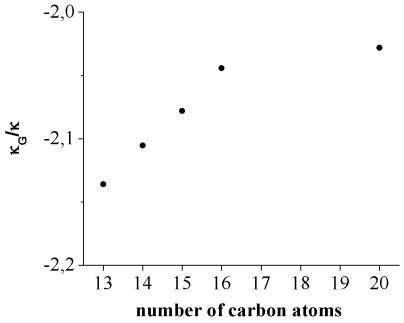

(c) κ_G/κ

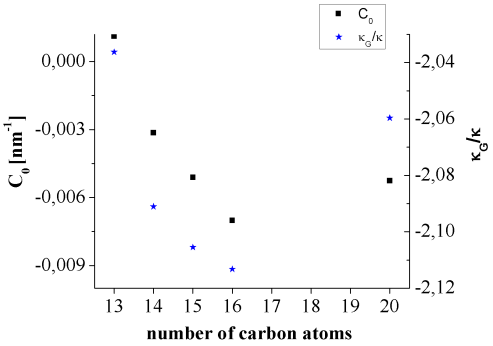

(d) Results of the two parameter fit

Figure 7.6.: (a) Fit of eq. 7.10 with ΔT ($\Delta G = 140\,\mathrm{J/mol}$, c_0 = -250nm) **(b)** Fit of eq. 7.10 with ΔT ($\Delta G = 150\,\mathrm{J/mol}$). **(c)** Ratio of κ_G and κ as function of lipid chain length. **(d)** $c_0 = 1/R_0$ and z as function of lipid chain length.

In figure 7.6, we show that our thermodynamic model can indeed well explain the observed trends of the temperature shift for different lipid chain lengths. Equation 7.10 was fitted to the data points of fig. 7.4b. T_M and ΔH were taken from the heat capacity profiles, κ was set to $2,510^{-18}J$ for 16:0PC and estimated according to $\kappa = 2,510^{-18}J(h/16)^3$ for the other lipids, where h is the number of carbon atoms of the hydrophobic chains of the lipids [92, 93]. Furthermore A_{mem} was set as $0,5\,nm^2$ and R is the radius of the NPs. Thus there are three unknown parameters $\kappa_G, \Delta G_S$ and $1/R_0$. We will show that κ_G turns out to be the crucial parameter.
Initially we perform a three parameter fit ($\Delta G_S, R_0, \kappa_G$ free) to get a first estimate for the magnitude of the free parameters (see fig. C.2). As ΔG_S denotes a mainly head group associated energy contribution it is reasonable to

consider ΔG_S as constant. Consistent fits are achieved for $\Delta G_S = constant = 150 J/mol$. The two parameter fit with fixed ΔG_S (fig. 7.6b) still shows good qualitative and quantitative agreement between theory (eq. 7.10) and experiments (see fig. 7.6). The values for R_0 and κ_G are comparable to those of the three parameter fit mentioned before (see fig. 7.6d).
Since the fit parameters affect each other we also compare the aforesaid results with a one parameter fit by additionally keeping R_0 fixed (see fig. 7.6a, $\Delta G_S = 140\, J/mol, R_0 = -250nm$). We still achieve very good agreement between the measurements and the analytical curves from eq. 7.10.
For all fits the ratio $z := \frac{\kappa_G}{\kappa}$ is a critical parameter, which turns out to be roughly -2 for all experiments. Independent of ΔG_S and R_0 any substantial deviation from -2 would predict transition temperature shifts ΔT of more than an order of magnitude larger than the ones observed. Our model therefore delivers the ratio z as predicted by Helfrich for the transition regime from lamellar to vesicular phase [94]. In [94] it is shown, that from a known stress profile, i.e. lateral stress as a function of the position on a axis perpendicular to the membrane plane, one can estimate κ_G as the second moment of the stress. Due to interfacial tension in the head group region of a lipid bilayer in literature negative stress is assumed [94], whereas in the hydro carbon chain region the stress is positive. In equilibrium the sum over the stress has to cancel out [94]. To model lipids with identical head group but varying chain length h and satisfy the aforementioned conditions the arbitrary values for $s(x)$ are taken as shown in fig. 7.7a. In eq. 7.11 it is shown that κ_G in this model is a quadratic function of h. The results of κ_G from the fit in fig. 7.6 show also a quadratic dependence of h.

$$\begin{aligned}\kappa_G &= 2\int_0^{h_0 z+k} x^2 s\,(x)\ \mathrm{d}x = 2\int_0^{h_0 z} x^2 s\,(x)\ \mathrm{d}x + 2\int_{h_0 z}^{h_0 z+k} x^2 s\,(x)\ \mathrm{d}x = \\ &= 2\int_0^{h_0 z} \frac{x^2 A}{h z_0}\,\mathrm{d}x + 2\int_{h_0 z}^{h_0 z+k} \frac{-x^2 A}{k}\,\mathrm{d}x = -\frac{4A}{3}h^2 {z_0}^2 - 2Ahz_0 k - \frac{2Ak^2}{3}\end{aligned} \tag{7.11}$$

In a similar manner theoretical considerations can predict the spontaneous curvature. But in fits with R_0 as free parameter and fixed z a contradiction to this earlier theoretical work [94, 95] appears. Instead of a decrease in the spontaneous curvature $1/R_0$ with increasing h, as theoretically predicted, the fit indicates an increase. A more thorough understanding of ΔG_S as well as better models and more than currently available on R_0 will hopefully improve the model in the near future. Along the same lines a refined model would account for more subtle differences in bending energy between fluid and gel phase and consider variations in A_{mem}.

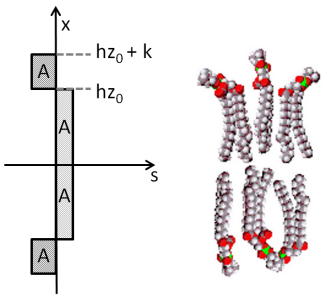

Figure 7.7.: Simplified stress profile of a lipid bilayer. x-coordinate is the distance on an axis perpendicular to the membrane plane.

7.4. Conclusion

In summary, we present in-depth theoretical and experimental studies on nanoparticle-membrane interaction showing that silica NPs are able to influence the thermodynamic state of lipid membranes via at least two different mechanisms. First, a melting point depression caused by silicic acid released from the NPs in aqueous solution has been clearly identified, calling for a thorough analysis of the chemical stability of NPs prior to studies on their interaction with biological matter. Even minute amounts of soluble substances can change the thermodynamic properties of lipid membranes significantly. Apart from this chemical aspect, we also found a size dependent impact of silica nanoparticles on the thermodynamic properties of phospholipid membranes mediated by the bending energy of the membrane. An analytical expression is proposed, which describes the shift in T_S of solid-supported lipid bilayers by thermodynamic and mechanical considerations. Together with further experimental data this could offer a way to estimate the modulus of Gaussian curvature of lipid membranes, a parameter that is very difficult to access otherwise. Finally, we like to point out that earlier work has demonstrated, that ion permeability, morphological changes or adhesion phenomena can be controlled by a shift in the thermodynamic state of the lipid membranes [96, 76, 89, 97]. A comparison between these data and the shift in state by NPs observed here, demonstrates that NPs are in principle capable to induce the phenomena mentioned. We believe that similar changes in membrane state may be induced in membranes of cells. In experiments with our collaborators [21] we have shown that the same NPs studied here increase their toxicity with total surface area and not simply with mass, which clearly exemplifies the role of NP-cell membrane contact. It will be interesting to find out to what extent this contact modifies the thermodynamic state of the cell membrane.

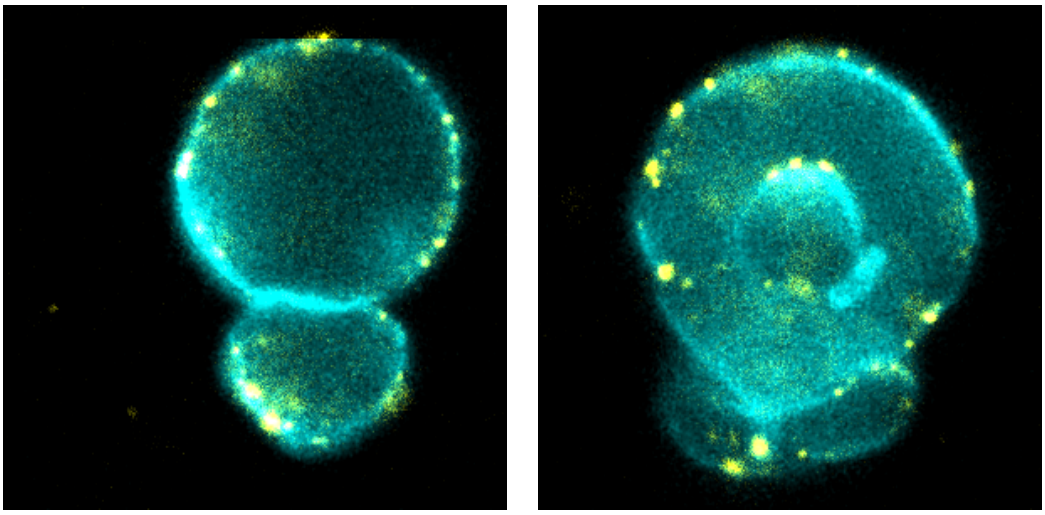

(a) DPPC GUV with NPs before phase transition

(b) DPPC GUV with NPs after phase transition

Figure 7.8.: (a) A DPPC GUV (blue) with adhered NP (yellow) before phase transition. The NPs are on the outside of the vesicle. **(b)** After the temperature induced phase transition the NPs are inside the mother vesicle. During phase transition intravesicular budding appeared.

7.5. Outlook - manipulation of membrane morphology by NPs

As a further step towards NP cell membrane interaction the impact of NPs on on GUV was studied. These GUV are modell membranes that are similar to cell membrane concerning dimensions.
As reported detailed in [12] we studied DPPC GUV and NPs labeled with different dyes with our cooperation partners. In figure 7.8 is shown that NP adhere to the membrane and indeed can change the morphology of the membrane.

The main observations of the temperature induced phase transition behavior of these GUV are:

- During phase transition, instead of the typical extravesicular budding behavior, various other effects can be seen (increased intravesicular budding, tube formation, no visible shape changes).
- NP can enter the GUV via intravesicullar budding during phase transition without the presence of other proteins like e.g. clathrin.
- Correlation of membrane parts with higher curvature and localization of NPs.

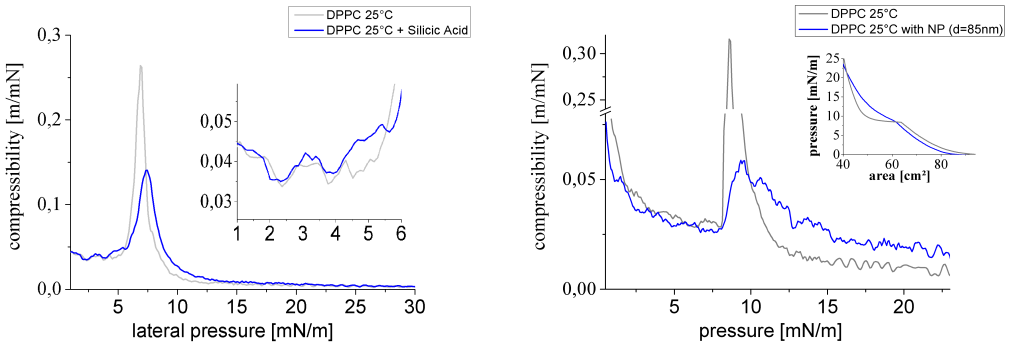

(a) Compressibility of a DPPC monolayer in presence of SA

(b) Compressibility of a DPPC monolayer in presence of NPs

Figure 7.9.: (a) Compressibility of a DPPC monolayer with and without silicic acid in the bulk. **(b)** Compressibility of a DPPC monolayer in absence and presence of NPs. Aqueous NP solution was sprayed on top of the monolayer. After equlibration of the lateral pressure again isotherms were measured.

This means NPs can overcome the barrier of a lipid bilayer with out any other proteins or signal cascades like shown in [3]. Of course in the case of our experiments the change of state of the lipids was induced by an overall temperature increase, which will not happen in vivo. But the principle effect that processes in biology take advantage of phase transitions is supported by our experiments, as the phase transition temperature is shifted by the NPs and for example the appearance of pores in lipid bilayers is increased near the phase transition [97]. Furthermore local changes in membrane elasticity could explain the observed effects as described in [12]. To analyze the influence of NPs on membranes within a broader range of physical states we also studied the impact of NPs on lipid monolayers. This is justified as the bending modulus κ of a bilayer and the isothermal lateral compressibility of a monolayer are connected [62].

In figure 7.9 we show the impact of SA as well as NPs on DPPC monolayers. While the first does not significantly change the elastic parameters of the monolayer, the latter can induce a significant increased compressibility in the liquid condensed phase. In the experiments with SA the isothermal compressibility of a DPPC monolayer was measured with saturated silicic acid in the bulk. As even that high concentrations do not significantly change the elastic properties of the membrane, we exclude this effect as origin for the observed morphological changes. In contrast, in figure 7.9b we show the compressibility of DPPC before and after spraying aqueous NP solution on top of the monolayer. The typical clear phase transition peak is lowered and the compressibility in the liquid condensed phase is increased by a factor of

roughly two. However, it has to be mentioned here, that experiments with NPs in the bulk solution did show no significant impact on the compressibility of a monolayer. On the one hand this may be due to the much lower NP bulk concentrations compared to the DSC experiments. On the other hand the stronger influence of NPs on the membrane due to bending (SSV) is very unlikely to happen with a monolayer. Also the sedimentation of the NPs due to gravity decreases possible NP lipid contacts. To conclude, also on the microscopic level strong NP membrane interaction can be observed. Hopefully in near future this ongoing research will help to understand amongst others cellular uptake mechanisms and the role of physical effects, e.g. due to adhered proteins, better. Nevertheless, if one transfers the ability for changes in the elasticity of a membrane to membrane damages and cytotoxicity in vivo, this also fits with the fact that cytotoxicity of those silica NPs is a function of overall supplied NP surface area and not NP mass (compare[21]). In summary, these studies show how the advantages of an interdisciplinary approach contribute to the clarification of membrane associated processes, like endocytic uptake mechanisms in nature.

8. Membrane state regulates acitvity of membrane bound protease ADAMTS13

8.1. Introduction

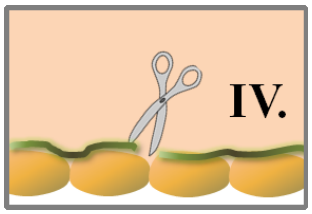

It is known a lot about the effects of enzymes on chemical reactions, but the mechanism behind it still is somehow a mystery [98]. The catalytic rates of many enzymes show a temperature dependence that is in accordance with a constant activation energy and following the arrhenius equation as described in chapter 4. But for several membrane associated enzymes it has been reported that the arrhenius plot shows kinks at certain temperatures. Different slopes in these plots correspond to different activation energies. The reason for this can be enzyme deactivation at higher temperatures, altering of binding affinities between substrate and enzyme, pH changes that influence reaction velocities or phase state changes in enzyme or membrane [99]. The latter ones are the most interesting ones, as physical states of membranes are influenced by a variety of parameters (e.g. temperature, pH, pressure, charges, chemical potential).
In chapter 4 the importance of ADAMTS13 for the biological function of VWF is clearly shown. Hemostasis usually takes place at vulnerations of the blood vessel system, where the VWF is adhered to the membrane of the cells at the vessel wall and then binds platelets to form a plug. In that environment the substrate is connected to membranes. Together with the knowledge about the changes in activity of membrane bound enzymes, as mentioned above, this leads to the question whether the physical state of the membrane controls enzyme activity in the case of membrane bound ADAMTS13.
It is reported that the fluidity of the membrane is a crucial parameter for the activity of membrane bound enzymes like ATPase [100]. We show that this is even the case for the water soluble enzyme ADAMTS13, when it is bound artificially to a lipid membrane. Furthermore we continue here the discussion on the theory of proper entropy of interfaces [101, 102]. It was shown for

Acetylcholinesterase (AChE) that the physical state of a monolayer plays the crucial role for the activity of the enzyme [101]. There the catalytic rate k of the
enzyme was shown to be coupled to the fluctuations in area of the monolayer and hence to the isothermal lateral compressibility κ. In that work the focus was especially on the maximal enzyme activity in the vicinity of the phase transition from liquid expanded to liquid ordered phase of the monolayer.
As the matrix of biological membranes is a lipid bilayer, an experiment where the enzyme is bound to lipid vesicles in aqueous solution is a step closer to biology. For this reason the activity of membrane bound ADAMTS13 is studied as function of temperature and hence as function of the membrane state.

8.2. Materials and Methods

All used lipids were purchased from Avanti Polar lipids solved in chloroform. If not explicitly mentioned a mixture of 1,2-dipentadecanoyl-sn-glycero-3-phosphocholine (15:0PC) and 1,2-dioleoyl-sn-glycero-3-[(N-(5-amino-1-carboxypentyl)iminodiacetic acid)succinyl] (nickel salt) (NTA-lipids) with a molar ratio of 98:2 and a final concentration of 1.13 mM were used. Detailed studies of the impact of NTA-lipids on the thermodynamic parameters of phosphatidylcholine can be found in appendix D.1.The lipids were dried under vacuum for three hours, afterwards re-hydrated with buffer (pH 6.5; 150 mM NaCl; 50mM Hepes; 5 mM $CaCl_2$; 1 μM$ZnCl_2$) and heated above 45°C for one hour. Mean vesicle diameter was determined as (3100±1400) nm with Dynamic Light Scattering (DLS).
The enzyme ADAMTS13 with a histidin-tag (ADAMTS13His) was used to bind to the NTA-lipids. Per enzyme $\approx$ 2000 NTA-lipids were in the sample. To estimate the to time to bind to the lipids, enzyme with and without his-tag was added to a monolayer on a Langmuir film balance. The increase of pressure as function of time is shown in figure D.4. In the liquid expanded phase state ADAMTS13 without his-tag induced a pressure increase of 2mN/m, whereas the enzyme with his-tag already with halved concentration increased the pressure even above the phase transition pressure. More detailed studies showed, that ADAMTS13His increases the lateral pressure roughly four times higher than ADAMTS13 and that most of the binding process, even without stirring or shaking, happens within two minutes. After the samples (vesicle solution, substrate, buffer) were given in a transparent 96 well plate the system was temperature equilibrated for five minutes. Then the enzyme was added, resulting in 1.8 times human plasma concentration. Within two minutes the solution was shaken for five seconds before the fluorescence readings (BioTek Instruments, Synergy HT, Excitation 485 nm, Emission 528 nm, bottom read-

ing), every 30 seconds for at least 90 minutes, were started. The maximal catalytic rate was determined by a linear fit (five to fifteen minutes) of the steep increase in the kinetic curve, as indicated in figure 8.1a. Furthermore, in fig. 8.1b it can be seen, that the maximal rate is dependent on the substrate concentration for low concentrations.
The heat capacity C_p of the system was measured with a Microcal VPDSC Differential Scanning Calorimeter [19] at a scan rate of 10 K/h. The reference sample was ultrapure water. Absorption measurements were carried out with the same plate reader as mentioned above.

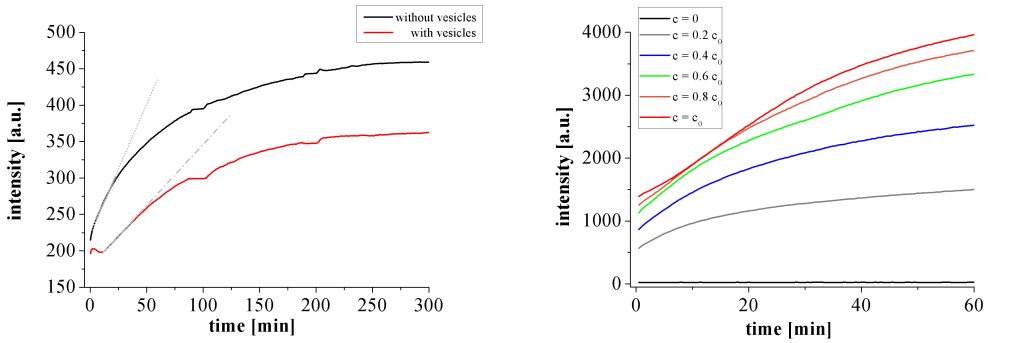

(a) Typical kinetics.

(b) Variation of substrate concentration

Figure 8.1.: (a) Typical kinetics: Intensity as function of time for a vesicle containing and a vesicle free sample at 33°C. The catalytic rate is measured with a linear fit to the steepest increase. **(b)** Kinetics for varied substrate concentration. The reaction rate is dependent on the substrate concentration for low amounts of substrate.

8.3. Theory. Role of membrane state and fluctuations

In [101] the relation between entropy potentials, fluctuations and reaction coordinate is presented theoretically and experimentally in detail. That thesis and the citations therein are recommended to the interested reader. In the experimental section there it is shown that the catalytic rate k of AChE is proportional to κ_T. Thus, the fluctuations in area, which are maximal in the phase transition from the liquid expanded to the liquid condensed phase of the monolayer, are associated with maximal activity of the embeded enzyme. It is stated that the lipid monolayer together with the enzyme and the hydration layer represents one system, that fluctuates in all coordinates as one system. The theory of "proper entropy" can be tested by various selections of the

subspace of the multidimensional phase space. To test this theory in the following part, it is tried to confer this theoretical predictions from a monolayer experiment to a bilayer experiment. In the former mentioned isothermal case the state was varied by variing the lateral pressure. Whereas in vesicle experiments, the state is altered by changing the temperature as the lateral pressure is not accessible. How far the lateral pressure in the membrane is constant for the vesicle experiments is highly discussed [103] but not crucial for our experiment, as the systems is already defined by a couple of parameters. All other controllable parameters (bulk pressure, pH, ion strength) are kept constant. The excess heat capacity C_p has been shown to be direct proportional to the isothermal excess lateral compressibility [65]. Thus in the case of bilayer vesicles C_p is an accessible parameter giving information about the curvature of the corresponding entropy potential. Hence, the fluctuations of the systems are maximal at the maximum of C_p(T).

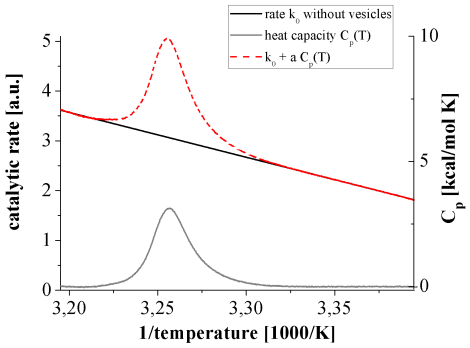

Figure 8.2.: Superposition (red dashed line) of linear fit to the reaction rate for vesicle free samples (black line) and C_p of the vesicle containing samples (grey solid line) with a peak around 34°C.

The activity of free enzyme is already temperature dependent as can be seen in fig. 8.3. Assuming a modulation of the activity of the free enzyme, that shows a linear temperature dependence, with the excess heat capacity, in analogy to the monolayer experiments, one theoretically expects a temperature dependence of the catalytic rate that is dominated by the peak like shape of C_p. A local maximum at T_M would be the consequence (illustrated figure 8.2).

8.4. Results - phase transition temperature divides regimes of activity

In figure 8.3 the catalytic rate of ADAMTS13His cleaving VWF is plotted as function of the inverse temperature. There the catalytic rate k is com-

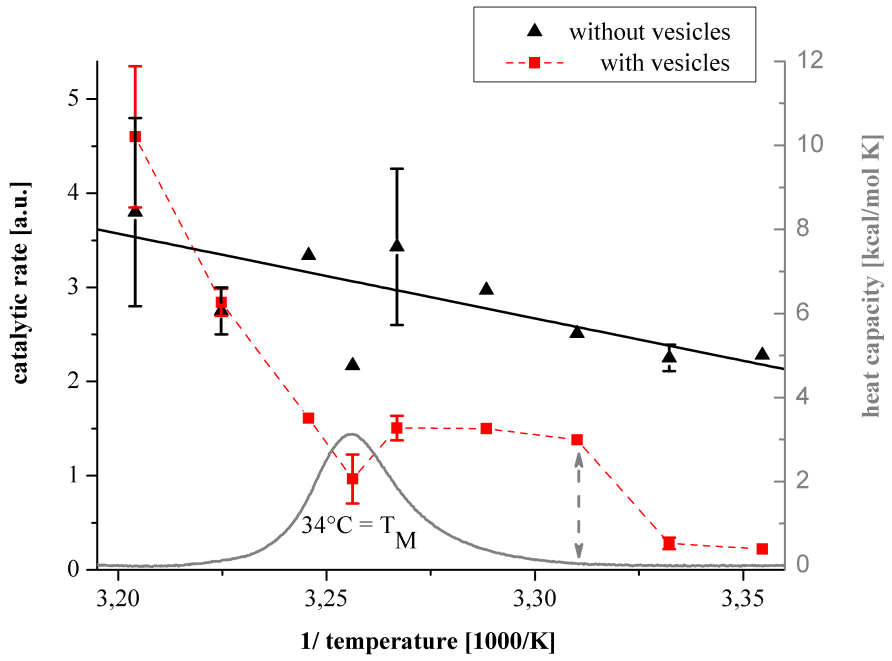

Figure 8.3.: The reaction rate for vesicle free (black triangles) and vesicle containing samples (red squares) as function of temperature (error bars are standard deviations of repeated measurements). C_p of the vesicle containing samples (gray solid line) indicates the phase transition of the vesicles around 34°C. A significant increase happens at the onset of the phase transition (see arrow).

pared for the system with and without vesicles, where all other concentrations are kept constant. The black triangular points show the measured rate of ADAMTS13His in the absence of lipid vesicles. Within the studied range of temperature the catalytic rate can be approximated with a linear function. However the red rectangular points show the rate of the vesicle containing system. In general the intensity saturation values for each temperature of the vesicle containing samples lie around 25% below the values of the vesicle free samples. This can be understood because of the higher absorbance of the vesicle solution. It has to be pointed out here that, in order to minimize any sources of error, no normalization of the intensity values is done. The focus of this work lies on the qualitative difference between the activity of the enzyme ADAMTS13 in bulk solution and in a membrane bound state. Every data pair (T, catalytic rate) represents one ore more kinetic curves. As error bars are provided, the catalytic rate is the mean value of repeated measurements and the error bars are the standard deviation of the corresponding measurements. Furthermore in fig. 8.3 the heat capacity C_p is plotted as function of the inverse temperature. The most pronounced difference in the temperature

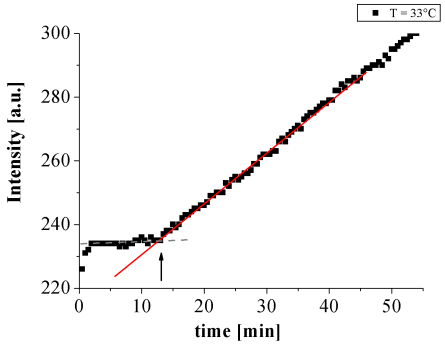

(a) Determination of lag time

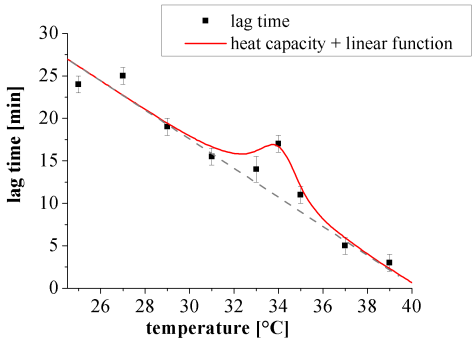

(b) Correlation of lag time outliers and phase transition

Figure 8.4.: (a) The intensity of vesicle containing samples show a certain lag time (arrow at intersection of tangentials) between addition of enzyme and measurable start of the reaction. The fluorescence intensity typically increases rapidly after some minutes. **(b)** The lag time as function of the temperature decreases linearly with temperature besides the temperature range around T_M of the membrane. The heat capacity as a measure for the phase state is added to a linear fit to the data points and demonstrates the correlation of phase transition and this outliers.

dependence of the catalytic rates with and without vesicles is the kink of the catalytic rate of membrane bound enzyme at $34°C$. In the linear regime above the phase transition temperature the slope of the rate as function of temperature is increased by a factor of ten. The data presented in figure 8.3 is measured under the same conditions (fluorescence reader, reading parameters, well plate, batch of lipids and enzymes, any concentrations) as exact as possible. Further measurements were done on other devices, with deviating fluorescence parameters, concentrations and batches. For clarity a quantitative comparison is not done here. But qualitatively those measurements reproduce the effect that the catalytic rate is increased significantly above $34°C$.

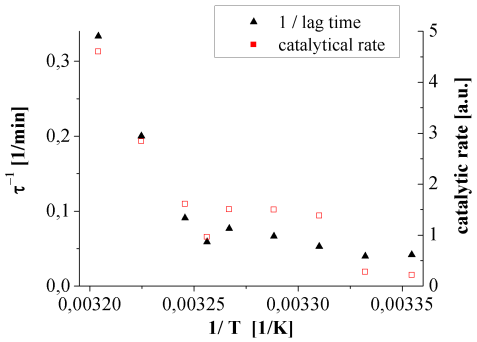

Figure 8.5.: Striking correlation between the inverse lag time (black triangles) and the catalytic rate (open squares).

Besides the mentioned kink, at the main phase transition temperature a slight local minimum in activity can be seen.

Another quantity that can be measured easily and reproducible is the lag time between addition of enzyme to the vesicle containing samples and the steep increase in intensity. In fig. 8.4a an extract of a kinetic is shown. The intensity plateau indi-

cates that no measurable amount of substrate is cleaved for 13 minutes (the increase during the first three data points is discussed later). From this point on the fluorescence intensity increases linearly. The intersection of tangents to this two regimes of the kinetic defines the lag time and is plotted in fig. 8.4b as function of temperature. This lag time decreases linearly with temperature besides in the temperature region of the main phase transition of the lipid membrane, where the lag time shows a local maximum. An overlay of a linear fit to the other data points and C_p indicates high correlation of the maximum in lag time and the phase transition. Thus, besides the kink in rate as function of temperature and the local rate minimum another distinctive feature at T_M was observed. To compare lag time with catalytic rate, the inverse of the lag time is plotted in fig. 8.5. The correlation of the two observables is striking.

8.5. Discussion

The discussion consists of two parts. Because of the correlation of catalytic rate and inverse lag time, the origin of the latter is discussed in the first part. In the second part the main question about the correlation of the systems state of phase and the catalytic rate is answered by the consideration of possible scenarios. The significance of the measured effects is confirmed by the exclusion of various systematic errors, as shown explicitly in the appendix D.3.

8.5.1. Lag time as measure of reaction rate

Because of the striking correlation of rate and inverse lag time, shown in fig. 8.5 the origin of this lag time is discussed in this paragraph. In general the appearance of a lag time is well known for phospholipase A_2 [104]. In this publication Burack and Biltonen study the correlation of lipid bilayer microheterogeneities and modulation of phospholipase A_2 (PLA2) activity in detail. The reported problematic may not be directly conferrable on the experiments studied here, because in the case of PLA2 the vesicles are at the same time substrate of the reaction. But the considerations about the origin of the lag time can serve as starting point.

They hypothesize that the bound-inactive state is a complex of reaction products and PLA2. Because of local product inhibition and substrate depletion the enzyme then shows only low activity. They reason the abrupt increase of reaction rate with phase separation after a certain threshold of product is reached. In these experiments the length of the lag time decreases with

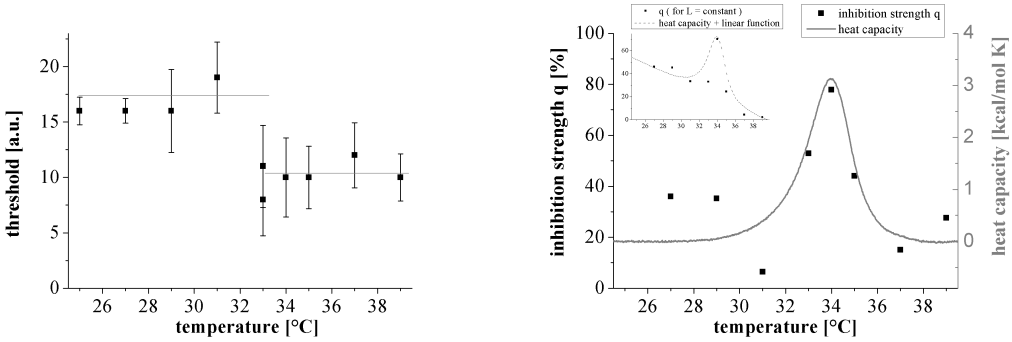

(a) Measured threshold L (b) Inhibition strength q

Figure 8.6.: (a) The intensity threshold L is nearly constant within each phase of the membrane. The error bars are the mean intensity artefact (2.9%) caused by the fluorescence lamp. **(b)** The inhibition strength q during the initial part of the kinetic curve, calculated from eq. 8.1 and the values from fig. a, show a maximum at the phase transition. Inset: Using the mean value of L, the temperature dependence of q fits a superposition of a linear function and the excess heat capacity.

increasing product concentration and goes down to zero for concentrations of 8% and higher. The third important observation in PLA2 experiments - a initial rapid but comparatively small increase of reaction product previous to the lag period - can be seen in the cleavage of VWF, too. However, a fraction of this initial increase is presumably a device related artifact, what similar effects in interrupted kinetic curves suggest.
In contrast to the lipid products there, in the case of ADAMTS13 and VWF the products (fractions of VWF) are water soluble. But, as been shown before in chapter 6 and [64], VWF tends to adhere to lipid surfaces. So the argument that reaction products in the vicinity of the enzyme could lead to a local inhibition until phase separation occurs is conferrable and a possible explanation for the lag time. Assuming that this local inhibition slows down the rate $r*$ for a fix percentage q, the proportionality of maximal rate r and inverse lag time is in agreement with a certain threshold L that has to be overcome to start phase separation and thus a rapid increase of the rate. Eq. 8.1 shows the proportionality of τ and $\frac{1}{r}$ at first glance.

$$\tau = \frac{L}{r*} = \frac{L}{r\,(1-q)} \sim \frac{1}{r} \tag{8.1}$$

This threshhold would lead to a small increase in fluorescence intensity, that can be seen in some but not all kinetic curves clearly. As enzyme-free measurements show that bleeching of the used dye happens on the same scale, the competition of these two opposite effects can be an explanation. In figure 8.5b the threshold L is plotted as function of temperature.

Within the gel/fluid phase L is nearly constant 17 respectively 10 (same units as the the rate in fig. 8.3). Using eq. 8.1 and the measured values of L the inhibition strength q is calculated (eq. 8.2) and plotted in fig 8.6b.

$$q = 1 - \frac{L\tau^{-1}}{r} \tag{8.2}$$

The tendency fits well with a superposition of a linear function and the excess heat capacity. This surprising inhibition maximum is at first glance a contradiction to theory and measurements of AChE [101], that predicts enhancement of the catalytic reaction during the phase transition. As the measured rate from fig. 8.3 was used in the calculation of q, intentionally just a decrease of q with increasing temperature would have been expected. This and the the local minima of the rate at T_M, instead of the expected maximum in analogy to the monolayer experiments, is discussed in section 8.5.2.
However, there remains the question, why reaction product should cause a local inhibition but not the uncleaved substrate. Burack et al. argue that the theory of phase separation is supported by a double peak in the heat capacity profile of the PLA2 samples [104]. In our case a phase separation between fractions of the membrane with and without bound reaction product cannot be proven.
Another reason for the existence of the lag time could be an association of the enzyme to the membrane. Burack showed for PLA_2 that the burst in reaction rate is not simply caused by the adhesion of enzyme to the vesicles [104]. In the experiments discussed here there are several facts that also exclude this explanation. First, monolayer experiments show that the time scale for pressure increases after enzyme addition takes place on the time scale of one to two minutes for several concentrations. Never time scales of 25 minutes were observed. Furthermore the preparation process in our sample is identical but the lag time does not follow just a simple temperature correlated tendency.
To sum up, it has been shown clearly so far that a certain threshold of reaction product has to be overcome before the maximal rate is reached. A model of local inhibition may explain that effect, but is hard to prove. Furthermore, there are enormous systematic differences between the ADAMTS13 measurements here and PLA_2 measurements: besides the structural differences between the enzymes, in our case the originally water soluble enyzem is bound to the membrane with a his-tag and the vesicles themselves are not the substrate of the reaction. Also the measuring technique itself is different. These facts imply that there has to be a more essential reason for the appearance of the lag time. Anyway, this question cannot be answered at the moment, but the lag time may provide an alternative method for the determination of enzyme activity, that needs less experimental time and opens possibilities for simpler and less pricey applications for medical purposes.

8.5.2. Comparison of measurements and theory

At first glance, the presented temperature dependence of the catalytic rate seems to deviate clearly from the theory, which predicts a local maximum in catalytic rate around the phase transition temperature. But the rate shows only a kink, or even a local minimum around the transition temperature. To unravel these contradictions, possible explanations are discussed in the following. Both possibilities are based on the idea, that during the reaction the membrane is de facto not at the point of the phase transition because of the ongoing reaction itself. First, released protons due to the catalytic reaction could force the according vesicles into the gel-like phase. Second, reaction product could change (locally) the state of the membrane and retard the phase transition.
During the reaction protonation of the vesicle, or at least the outer layer of a vesicle, can occur. This local protonation of the bilayer has the same effects like cooling of the particular bilayer. Thus, the lipid membrane is shifted towards the gel phase during the reaction. Hence the reaction is slowed down, resulting in an apparent minimum of enzyme activity. If this is correct, eventually at higher temperatures a rate maximum would be expected. The strength of this effect also depends on the amount of protons produced during the reaction. Intense studies of changes in bulk pH during the reaction show that no significant changes appear, that would lead to a global shift of the phase transition. A measurement of the local degree of protonation for MLV experiments is so far not possible. But this possibility also can not be excluded. Experiments with giant uni lamellar vesicles (GUV) with an fluorescence microscope could allow the observation of the vesicles during the reaction. Due to the significant morphology changes during the phase transition, such experiments are an promising candidate to testify the hypothesis of protonation effects.
A second possible explanation of the not present maximum in rate around T_M is connected with the consideration concerning the lag time before. If reaction product (fragments of VWF) sticks to the vesicle and interact in a manner like stretched VWF (compare the studies in chapter 6) the phase transition can be altered locally drastically. To check this possibility, long time DSC measurements on sample were recorded while the catalytic reaction was running. Figure 8.7a show a series of upscans during a running reaction. Obviously a shoulder at higher temperatures develops on cost of the initial peak around 34°C.

The time scale of this measured effect seems to be an order of magnitude higher than the analyzed part of the kinetic curves. But one should keep in mind that these measurements show the overall heat capacity of the complete sample volume, including also the inner layers of the MLV. Long before the change gets visible in C_p, the phase transition behavior locally in vicinity of

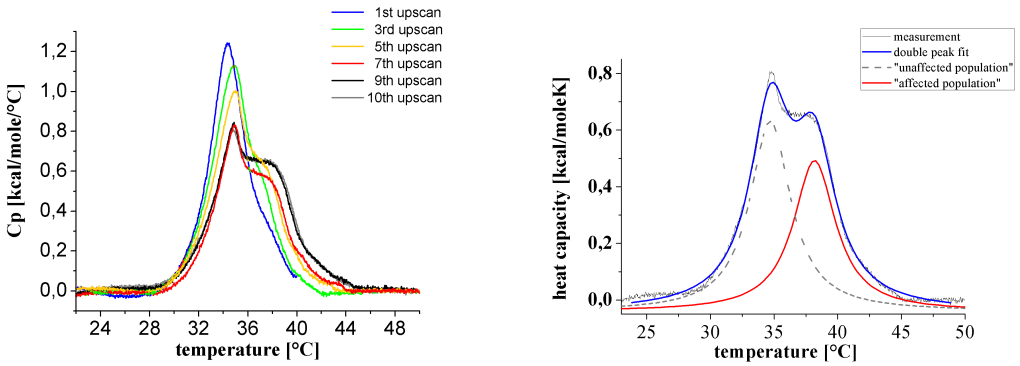

(a) Heat capacity during a running reaction (b) Development of a double peak structure

Figure 8.7.: (a) The heat capacity profile of a typical sample two to 44 hours after start of the reaction. A shoulder developes at higher temperatures. Between the start of each upscan there is a time difference of ca. 4h. **(b)** The heat capacity profile can be fitted with a double peak structure. The two peaks can be attributed to an unaffected population (inside the MLVs) and an affected population (outer bilayers interacting with reaction product).

the enzyme may be altered already. Taking this effect of the reaction product on the membrane phase transition into account, three scenarios have to be compared:

- 1. Membrane unaffected by reaction product. $T_M = 34°C$.
- 2. Membrane affected by reaction product. The thermodynamic properties of the complete amount of lipid influences the catalytic reaction. Broad transition between 30°C and 44°C.
- 3. A fraction of the lipid population affected by reaction product. Mainly the properties of this population influence the catalytic reaction. $T_M \approx 38°C$.

To check which scenario provides best agreement with the measured catalytic rates in fig. 8.8 the rate of samples without enzyme (linear fit, black line) is superposed with C_p(T) for each scenario (gray dashed line), in analogy to fig. 8.2.

Besides the fluctuations, due to the phase state, in literature one finds the opinion, that the fluidity of the membrane is deciding for the activity of membrane associated enzymes [105, 106]. To follow up this explanation attempt, furthermore the activity of the vesicle-free samples is scaled with the excess enthalpy ΔH(T) (red dotted line). In this case the enthalpy serves as a measure of membrane fluidity as it is proportional to the probability that an enzyme is bound to a fluid part of the membrane. The first scenario shows no correlation of neither C_p(T) nor ΔH(T) with the catalytic rate. In contrast, in the second scenario ΔH produces a kink in the temperature dependence, but at too low temperatures. C_p(T) is not correlated with the measured rate, because the predicted increase takes place at too low temperatures and furthermore the rate is predicted roughly constant between 34°C and 39°C. The best agreement of predicted and measured rate appears in scenario 3. The correlation of ΔH(T) and r_0 is convincing: a kink around 34°C is reproduced without other deviations in the measured range. Whereas C_p predicts the increase at 34°C roughly but also a decrease around 39°C, which was not measured.
Thus, we suggest scenario 3 to be the most likely. But the measurements so far do not allow definitely to decide if the rate correlates with C_p or ΔH(T), respectively the fluctuations or the fluidity of the membrane.

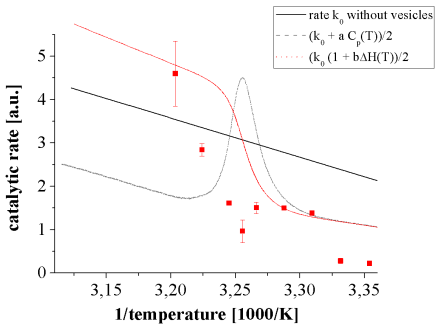

(a) scenario 1

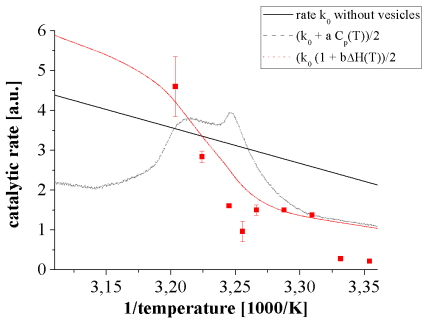

(b) scenario 2

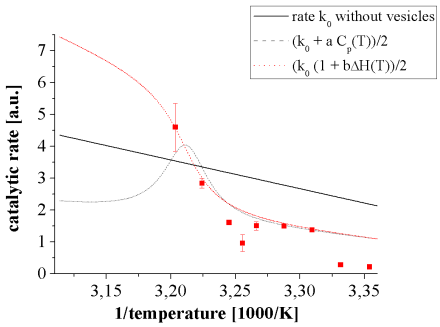

(c) scenario 3

Figure 8.8.: (a) Scenario 1: Neither C_p(T) nor ΔH(T) correlate with the catalytic rate. **(b)** Scenario 2: C_p(T) shows no high correlation, because predicted rate increase takes place at too low temperatures. ΔH produces a kink in temperature dependence but at too low temperatures. **(c)** Scenario 3: Correlation of C_p and rate but predicted decrease around 39°C was not measured. ΔH(T) shows the best correlation: kink around 34°C reproduced without big deviations.

8.6. Conclusion and Outlook

Thus, the measurements suggest that the affected lipid population in turn influences the enzyme and hence the measured rate. One can only suppose, whether this changes in the affected population happen due to interaction with the VWF fragments themselves, the dyes associated with these fragments or due to other effects like protonation during the reaction. The catalytic rate correlates in these measurements with the excess enthalpy and hence with the fraction of fluid parts in the membrane as well with the heat capacity and the membrane fluctuations.
Measurements at higher temperatures between 45°C and 50°C could approve the above mentioned conclusions. But besides the problematic to reach these temperatures with the used plate readers, these temperatures could lead to denaturation of the enzyme and to temperature induced cleavage of the substrate. Thus, analogous experiments performed with 14:0PC and 18:1DGS-NTA(Ni) are a promising way to further illuminate the question of the role of membrane fluctuations for the activity of membrane associated enzymes. Furthermore a system with a more narrow phase transition (e.g. possible by decreased fraction of 18:1DGS-NTA(Ni)) would be in turn correlated with stronger fluctuations and hence a better chance to detect the influence of the fluctuations also in bilayer vesicle systems.
However, the presented data show clearly that the activity of a membrane bound enzyme is strongly coupled with the state of the membrane. In the case of ADAMTS13 this is even more surprising, as the enzyme naturally is water soluble and not linked to the membrane. In nature the cleavage of VWF mainly happens when the protein is in its elongated conformation and these elongated VWF fibers stick to the vessel walls. Thus, the question raises, whether the membrane state dependent activity of the enzyme could be self regulated by the interaction of VWF, membrane and enzyme. One could imagine the following thought experiment, illustrated in figure 8.9.
A phase transition of biological cell membranes is found to be often at temperatures slightly below the temperature of the organism [107]. We have shown before that elongated VWF interacts much more with lipid interfaces than globular VWF. If elongated VWF fibers are now adhered to the cell membranes of the vessel walls the phase state of the new system is changed. In the experiments above the phase transition temperature has been increased for several degrees. As the temperature in mammalian organisms stays almost constant, locally the membrane-VWF-complex is more close to the phase transition than the bare membrane. Increased fluctuations of thermodynamic variables are the consequence. If it turns out, that indeed the fluctuations

dictate the enzyme activity, an increased cleavage of VWF is predicted. On the other hand if the fluidity of the membrane regulates the enzyme activity, the influence of VWF on the state of phase would lead to a decrease of enzyme activity and thus a stabilization of the VWF fibers and the whole wound closure. Obviously this topic stays a highly interesting field of research at the intersection of biology and physics.

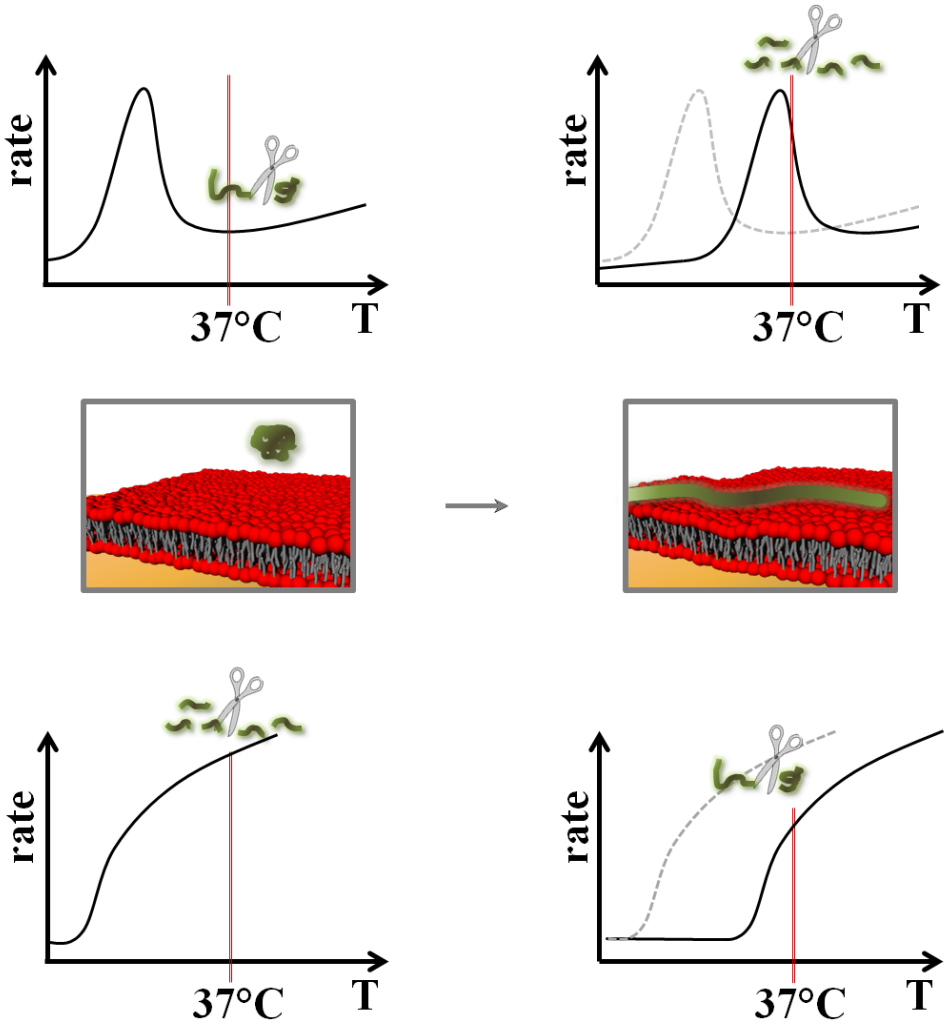

Figure 8.9.: Illustration of self regulation by interaction of VWF, membrane and ADAMTS13: Due to the adhesion of VWF to the membrane the phase transition is shifted. **top scenario:** if the enzyme activity is proportional to the area fluctuations, increased cleavage of VWF is predicted. **bottom scenario:** if the activity is proportional to the fluidity of the membrane, a decrease of the reaction rate is predicted.

Part III.

Appendix

A. Appendix - Mutations influence mechanical stretching of VWF

A.1. Typical cantilever and substrate preparation protocol

Ethanolamine layer

- Take a fresh PBS++ bottle and adjust the pH value to 7.4
- 24.75 g Ethanolamine Hydrochloride in 45 ml DMSO (Dimethylsulfoxide)
- Clean a glass beaker (diameter about 9 cm) with EtOH and ultrapure H_2O
- Add 45 ml of the DMSO inside the beaker and 24,75 g Ethanolamine. Cover the beaker to avoid evaporation.
- Put the beaker on the hot plate at $60°C$ and stir the Ethanolamine to dissolve it completely.
- After solution of the Ethanolamine, add the molecular sieve and put the beaker in the vacuum chamber, for removing the air bubbles.
- Clean a halved Micaslide with chloroform. Put chloroform in three big enough glasses. The slide has to be cleaned for 5 minutes in each of the 3 glasses. Cover the glasses!
- Blast the slide with a very mild Nitrogen blast.
- Put the clean Micaslide and the cantilevers inside the beaker, on the molecular sieve layer. The slide and the cantilevers incubate overnight.
- Washing: Pour DMSO in 3 beakers. The cantilevers and slides should be cleaned in each beaker for five minutes. Blast the washed slide and cantilevers with nitrogen. Repeat the cleaning steps with ethanol.

Linker molecules: Aldehyde-PEG-NHS

- Open the package of the aldehyde-PEG-NHS which is ordered by Linz (Institut für Biophysik J.K Universität Linz, 4040, Linz). Open it under the hood, since it can be packed under toxic atmosphere.
- Add 0.5 ml of chloroform to 3.3 mg the aldehyde-PEG-NHS (package), for solving the aldehyde-PEG-NHS. Add 10 μl Triethylamine and put the half of the mixture in the middle of the coating area. Use the middle of the slides as coating area, scratch a little R in the top right corner. Incubate the system and the cantilevers at RT for two hours. During the time of working with the mixture of aldehyde+chloroform, cover the glass beaker to avoid chloroform evaporation.
- Take the VWF out of the freezer, ideally thaw it at $37°C$ and dilute to the desired concentration.

Substrate coating with VWF antibodies and cantilever coating with VWF

- Wash the slides and the cantilevers with chloroform (3 step system), then dry them with N2 blast.
- Take 30 μl VWF antibodies (Dako Cytomation, Denmark, A0082, 3.1mg/ml) and dilute it with 270 μl pure water. Put the diluted antibody solution onto the coating area of the slide and let it incubate for two hours in the fridge.
- Put for each cantilever a drop of the VWF dilutions on a cleaned teflon plate and stick the tips of the cantilevers in the drop(s) and let it incubate for two hours in the fridge.
- Prepare a Hydroxylamine solution (0,34745 g / 10 ml, pH = 7.4) and put the slides and the cantilevers in the Hydroxylamine solution for 60 min (or put the Hydroxylamine solution onto the coating area).
- Wash the slides and cantilevers in PBS++ three times for 5 minutes.
- Store slides and cantilevers in PBS++ in the fridge.

A.2. Parameters - force spectroscopy, simulation, resulting fit parameters

Default force spectroscopy parameters

In standardized force spectroscopy experiments the crucial parameters were kept constant. Thus, there are default values for the trace velocity (1μm/s), the retrace velocity (250nm/s), pause at substrate (1s) and the contact force during the pause at substrate (500pN). Due to the choice of cantilevers with spring constants in the same range and the fixed retraction velocity, loading rates in compared experiments varied between 3400pN/s and 9500pN/s. As the forces depend logarithmically on the loading rates systematic errors are estimated to be in the range below 10%.

Simulation parameters

In parallel N polymers were simulated. A polymer consists of a linker to the cantilever, M protein building blocks and a linker to the substrate. If not other explicitly mentioned M = 4 and N = 3. The simulation parameters of the three subunits of a polymer were the following (attaching and folding was not implemented).
Protein building block: contour length of domains in m: 1E-9*[105, 6, 10], persistence length of domains 100 nm, typical force for unfolding 7 pN, basic rate for unfolding 0.2, typical force for detaching 10 pN, basic rate for detaching 10, ground state: folded.
Linker to cantilever: contour length of domains 15 nm, persistence length of domains 0.5 nm, typical force for unfolding 1 pN, basic rate for unfolding 1, typical force for detaching 200 pN, basic rate for detaching 0, ground state: folded.
Linker to substrate: contour length of domains 15nm, persistence length of domains 0.5 nm, typical force for unfolding 1 pN, basic rate for unfolding 1, typical force for detaching 10 pN, basic rate for detaching 0.4, ground state: unfolded.

A.3. Force clamp measurements on VWF WT

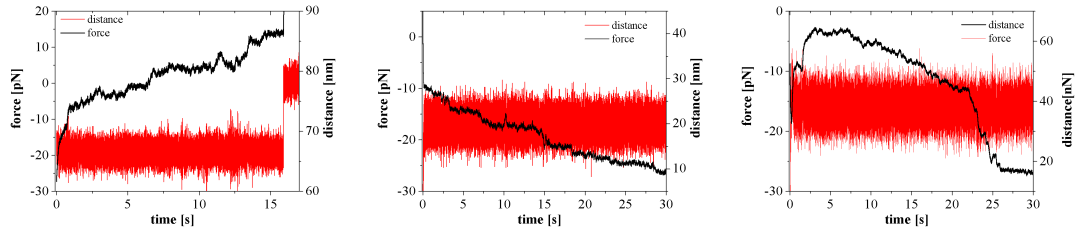

(a) Unfolding and Folding

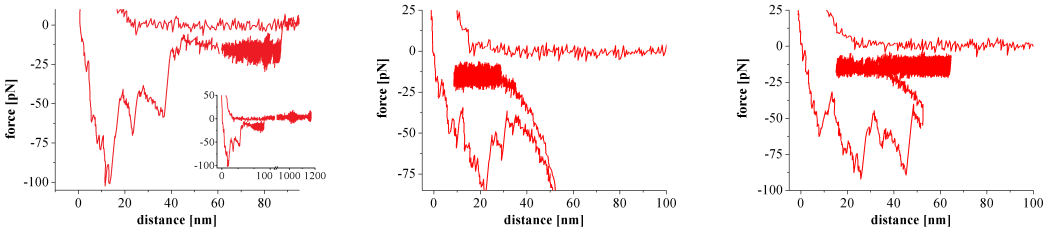

(b) F(d)

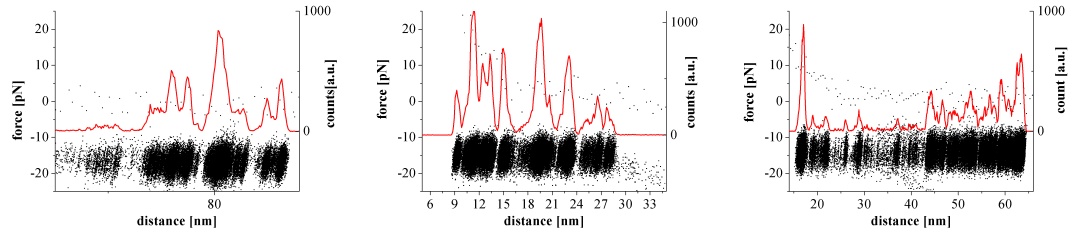

(c) State histograms

Figure A.1.: (a) Typical clamp measurements on VWF WT. During retraction of a standard force distance cycle the force is clamped at 20pN (red line) after a initial retrace of ca. 50 nm. The distance between tip and substrate is observed as function of time (black line). Left: Protein unfolding is indicated by the upward steps, until the bond breaks at t = 16 s and the force drops to zero. Center: the protein folds as indicated by the downward steps. Right: the protein unfolds in the first 3 s before it refolds again from t = 8 s till t = 25 s.**(b)** The data from the plots above plotted as F(d). Inset: Complete force curve up to a distance of 1100 nm. **(c)** Zoom into the regions of the force clamp (black dots). Histograms of the distance with a bin size of 0.1 nm give insight about the dwell times of each state, respectively position.

Fig. A.1 shows representative examples of force clamp measurements on VWF WT. The typical plotting variant is chosen for the graphs in the first line. They show the end-to-end-distance of the protein as function of time, while the force

is clamped to ≈20 pN. Unfolding, Folding as well as both can be seen in the measurements. The second line shows besides the clamp phase also the trace and initial retrace, plotted as force distance curve. The accumulation of data points is an indication for long times at the particular points. Finally, the third line is a zoom into the relevant part during the force clamp phase (black dots). Additionally histograms of the measured end-to-end lengths are plotted. The quantization of the end-to-end distances is originated by different states of the protein. Further considerations, using statistical physics, can give further information e.g. about transition probabilities and are an interesting point to continue the research in this field.

B. Appendix - Conformation of von Willebrand Factor switches interaction with phospholipid membranes

B.1. Measurements - time dependence, quantification of hysteresis, temperature dependence of phase transition

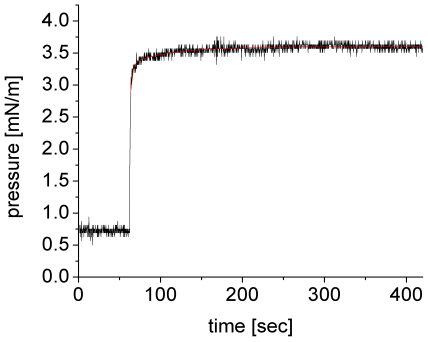

Figure B.1.: At fixed area a VWF droplet is spread at the surface, while the lateral pressure is recorded as function of time. A rapid increase and a stable saturation indicate, that a fraction of the proteins goes to the surface and interact with the lipids or repels them.

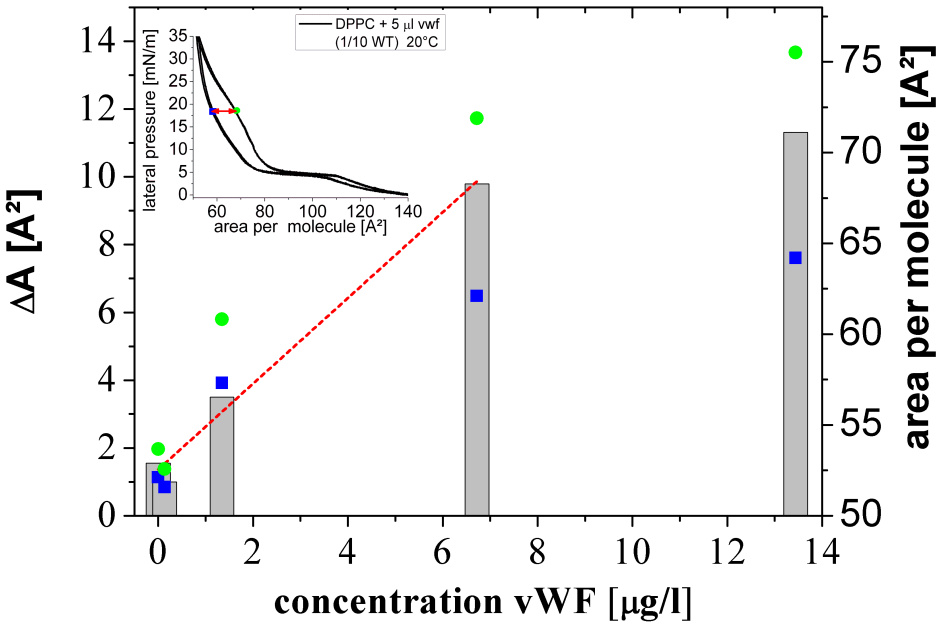

Figure B.2.: Quantification of the hysteresis. The maximal difference between compression and expansion isotherm plotted as function of VWF concentration. The hysteresis is a linear function below 7 μg/ml. For higher concentration the hysteresis shows a saturarion behavior.

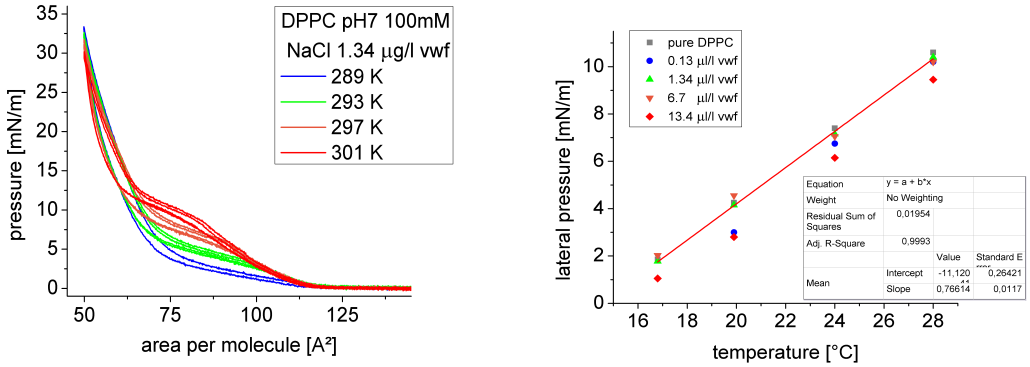

(a) DPPC isotherms in presence of VWF at different temperatures

(b) Lateral pressure of the phase transition as function of temperature

Figure B.3.: (a) The area-pressure isotherms of a DPPC monolayer for a fix VWF concentration show an increase of the phase transition pressure. **(b)** The phase transition pressure for each concentration shifts linearly with increasing temperature. The mean value over different concentrations for this increase is $\frac{0.8mN/m}{1/K}$.

B.2. Compressibility in measurements and calculations

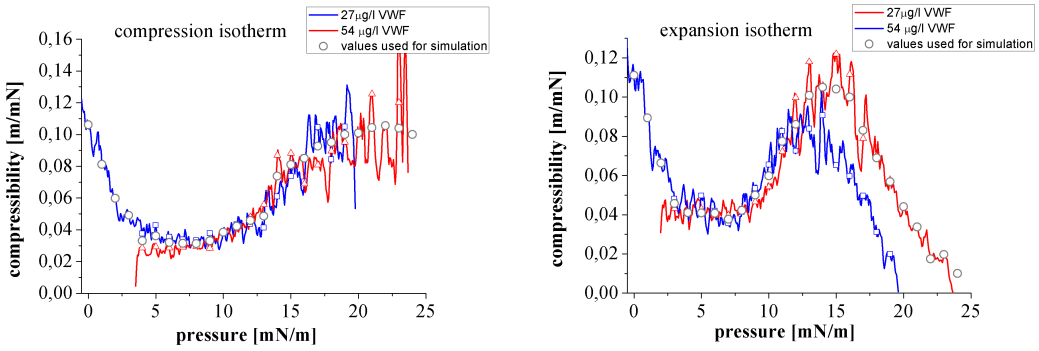

(a) Compression compressibility (b) Expansion compressibility

Figure B.4.: (a) Compressibility of pure VWF layer compressions. To cover a adequate pressure range isotherms at different concentrations were measured and the compressibilities were combined. The circles are the used values for the calculated isotherms. **(b)** Compressibility of pure VWF layer expansions. Independent from exact pressure, a barrier opening results in a steep pressure decrease. As pressures over 30 mN/m are reached in the VWF DPPC monolayers, for the calculations the compressibilities of the higher concentrated samples were used.

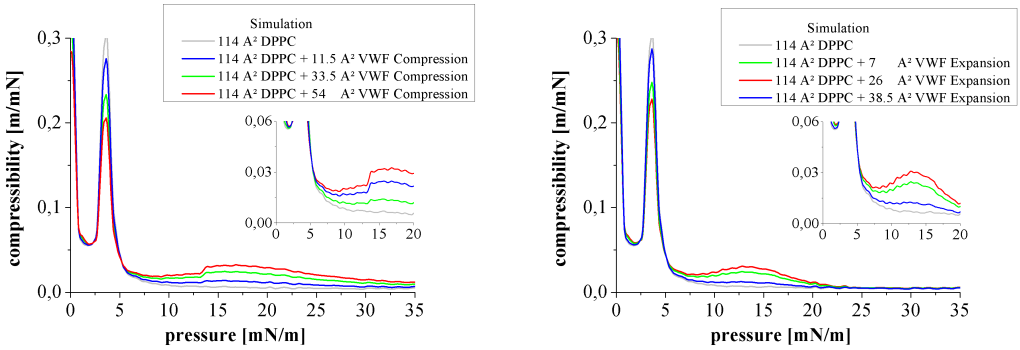

(a) Calculated compression compressibility (b) Calculated expansion compressibility

Figure B.5.: (a) Compressibility of simulated VWF-DPPC compressions with different amounts of VWF. **(b)**Compressibility of simulated VWF-DPPC expansions with different amounts of VWF.

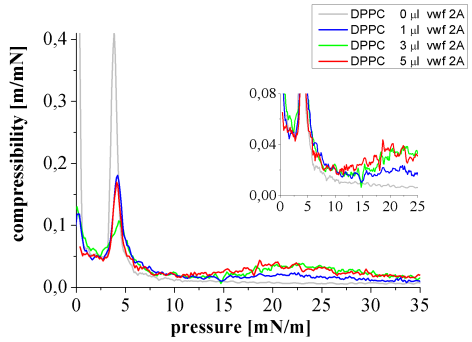

(a) Compression compressibility - VWF 2A

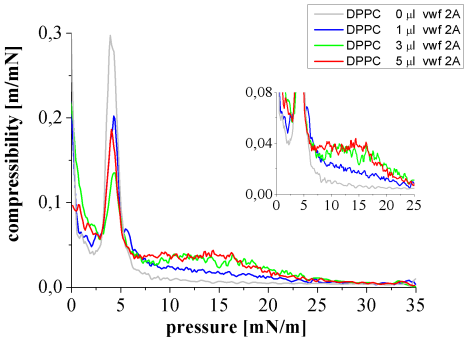

(b) Expansion compressibility - VWF 2A

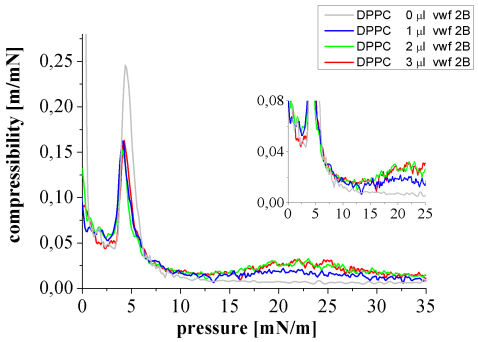

(c) Compression compressibility - VWF 2B

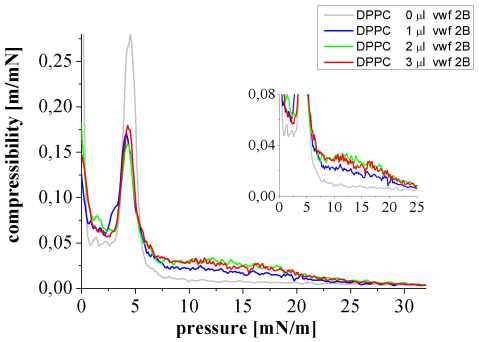

(d) Expansion compressibility - VWF 2B

Figure B.6.: Compressibility as function of concentration of **(a)** compression 2A **(b)** expansion 2A **(c)** compression 2B **(d)** expansion 2B. The maximal compressibility at the phase transition is decreased. Similar to VWF WT, the mutated VWF causes an additional broad peak between 15 mN/m and 25 mN/m for the compression curves. In the compressibility from the expansion curves a shoulder occurs between 5 mN/m and 20 mN/m.

C. Appendix - Impact of nanoparticles on phospholipid membranes

C.1. Additional information to SSV experiments

How much lipid covers the nanoparticles? As shown in chapter 7 SSV samples were prepared and the impact of the NP to the phase transition behavior of the lipid membranes was studied. To determine the amount of lipid associated with the NP samples were centrifuged to remove NP-free vesicles. The NP and lipid containing sediment was analyzed with thermogravimetrical analysis (TGA). The samples were heated with a controlled temperature ramp while the weight is measured with high precision. Thus the fraction of organic constituents can be measured. Fig. C.1 shows the results of a typical NP containing DPPC sample and of the reference measurement - a pure NP sample. From the weight loss the amount of lipid is calculated. Using the molecular weight of the lipid, a typical area per lipid head group delivers the theoretical area, the lipids could cover if arranged as a bilayer.
Furthermore from the weight and known size of the NP their surface area (under assumption of plain spheres) is calculated. The resulting area ratio of lipid and NP lies in the range of 48% to 98%. The upper and lower limit of this range result from the variation of area per lipid between $55A^2$ and $90A^2$ (typical values for liquid condensed/expanded phase) and the variation of NP size within the range of the standard deviation around the mean diameter. This result agrees with the assumption that each NP is (partly) covered by one lipid bilayer.

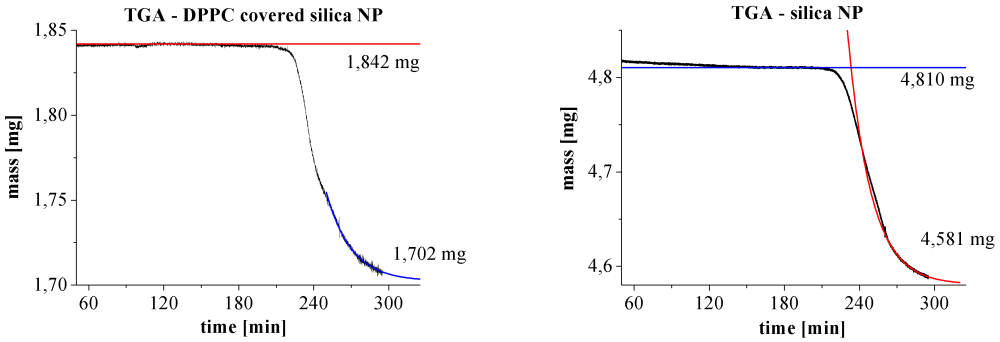

Figure C.1.: Thermogravimetry: During heating the mass of a sample is recorded as function of time with high precision. **(a)** After DSC measurement a NP containing DPPC sample was centrifuged and the supernatant was discarded. The remaining part of the sample was analyzed with TGA. **(b)** In an analog experiment the mass ratio of hydrated and dry NP is determined.

How do the free parameters of the fit to ΔT influence each other? The fitting parameters of the mentioned three parameter fits in section 7.3.4 are shown in fig.C.2.

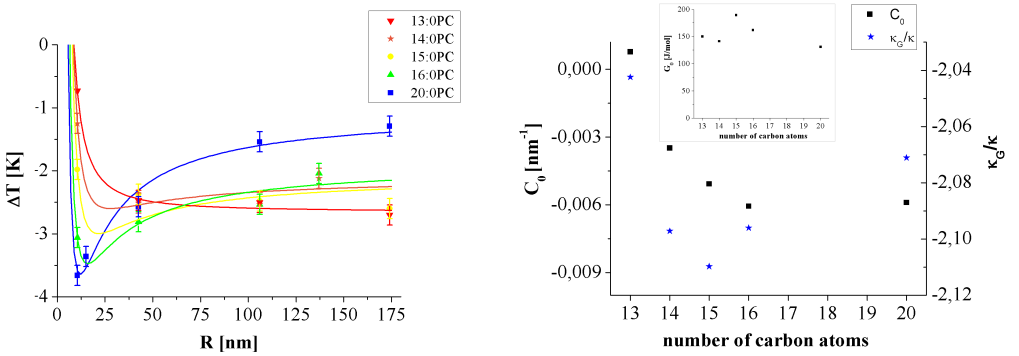

(a) Three-parameter fit to ΔT (b) Results of the three-parameter fit to ΔT

Figure C.2.: (a) Three-parameter fit to ΔT shows very good agreement with the measurements. **(b)** Results of the three-parameter fit to ΔT: c_0, ΔG_S and z.

C.2. Preparation protocol for GUV

Giant unilamellar vesicles were produced by the electro swelling method [108]. Lipids with the intended concentration ratio (ca. 2 mg/ml) were solved in a

chloroform and methanol mixture (95:5). This solution is transfered to an ITO covered glass substrate. After evaporation of the solvents, two of the plates are combined with a TEFLON frame to a closed chamber. In a heat bath with a temperature higher than T_M a sinusoidal voltage is applied to the plates (3V, 10Hz). This accelerates the formation of single bilayers that form closed unilamellar vesicles in the size range of (10-100) μm.
Materials:

- DPPC solved in chloroform (*Avanti Polar Lipids Inc., USA*)
- fluorescence dye *Texas-Red-DHPE or DiD (Invitrogen, USA)*
- saccharose from *Merck, D.*

Processing steps:

1. ITO plates are cleaned with isopropanol and mucasol-solution in an ultrasonic bath. Subsequently the plates were cleaned with vibes and isopropanol and water. Finally the plates are rinsed with water and dried under nitrogen flow.
2. Mixing of lipid and dye in intended molar ratio in the chloroform methanol mixture.
3. ITO plates are warmed on a heat plate above T_M.
4. Roughly 8 μl of lipid solution are distributed over each plate with a needle.
5. Evaporation of solvents under vacuum for 3 h.
6. Two plates are bonded to a frame. These chambers are filled with saccharose-solution (degased, $\approx$ 200 mM) through a hole that is closed with polysiloxane afterwards. A sinusoidal voltage is applied to the ITO covered plates: (15 Hz, 2.3 V).
7. The temperature of the chamber is kept for 6 h - 18 h slightly above T_M.
8. To detach adhered vesicles from the plate a square-wave voltage (4.5 V) can be used at the end of the swelling process.
9. Use only pipettes with big opening for handling of the GUV dispersion to avoid high shear forces.
10. The GUV are stable at $4°C$ for some days.
11. For microscopical observation it is helpful to bring the GUV in glucose solution. Because of the higher density the vesicles sink down and lie on the glass slide. The osmolarity of both solutions has to be exact the same.

D. Appendix - Membrane state regulates enzyme acitvity

D.1. Thermodynamic studies of NTA-lipid phosphodylcholine mixtures

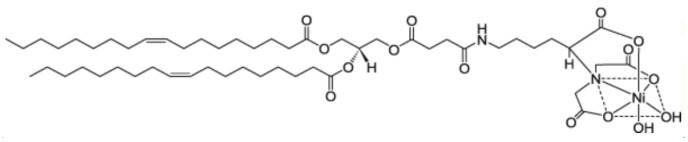

Figure D.1.: Chemical structure of 1,2-dioleoyl-sn-glycero-3-[(N-(5-amino-1-carboxypentyl)iminodiacetic acid)succinyl] (nickel salt). Short name: 18:1DGS-NTA(Ni).

The strategy to bind histidin-tagged biomolecules to chelator lipids - or more specific: 1,2-dioleoyl-sn-glycero-3-[(N-(5-amino-1-carboxypentyl)iminodiacetic acid)succinyl] (nickel salt) (NTA-lipid) - has been shown to be a highly defined way to immobilize proteins to lipid surfaces [109]. The Ni atom in the head group is exchanged with the histidin-tag of the enzyme. In the experiments presented in chapter 8 this strategy is used to measure the activity of a per se water soluble enzyme when it is bound to a lipid membrane. To understand the impact of the NTA-lipid on the studied phosphodylcholine mono- and bilayers, its influence on the most meaningful thermodynamic variables is studied.

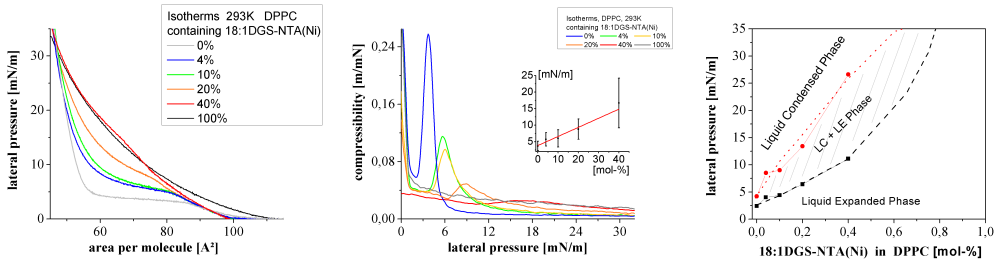

(a) Isotherms of lipid mixture (b) Lateral compressibilities (c) Phase diagram

Figure D.2.: (a) Isotherms of a mixture of DPPC and 18:1DGS-NTA(Ni) at 293K. Increasing the percentage of 18:1DGS-NTA(Ni) leads to a decrease in phase transition pressure. Similarities to an assembly of pure DPPC isotherms of different temperatures is obvious. **(b)** Compressibilty of isotherms in figure (a). **(c)** Estimated phase diagram of a mixture of DPPC and 18:1DGS-NTA(Ni) for 293K. Dotted/dashed lines indicate the estimated phase boundaries. Circles/Squares indicate borders of the coexistence region of liquid condensed and liquid expanded phase.

Lateral compressibility of NTA-lipid containing 16:0PC monolayers In fig. D.2a isotherms of DPPC monolayers containing 2% to 100% 18:1 DGS-NTA(Ni) are shown. This assembly of area-pressure isotherms, for a fixed temperature but varying ratio of lipid contents, demonstrates that the chemical potential acts as a thermodynamic force, like temperature.

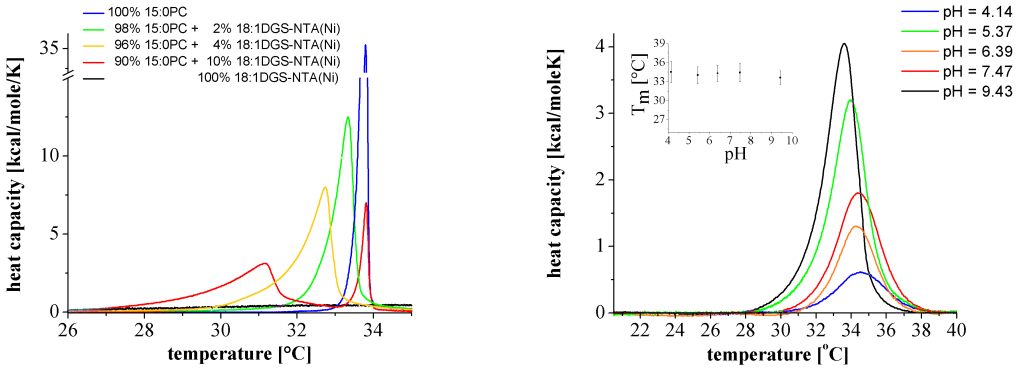

(a) Heat capacity of lipid mixtures

(b) pH dependent heat capacity

Figure D.3.: (a) Heat capacity of mixtures of 15:0PC and 18:1DGS-NTA(Ni). Increasing the percentage of 18:1DGS-NTA(Ni) leads to a decrease in phase transition temperature and a broadening of the transition. The two peaks at a fraction of 10% 18:1DGS-NTA(Ni) indicates phase separation and independent melting of both components. **(b)** The heat capacity profile of a sample under same conditions as experiments reported in 8 for varied pH. Error bars indicate temperatures with half of the maximal heat capacity. As no charged lipids are used, the T_M is only weakly dependent on the pH over a broad range. The shift compared to the samples of figure (a) are caused by DMSO content of the substrate solution.

Heat capacity of NTA-lipid containing 15:0PC vesicles To study the activity of membrane-bound ADAMTS13 in chapter 8 vesicle experiments are shown. The main constituent of a cell membrane is a lipid bilayer. So lipid vesicles are a simple model system to study the enzyme activity in aqueous solution. As the question of interest is the dependency of the enzyme activity on the physical state of the membrane, one has to have an idea about the multi dimensional state diagram of the lipid system. The axes of this phase space are e.g. temperature, ratio of lipid mixture (connected with the chemical potential), pH, three dimensional bulk pressure and so on.
The parameters that influence the physical state of a lipid bilayer easily; besides the temperature; are the chemical potential and - mostly for charged lipids - pH. Figure D.3 shows the heat capacity as function of temperature for different vesicle samples. In figure D.3a the fraction of 18:1DGS-NTA(Ni) is varied, while figure D.3b shows the heat capactiy of a 98%DPPC-2%18:1DGS-NTA(Ni) sample for different pH values. The inset in this figure shows T_M as function of pH, where error bars indicate the temperatures, where C_p is decreased to half of the maximal heat capacity. Increasing the pH from 4 to 9 causes a slight decrease of T_M. Compared to the studied temperature range and the transition width the shift is negligible. As expected pH changes influence the temperature driven phase transition only weakly, while the lipid

composition causes stronger effects. Already at a fraction of 10% 18:1DGS-NTA(Ni) lipid phase separation and independent phase transitions appear, as the two separated peaks indicate. Hence, this is a upper limit for the intended experiments on enzyme activity.

D.2. Influence of His-tag on binding affinity

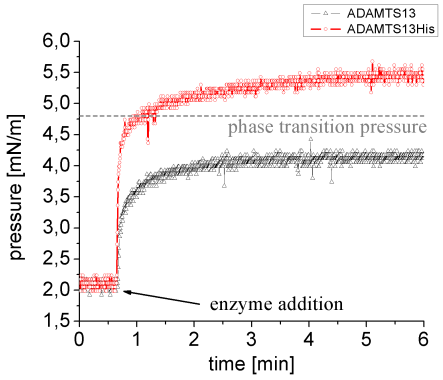

(a) Addition of enzyme to a DPPC monolayer.

Figure D.4.: Same volumes of ADAMTS13 (red circles) and ADAMTS13His (black triangles) were added to a DPPC monolayer in the liquid expanded phase at fixed area. Although the concentration of ADAMTS13His is roughly half the concentration of ADAMTS13 the pressure is even shifted above the phase transition pressure, indicating a stronger binding affinity for the enzyme with the His-tag.

In fig. D.4 the lateral pressure of a monolayer as function of time is plotted. At the point of time indicated with the arrow ADAMTS13 with respecitvely without his-tag is given to the surface. The pressure increase for the enzyme with his-tag is significantly higher than for the enzyme without his-tag. Taking the concentrations into account and assuming the same area compression per enzyme molecule bound to the membrane, the binding affinity is four times higher for ADAMTS13His compared to ADAMTS without his-tag.

D.3. Exclusion of systematic errors - measurements and calculations

To convince the reader of the significance of the results concerning dependency of catalytic rate as function of the membrane state, it is essential to exclude systematic errors of the experiment. Thus, at first the impact of pH on the membrane, fluorescence absorption and geometrical constrainments are discussed.

Influence of pH changes on membrane state

Heat capacity profiles of a typical lipid containing sample at different pH were measured, to ensure that the state of phase of the lipids is not influenced due to possible pH changes that could be caused by protonation during the catalyzed reaction. The results are plotted in fig. D.3b. As no "charged" lipids are used, T_M is only weakly dependent on pH over a broad range. Thus, it can be assumed that the temperature is the main parameter to change the state of the membrane and pH effects can be neglected.

Influence of temperature dependent absorption of vesicle solution on fluorescence signal

Since the enzyme activity is only measured by fluorescence spectroscopy, the temperature dependent absorbance of vesicle solutions has to be checked carefully as possible source of error. In the following it is shown with temperature dependent absorbance measurements in the range of the used wavelengths that the transmittance of buffer is constant. However, the transmittance of vesicle containing buffer with same concentrations as used in the experiments is a function of temperature as can be seen in D.6. Thus, a minor contribution to the increased intensity and thus catalytic rate is caused by the decreasing absorbance with increasing temperature. As the following considerations show, the intensity of the vesicle containing sample should be the intensity of a vesicle free sample multiplied by the square of the transmittance, if the unquenched dye concentrations are equal.

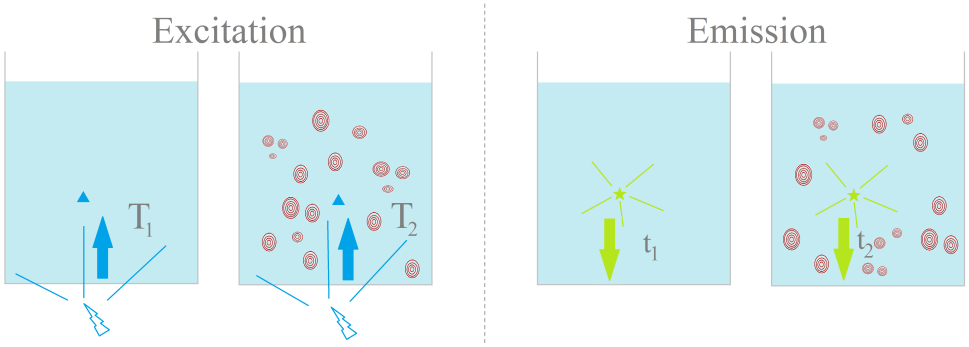

Figure D.5.: Comparison of fluorescence yield in vesicle free and vesicle containing samples. Left: The exciting light that reaches fluorescence molecules is proportional to the transmittance T(485nm) of the sample. Right: the detected light sent out from the fluorescent molecule is proportional to the transmittance t(535nm) of the sample. Assuming nearly equal distribution of dye in the samples, the signal will be approximately proportional to the product $T(485nm) \cdot t(535nm)$.

As indicated on the right side of fig. D.5 from the intensity I of a fluorescent molecule the fraction IT_1 is detected after crossing the vesicle free sample, where $T_1 = T_1(485\,nm) = 1 - A_1(485\,nm)$ is the transmittance of the sample for light with the wavelength 485 nm. The values for the vesicle containing sample are named in analog way using subscript 2. Assuming the same real fluorescence I in both samples the measured intensity of the vesicle containing sample I_2 is expected to be $I_2 = T_2/T_1 I_1$.
In the same manner during the excitation process light is absorbed on its way to the dye. This leads in general to a reduced number of dyes fluorescing in the sample. For light of the exciting wave length (535 nm) t_1 is the transmittance of the vesicle free and t_2 the transmittance of the vesicle containing sample. Hence the measured intensities for j =1, 2 are

$$I_j = ct_j T_j \tag{D.1}$$

with c =constant. Consequently for same amount of fluorescent dyes the expected intensity ratio r is:

$$r := \frac{I_2}{I_1} = \frac{t_2 T_2}{t_1 T_1} \approx \frac{T_2^2}{T_1^2} = \left(\frac{T_2}{T_1}\right)^2 \tag{D.2}$$

Temperature dependent absorbance measurements in the range of 490 nm - 550 nm for buffer and vesicle containing buffer with same concentrations as used in the experiments show that T_2 is constant. However T_1 is slightly a function of temperature as can be seen in fig. D.6. Thus, a minor contribution to the increased intensity and thus catalytic rate is caused by the decreasing absorbance with increasing temperature. As the considerations above show,

the intensity of the vesicle containing sample should be the intensity of the vesicle free sample multiplied by the square of the transmittance.
However scaling the intensity of the vesicle free sample with the square of the transmittance as function of temperature does by far not reproduce the kink in the catalytic rate as function of inverse temperature. Thus, absorption effects can be neglected to the greatest extend.

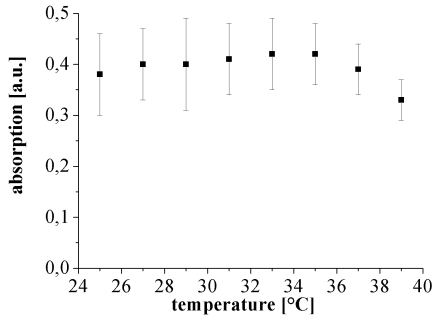

Figure D.6.: (a) Absorption of vesicle containing samples as function of temperature.

Influence on measured fluorescence due to reduced volume

For the experiments separately MLVs were produced and sensor dye and enzyme was diluted in buffer. Roughly five to ten minutes before start of the reaction vesicles and dye were mixed and equilibrated to the designated temperature. Afterwards one to two minutes before start of the measurement the enzyme was added and the solution was shaken for five seconds. Thus, a possible source of error is the reduced reaction volume compared to vesicle free samples. Neither enzyme nor substrate can go to the enclosed volume inside the vesicles (besides the measurements at the phase transition temperature where budding occurs). The following calculations will show that less than 1% of the volume are closed.
The volume V of a spherical MLV with diameter d is $V = 4/3(d/2)^3\pi = \pi/6d^3$. Furthermore the number concentration c_N of MLVs can be estimated from the total lipid concentration c_L, the molar Mass M, the average number of bilayers in a MLV and the average area A of a lipid molecule:

$$c_N = \frac{N_{Lipids}}{n\frac{4\pi d^2}{A^2}} = \frac{\frac{c_L}{M}}{n\frac{2\pi d^2}{A^2}} \tag{D.3}$$

Multiplying the number concentration of MLVs with the occupied volume of one MLV gives the fraction of occupied volume v:

$$v = \frac{Ac_L d}{12Mn} \approx \frac{0.085}{n} \tag{D.4}$$

with the known quantities $c_L = 0.8 mg/ml$, M= 710 g/mole and d=3μm (Hydrodynamic diameter from DLS measurements, not shown). Furthermore A= 0.5 nm^2 is assumed according to literature values [110] for the gel phase. The number of layers in such an onion-like MLV are typically in the order of 10 to 100. Taking the lower limit gives an upper limit for the estimation of occupied volume of 0.85%. Hence it can be assumed that effects due to that reduced volume do also not significantly influence the catalytic rate.

Curriculum Vitae

Personal Data

Christoph Westerhausen

born 1984 February 16th in Dillingen

Education

06/2012	PhD (University of Augsburg)
12/2008	Diploma in physics (University of Augsburg)
12/2008	Exame for teaching of mathematics/physics
06/2003	Abitur (Johann-Michael-Sailer-Gymnasium, Dillingen)

Prior Engagements

03/2011–06/2011	Boston University, research visit, Department of Mechanical Engineering, Boston, MA, USA, Biophysics group, Prof. M. F. Schneider
09/2011–12/2011	Boston University, research visit, Department of Mechanical Engineering, Boston, MA, USA, Biophysics group, Prof. M. F. Schneider
04/2009–03/2012	University of Augsburg, research associate, Lehrstuhl Experimentalphysik I, Biophysics group, Prof. A. Wixforth
09/2010–12/2010	University Hospital Mannheim, research associate, Sektion Experimentelle Dermatologie, Prof. S. W. Schneider
01/2009–03/2009	University of Augsburg, graduate assistant, Lehrstuhl Experimentalphysik I, Biophysics group, Prof. A. Wixforth
04/2008–07/2011	University of Augsburg, teaching assistant for mathematics, Prof. J.H. Eschenburg
09/2007–09/2008	Rudolf-Diesel-Gymnasium, Augsburg, part-time teacher for mathematics
10/2007–12/2007	University of Augsburg, teaching assistant for mathematics in micro economics, Lehrstuhl für Volkswirtschaftslehre mit Schwerpunkt Umwelt- und Ressourcenökonomie, Prof. P. Michaelis
07/2003–12/2007	BSH GmbH, Dillingen, Six Sigma, working student
04/2000–03/2003	Nosta GmbH, Höchstädt, part-time job

Publications and coached diploma theses

- S. Niland, C. Westerhausen, S. W. Schneider, B. Eckes, M. F. Schneider, J. A. Eble, Biofunctionalization of a generic collagenous triple helix with the [alpha]2[beta]1 integrin binding site allows molecular force measurements, The International Journal of Biochemistry and Cell Biology, Volume 43, Issue 5, May 2011, 721-731

- D. Breyer, Mechanik des Bioproteins VWF: Simulation, Experiment und Analyse, Diplomarbeit, Augsburg, Feb. 2011

- F. Strobl, Zur Interaktion von Lipidmembranen und Nanopartikeln, Diplomarbeit, Augsburg, Apr. 2011

- A. T. Bauer, E. Strozyk, C. Gorzelanny, C. Westerhausen, A. Desch, M. F. Schneider, S. W. Schneider, Surface area-dependent Cytotoxicity of Silica Nanoparticles induces Exocytosis of von Willebrand factor and necrotic Cell Death in primary human endothelial Cells, Biomaterials, 2011 Nov;32(33):8385-93. Epub 2011 Aug 16

- C. Westerhausen, F. Strobl, R. Herrmann, A. T. Bauer, S. W. Schneider, A. Reller, A. Wixforth, M. F. Schneider, Chemical and mechanical impact of silica nanoparticles on the phase transition behavior of phospholipid membranes in theory and experiment, Biophys. Journal, 102(5), 1032-1038

June 6, 2012

Bibliography

[1] E Schrödinger. *What is life? The physical aspect of the living cell*. Cambridge University Press, Cambridge, 1948.

[2] S W Schneider, S Nuschele, A Wixforth, C Gorzelanny, A Alexander-Katz, R R Netz, and M F Schneider. Shear-induced unfolding triggers adhesion of von Willebrand factor fibers. *PNAS*, 104(19):7899–7903, 2007.

[3] S D Conner and S L Schmid. Regulated portals of entry into the cell. *Nature*, 422(6927):37–44, 2003.

[4] Matthias F Schneider and Stefan W Schneider. Der von Willebrand-Faktor : Ein intelligenter Gefäßkleber. *Biospektrum*, 14:134–139, 2008.

[5] A J Reininger. Function of von Willebrand factor in haemostasis and thrombosis. *Haemophilia*, 14 Suppl 5:11–26, November 2008.

[6] R Schneppenheim, M Barthels, and U Budde. [Inborn and acquired von Willebrand disease]. *Hamostaseologie*, 25(4):367–375, November 2005.

[7] Junyi Ying, Yingchen Ling, Lisa A Westfield, J Evan Sadler, and Jin-yu Shao. Unfolding the A2 Domain of Von Willebrand Factor with the Optical Trap. *Biophys J*, 98(8):1685–1693, 2010.

[8] S. Butenas, R. F. Branda, C. VanÂŧt Veer, K. M. Cawthern, and K. G. Mann. Platelets abd phospholipids in tissue factor-initiated thrombin generation. *Thromb Haemost*, 86:660–7, 2001.

[9] Hans-Jürgen von Bose. *Krankheitslehre*. Springer-Verlag Berlin Heidelberg New York, Berlin, 1995.

[10] D Chapman, WE Peel, and B Kingston. Lipid phase transitions in model biomembranes:: The effect of ions on phosphatidylcholine bilayers. *Biochimica et biophysica acta*, 464:260–275, 1977.

[11] Guillaume Tresset. The multiple faces of self-assembled lipidic systems. *PMC Biophysics*, 2(1):3, January 2009.

[12] Florian Georg Strobl. Zur Interaktion von Lipidmembranen und Nanopartikeln. *Scanning*, 2011.

[13] D O C Butt and P C Uni. The physics and chemistry of interfaces 1. 2001.

[14] P K Weissenborn and R J Pugh. Surface Tension and Bubble Coalescence Phenomena of Aqueous Solutions of Electrolytes. *Langmuir*, 11:1422–1426, 1995.

[15] Heiko Ahrens, S. Förster, and C.A. Helm. Polyelectrolyte brushes grafted at the air/water interface. *Macromolecules*, 30(26):8447–8452, 1997.

[16] W.D. Harkins and L.E. Copeland. No Title. *J. Chem. Phys.*, 10:272, 1942.

[17] O Albrecht, H Gruler, and E Sackmann. Polymorphism of phospolipid bilayers. *Le Journal De Physique*, 39:301, 1978.

[18] Susan Mabrey and Julian M Sturtevant. Investigation of phase transitions of lipids and lipid mixtures by high sensitivity differential scanning calorimetry. *Biochemistry*, 73(11):3862–3866, 1976.

[19] V V Plotnikov, J M Brandts, L N Lin, and J F Brandts. A new ultrasensitive scanning calorimeter. *Analytical biochemistry*, 250(2):237–44, August 1997.

[20] Verordnung über die Zulassung von Zusatzstoffen zu Lebensmitteln zu technologischen Zwecken (Zusatzstoff -Zulassungsverordnung - ZZulV). *BGBl. I S.*, page 230f, 2011.

[21] Alexander T Bauer, Elwira Strozyk, Christian Gorzelanny, Christoph Westerhausen, Anna Desch, Matthias F Schneider, and Stefan W Schneider. Surface area-dependent Cytotoxicity of Silica Nanoparticles induces Exocytosis of von Willebrand factor and necrotic Cell Death in primary human endothelial Cells. 2011.

[22] Julia Blechinger, Rudolf Herrmann, Daniel Kiener, F Javier García-García, Christina Scheu, Armin Reller, and Christoph Bräuchle. Perylene-Labeled Silica Nanoparticles: Synthesis and Characterization of Three Novel Silica Nanoparticle Species for Live-Cell Imaging. *Small*, 6(21):2427–2435, 2010.

[23] H. M. Tsai. Physiologic cleavage of von Willebrand factor by a plasma protease is dependent on its conformation and requires calcium ion. *Blood*, 87(10):4235–4244, 1996.

[24] M Furlan, R Robles, M Galbusera, G Remuzzi, P A Kyrle, B Brenner, M Krause, I Scharrer, V Aumann, U Mittler, M Solenthaler, and B Lammle. von Willebrand factor-cleaving protease in thrombotic

thrombocytopenic purpura and the hemolytic-uremic syndrome. *N. Engl. J. Med.*, 339:1578 – 1584, 1998.

[25] K. Fujikawa. Purification of human von Willebrand factor-cleaving protease and its identification as a new member of the metalloproteinase family. *Blood*, 98(6):1662–1666, September 2001.

[26] H. E. Gerritsen. Partial amino acid sequence of purified von Willebrand factor-cleaving protease. *Blood*, 98(6):1654–1661, September 2001.

[27] Dominic W Chung and Kazuo Fujikawa. Current Topics Processing of von Willebrand Factor by ADAMTS-13 âĂă. *Biochemistry*, 41(37):11065–11070, 2002.

[28] Joel L Moake. Thrombotic thrombocytopenic purpura: survival by "giving a dam". *Transactions of the American Clinical and Climatological Association*, 115(2):201–19, January 2004.

[29] Enrico Di Stasio, Stefano Lancellotti, Flora Peyvandi, Roberta Palla, Pier Mannuccio Mannucci, and Raimondo De Cristofaro. Mechanistic studies on ADAMTS13 catalysis. *Biophys J*, 95(5):2450–61, September 2008.

[30] Jeremy M. Berg, John L. Tymoczko, and Lubert Strye. *Biochemistry*. W. H. Freeman, New York, 5th edition, 2002.

[31] Otto G Berg, Joe Rogers, and Mahendra Kumar. Interfacial Catalysis by Phospholipase A2: Determination of the Interfacial Kinetic Rate Constants? *Biochemistry*, 30:7283–7297, 1991.

[32] Farideh Ghomashchi, Thomas O Hare, David Clary, and Michael H Gelb. Interfacial Catalysis by Phospholipase A2 : Evaluation of the Interfacial Rate Constants by Steady-State Isotope Effect Studies ? *Biochemistry*, 30:7298–7305, 1991.

[33] J. E. Sadler. The Metabolic Basis of lnherited Disease. In D. S. criver, C. R., Beaudet, A. L., Sly, W. S., and Valle, editor, *The Metabolic Basis of lnherited Disease*, pages 2171–2188. McGraw-Hill Book Co., New York, 6th. editi edition, 1989.

[34] Erik Adolf Von Willebrand. Hereditär pseudohemofili. *Finska Läkaresällskapets Handlingar*, 672:7–112, 1926.

[35] Erik Adolf Von Willebrand and R Jürgens. Über ein neues vererbbares Blutungsübel: die konstitutionelle Thrombopathie. *Dtsch Arch Klin Med*, 175:453–83, 1933.

[36] R Schneppenheim, U Budde, and Z M Ruggeri. A molecular approach to the classification of von Willebrand disease. *Best practice & research.*

Clinical haematology, 14(2):281–98, June 2001.

[37] ZM Ruggeri, FI Pareti, PM Mannucci, N Ciavarella, and TS Zimmermann. Heightened interaction between platelets and factor VIII/von Willebrand factor in a new subtype of von Willebrand's disease. *N Engl J Med*, 302(19):1047–51, 1980.

[38] Zaverio M Ruggeri and Theodore S Zimmerman. Variant von Willebrand ' s Disease - characterization of two subtypes by analysis of multimeric composition of factor VIII/ VWF in plasma and platelets. *J Clin Invest*, 65:1318–1325, 1980.

[39] A Engel, H E Gaub, and D J Müller. Atomic force microscopy: a forceful way with single molecules. *Current biology : CB*, 9(4):R133–6, February 1999.

[40] Elias M Puchner and Hermann E Gaub. Force and function: probing proteins with AFM-based force spectroscopy. *Current opinion in structural biology*, 19(5):605–14, October 2009.

[41] Csilla Gergely, Joseph Hemmerlï£¡, Pierre Schaaf, J K Heinrich Hï£¡rber, Jean-Claude Voegel, and Bernard Senger. Multi-bead-and-spring model to interpret protein detachment studied by AFM force spectroscopy. *Biophys J*, 83(2):706–722, August 2002.

[42] Ferdinand Kühner and Hermann E. Gaub. Modelling cantilever-based force spectroscopy with polymers. *Polymer*, 47(7):2555–2563, March 2006.

[43] Ferdinand Kühner, Matthias Erdmann, and Hermann Gaub. Scaling Exponent and Kuhn Length of Pinned Polymers by Single Molecule Force Spectroscopy. *Physical Review Letters*, 97(21):1–4, November 2006.

[44] Aleksandr Noy. Force spectroscopy 101: how to design, perform, and analyze an AFM-based single molecule force spectroscopy experiment. *Current Opinion in Chemical Biology*, 15(5):710–718, August 2011.

[45] Pierre-Gilles de Gennes. *Scaling concepts in polymer physics*. Cornell University Press, Ithaca, N.Y., New York, 1979.

[46] Dominik Breyer. *Mechanik des Bioproteins VWF : Simulation , Experiment und Analyse*. diploma thesis, University of Augsburg, 2011.

[47] A S M Kamruzzahan, Andreas Ebner, Linda Wildling, Ferry Kienberger, Christian K Riener, Christoph D Hahn, Philipp D Pollheimer, Peter Winklehner, Martin Hölzl, Bernd Lackner, Daniela M Schörkl, Peter Hinterdorfer, and Hermann J Gruber. Antibody linking to atomic force microscope tips via disulfide bond formation. *Bioconjugate Chem*,

17(6):1473–81, 2006.

[48] Dominik Breyer, Christoph Westerhausen, and Matthias Franz Schneider. Statistical simulations of force spectra of VWF-PEG-combinations based on a Boltzmann-ansatz with finite time steps and its consequences to force spectroscopy experiments in general. *(in preparation)*, 2012.

[49] R B Levene, F M Booyse, J Chediak, T S Zimmerman, D M Livingston, and D C Lynch. Expression of abnormal von Willebrand factor by endothelial cells from a patient with type IIA von Willebrand disease. *PNAS*, 84(18):6550–4, September 1987.

[50] H I Saba, S R Saba, J Dent, Z M Ruggeri, and T S Zimmerman. Type IIB Tampa: a variant of von Willebrand disease with chronic thrombocytopenia, circulating platelet aggregates, and spontaneous Type IIB Tampa: a variant of von Willebrand disease with chronic platelet aggregation. *Blood*, 66:282–286, 1985.

[51] M Donner, A C Kristoffersson, H Lenk, E Scheibel, E Dahlback, I M Nilsson, and I M Holmberg. Type IIB von WillebrandÂŠs disease: Gene mutations and clinical presentation in nine families from Denmark, Germany and Sweden. *Haematologica*, 82:58–65, 1992.

[52] P G de Groot, a B Federici, H C de Boer, P D'Alessio, P M Mannucci, and J J Sixma. von Willebrand factor synthesized by endothelial cells from a patient with type IIB von Willebrand disease supports platelet adhesion normally but has an increased affinity for platelets. *PNAS*, 86(10):3793–7, May 1989.

[53] M B Hultin and I I Sussmann. Postoperative thrombocytopenia in type IIB von Willebrand disease. *Am J Hematol.*, 33(1):64–68, 1990.

[54] Zaverio M Ruggeri. Type IIB von Willebrand disease: a paradox explains how von Willebrand factor works. *Thromb Haemost*, 2:2–6, 2004.

[55] Erich Sackmann and Rudolf Merkel. *Lehrbuch der Biophysik*. WILEY-VCH Verlag, Weinheim, 2010.

[56] HA Kramers. Brownian motion in a field of force and the diffusion model of chemical reactions. *Physica*, VII(4):284ff, 1940.

[57] P Haenngi, P Talkner, and Michal Borkovec. Reaction-rate theory: fifty years after Kramers. *Reviews of Modern Physics*, 62(2):251–342, 1990.

[58] R Zwanzig. Two-state models of protein folding kinetics. *PNAS*, 94(1):148–50, January 1997.

[59] J E Sadler. Von-Willebrand-Factor. *Journal of Biological Chemistry*, 266(34):22777–22780, 1991.

[60] R Schneppenheim, U Budde, and Z M Ruggeri. A molecular approach to the classification of von Willebrand disease. *Best Pract Res Clin Haematol*, 14(2):281–298, June 2001.

[61] Nina Kerk, Elwira A Strozyk, Birgit Po, and Stefan W Schneider. The Mechanism of Melanoma-Associated Thrombin Activity and von Willebrand Factor Release from Endothelial Cells. *Journal of Investigative Dermatology*, pages 2259–2268, 2010.

[62] Thomas Heimburg and Andrew D Jackson. The thermodynamics of general anesthesia. *Biophysical journal*, 92(9):3159–65, May 2007.

[63] E A Evans. Bending resistance and chemically induced moments in membrane bilayers. *Biophys J*, 14:923–931, 1974.

[64] Daniel Michael Steppich. *The Physics of Von Willebrand Factor*. Dissertation, University of Augsburg, 2008.

[65] D. Steppich, J. Griesbauer, T. Frommelt, W. Appelt, a. Wixforth, and M. Schneider. Thermomechanic-electrical coupling in phospholipid monolayers near the critical point. *Physical Review E*, 81(6):1–5, June 2010.

[66] W Rawicz, K C Olbrich, T McIntosh, D Needham, and E Evans. Effect of chain length and unsaturation on elasticity of lipid bilayers. *Biophysical journal*, 79(1):328–39, July 2000.

[67] Christoph Westerhausen, Florian Georg Strobl, Rudolf Hermann, Alexander Bauer, Stefan Wolfgang Schneider, Armin Reller, Achim Wixforth, and Matthias Franz Schneider. Chemical and mechanical impact of silica nanoparticles on the phase transition behavior of phospholipid membranes in theory and experiment. *Biophys J*, 102(5):1032–1036, 2012.

[68] C Greulich, S Kittler, M Epple, G Muhr, and M Köller. Studies on the biocompatibility and the interaction of silver nanoparticles with human mesenchymal stem cells (hMSCs). *Langenbeck's archives of surgery*, 394(3):495–502, May 2009.

[69] Barbara Rothen-Rutishauser, Robert N Grass, Fabian Blank, Ludwig K Limbach, Christian MuÌĹhlfeld, Christina Brandenberger, David O Raemy, Peter Gehr, and Wendelin J Stark. Direct Combination of Nanoparticle Fabrication and Exposure to Lung Cell Cultures in a Closed Setup as a Method To Simulate Accidental Nanoparticle Exposure of Humans. *Environmental Science {&} Technology*, 43(7):2634–2640, 2009.

[70] Shirley K. Knauer and Roland H. Stauber. Kontroverse im "Nanohype"

- Nanopartikel - Freund oder Feind. *DZKF*, 05/06(1-7), 2009.

[71] Christophe J. Barbé, J Bartlett, L Kong, K. Finnie, H. Q. Lin, M. Larkin, S. Calleja, A. Bush, and G. Calleja. Silica Particles: A Novel Drug-Delivery System. *Advanced Materials*, 16(21):1959–1966, 2004.

[72] Kai Simons and Winchil L C Vaz. Model systems, lipid rafts, and cell membranes. *Annual review of biophysics and biomolecular structure*, 33:269–95, January 2004.

[73] R Kwok and E Evans. Thermoelasticity of large lecithin bilayer vesicles. *Biophys J*, 35(3):637–652, 1981.

[74] Aurélien Roux, Damien Cuvelier, Pierre Nassoy, Jacques Prost, Patricia Bassereau, and Bruno Goud. Role of curvature and phase transition in lipid sorting and fission of membrane tubules. *The EMBO Journal*, 24(8):1537–1545, 2005.

[75] C T Leirer, B Wunderlich, a Wixforth, and M F Schneider. Thermodynamic relaxation drives expulsion in giant unilamellar vesicles. *Physical biology*, 6(1):016011, January 2009.

[76] Thomas Franke, Christian Leirer, Achim Wixforth, and Matthias F Schneider. Phase transition induced adhesion of giant unilamellar vesicles. *Chemphyschem*, 10(16):2858–61, November 2009.

[77] C Leirer, B Wunderlich, V M Myles, and M F Schneider. Phase transition induced fission in lipid vesicles. *Biophysical chemistry*, 143(1-2):106–9, July 2009.

[78] Joachim Seelig. Thermodynamics of lipid-peptide interactions. *Biochimica et biophysica acta*, 1666(1-2):40–50, November 2004.

[79] C Naumann, T Brumm, and T M Bayerl. Phase transition behavior of single phosphatidylcholine bilayers on a solid spherical support studied by DSC, NMR and FT-IR. *Biophysical journal*, 63(5):1314–9, November 1992.

[80] T Brumm, K Jø rgensen, O G Mouritsen, and T M Bayerl. The effect of increasing membrane curvature on the phase transition and mixing behavior of a dimyristoyl-sn-glycero-3-phosphatidylcholine/ distearoyl-sn-glycero-3-phosphatidylcholine lipid mixture as studied by Fourier transform infrared spectroscopy and. *Biophys J*, 70(3):1373–9, March 1996.

[81] Selver Ahmed and Stephanie L Wunder. Effect of High Surface Curvature on the Main Phase Transition of Supported Phospholipid Bilayers on SiO 2 Nanoparticles. *Langmuir*, 25(6):3682–3691, 2009.

[82] G. B. Alexander. The Effect of Particle Size on the Solubility of Amor-

phous Silica in Water. *J Phys Chem*, 61(11):1563–1564, 1957.

[83] J.D. Rimstidt and H.L. Barnes. The kinetics of silica-water reactions. *Geochimica et Cosmochimica Acta*, 44(11):1683–1699, November 1980.

[84] T L O'Connor. The kinetics for the solution of silica in aqueous solutions. *The Journal of Physical Chemistry*, 62(10):1195–1198, 1958.

[85] R K Iler. *The chemistry of silica: solubility, polymerization, colloid and surface properties, and biochemistry*. John Wiley {&} Sons, New York, 1979.

[86] T M Bayerl and M Bloom. Physical properties of single phospholipid bilayers adsorbed to micro glass beads. A new vesicular model system studied by 2H-nuclear magnetic resonance. *Biophysical Journal*, 58(2):357–362, 1990.

[87] Lev D Landau. *Lehrbuch der theoretischen Physik - Band V - Statistische Physik*. Harri Deutsch Verlag, Berlin, 1987.

[88] H Callen. *Thermodynamics and an Introduction to Thermostatistics*. Wiley-VCH, 2. edition, 1985.

[89] M F Schneider, D Marsh, W Jahn, B Kloesgen, and T Heimburg. Network formation of lipid membranes: triggering structural transitions by chain melting. *PNAS*, 96(25):14312–7, December 1999.

[90] Hermann Träuble, Max Teubner, Paul Woolley, and Hansjörg Eibl. Electrostatic interactions at charged lipid membranes: I. Effects of pH and univalent cations on membrane structure. *Biophysical Chemistry*, 4(4):319–342, 1976.

[91] Wolfgang Helfrich. Elastic Properites of Lipid Bilayers: Theory and Possible Experiments. *Z. Naturforsch*, 28 c:693–703, 1973.

[92] H Seto, N L Yamada, M Nagao, M Hishida, and T Takeda. Bending modulus of lipid bilayers in a liquid-crystalline phase including an anomalous swelling regime estimated by neutron spin echo experiments. *The European physical journal. E, Soft matter*, 26(1-2):217–23, 2008.

[93] Derek Marsh. Elastic curvature constants of lipid monolayers and bilayers. *Chemistry and physics of lipids*, 144(2):146–59, 2006.

[94] Wolfgang Helfrich. Amphiphilic mesophases made of defects. In *Physics of defects*. Amsterdam and New York, 1981.

[95] M. Winterhalter and W. Helfrich. Effect of surface charge on the curvature elasticity of membranes. *The Journal of Physical Chemistry*, 92(24):6865–6867, December 1988.

[96] C T Leirer, B Wunderlich, a Wixforth, and M F Schneider. Thermodynamic relaxation drives expulsion in giant unilamellar vesicles. *Physical biology*, 6(1):016011, January 2009.

[97] B Wunderlich, C Leirer, A-L Idzko, U F Keyser, A Wixforth, V M Myles, T Heimburg, and M F Schneider. Phase-state dependent current fluctuations in pure lipid membranes. *Biophys J*, 96(11):4592–7, June 2009.

[98] Klinman JP Nagel ZD. A 21st century revisionist s view at a turning point in enzymology. *Nature chemical biology*, 5:543–50., 2009.

[99] J K Raison. The influence of temperature-induced phase changes on the kinetics of respiratory and other membrane-associated enzyme systems. *Journal of bioenergetics*, 4(1):285–309, January 1973.

[100] Harold K Kimelberg and Demetrios Papahadjopoulos. Effects of Phospholipid Acyl Chain Fluidity , Phase Transitions and Cholesterol on (Na + + K +)-stimulated Adenosine Triphosphatase. *Journal of Biological Chemistry*, 249(4):1071–1080, 1974.

[101] Stefan Nuschele. *The Role of Interfaces in Enzyme Activity and Cell Adaptation*. Dissertation, University of Augsburg, 2010.

[102] Konrad Kaufmann. My theory. *Anahit AB publisher*, 2&3, 2009.

[103] Alfred Blume. A comparative study of the phase transitions of phospholipid bilayers and monolayers. *Biochimica et biophysica acta*, 557(1):32–44, October 1979.

[104] W R Burack and R L Biltonen. Lipid bilayer heterogeneities and modulation of phospholipase A 2 activity. *Chemistry and Physics of Lipids*, 73:209–222, 1994.

[105] L T Kopeikina, E F Kamper, I Siafaka, and J Stavridis. Modulation of synaptosomal plasma membrane-bound enzyme activity through the perturbation of plasma membrane lipid structure by bupivacaine. *Anesthesia and analgesia*, 85(6):1337–43, December 1997.

[106] K Reiss, I Cornelsen, M Husmann, G Gimpl, and S Bhakdi. Unsaturated fatty acids drive disintegrin and metalloproteinase (ADAM)-dependent cell adhesion, proliferation, and migration by modulating membrane fluidity. *J Biol Chem.*, 286(30):26931–42, 2011.

[107] DL Melchior and J M Steim. Thermotropic transitions in biomembranes. *Annual review of biophysics and*, 5:205–238, 1976.

[108] M I Angelova, S Soleau, P Meleard, J F Faucon, and P Bothorel. Preparation of giant vesicles by external AC electric ïňĄelds. Kinetics and

applications . *Prog Colloid Polym Sci*, 89:127–131, 1992.

[109] C Dietrich, O Boscheinen, K D Scharf, L Schmitt, and R Tampé. Functional immobilization of a DNA-binding protein at a membrane interface via histidine tag and synthetic chelator lipids. *Biochemistry*, 35(4):1100–5, January 1996.

[110] S Tristram-Nagle, R Zhang, R M Suter, C R Worthington, W J Sun, and J F Nagle. Measurement of chain tilt angle in fully hydrated bilayers of gel phase lecithins. *Biophys J*, 64(4):1097–109, April 1993.

Danksagung

Zum Schluss möchte ich mich hier bei allen Personen bedanken, die mich beruflich und privat unterstützt und motiviert haben bei der Anfertigung dieser Arbeit. Insbesondere:

Danke,

- Prof. Achim Wixforth, für die Ermöglichung der Arbeit am Lehrstuhl, deine motivierende Art und die angenehme Zusammenarbeit von Anfang an.
- Prof. Armin Reller, für die Erstellung des Zweitgutachtens.
- Prof. Matthias Schneider, für dein offenes Ohr, deine lockere Art und die ansteckende Begeisterung für die Wissenschaft, sowohl in der Uni als auch bei den ergiebigen Veranstaltungen in Maßbach.
- Dominik Breyer, für den Einsatz von mindestens deiner ganzen Arbeitskraft für die Optimierung des Messsystems und der Software, ohne die die quantitative Auswertung in diesem Maß niemals möglich gewesen wäre.
- Florian Strobl, für deinen unermüdlichen Einsatz in allem was Lipide angeht und deine kritische Sichtweise, die einen sehr guten Standpunkt gegenüber meiner pragmatischen und optimistischen Sichtweise bildet.
- Alexander Hupfer, für die blitzartige Unterstützung in sämtlichen Software und Hardware Fragestellungen sowie die Verstärker für die Süderhofparty.
- R308 d.h. allen jetzigen und ehemaligen Mitgliedern von Raum 308 für das tolle Klima.
- Marcin Malecha, vor allem für das Menschliche und die wunderbaren Feierabenddiskussionen. Dazu natürlich auch für die gelegentliche Benutzung deiner Couch.
- Judith Leese, für deine herrlich unbedarfte Art an dir unbekannte Sachverhalte heranzugehen. Für das geplante Esoterikbuch und deine weibliche Bereicherung in unserem sonst ausschließlich männlichem Raum 308.
- Andreas Hartmann, alias AC Haggi, dafür dass du so toll Pfeife rauchen kannst und das auch machst, für deine Kritikfähigkeit in biophysikalischen Fragen und deine Hausschuhe, die 308 viel gemütlicher gemacht haben.

- Jörg Kinzel, für dein lautes Lachen und den Einsatz deiner ebeam-Zauberkräfte.
- Bernhard Fichtl, für die Gespräche zu den "Enzymsachen".
- Benjamin Eggartlein, zunächst dafür, dass du keinen Vorschlag für ein Kalenderbild an NIM gesandt hast, was mir letztendlich erst den unsagbaren Ruhm des NIM Kalender 2011 Covers ermöglicht hat. Natürlich auch für deine ansteckende Gabe "Empathie zu machen"und die angenehme Zeit mit dir als Banknachbar und in Boston.
- Stefan Bössinger, für deine intra- und interkontinentale Freundschaft, für die vielen Stunden inner- und außerhalb des Labors, für die Information über den tagesaktuellen Dollarkurs, die Eurobonds aber auch das Onsager-Theorem und die Einführung in die amerikanische Kultur sowie die gemeinsamen Erlebnisse in Boston.
- Fif und Shamit, in Vertretung für das Bostoner Team mit Frank, Ali, Elbara und Dan für eure herzliche Art, mit der ich im "Wilden Westen"aufgenommen wurde.
- Konrad Konny Kaufmann, für die unglaubliche Inspiration, die von dir ausgeht und die einen dazu erzieht, die kritischen Fragen einfach zu stellen. Außerdem noch für die Gedichte und den zweiten Hauptsatz natürlich.
- Irene und Joachim Westerhausen, für eure Unterstützung von Anfang an bis heute, in ideeller, moralischer und finanzieller Hinsicht. Von nix kommt schließlich nix - und deswegen: Danke!
- Steffen und Alexander Westerhausen, dafür dass ihr einfach Konstanten in meinem Leben seid, auf die ich mich jederzeit verlassen kann und die mich immer zum Lachen bringen!
- Anna Westerhausen, für alles, angefangen von den Pfannkuchen und Semmelknödeln, über aufmunternde Worte bis zum gelegentlichen Einsatz einer Finanzspritze.
- Stefanie Langhans, Christian Zoth, Christian König und Martin Weckerle, für eure "Männerfreundschaften".
- Hütte Hausen, für eure langjährige Freundschaft, die sämtliche Stationen von Schule über Studium und Promotion überdauert und mich auf dem Boden gehalten hat.
- Michaela Helbig, für deine "Betreuung"und die Schnittchen während des Zusammenschreibens, die "Wollkn"und mehr!